Seismic structure of the St. Paul Fracture Zone and Late Cretaceous to Mid Eocene oceanic crust in the equatorial Atlantic Ocean near 18°W

Kevin Growe[1,1], Ingo Grevemeyer[1,1], Satish Chandra Singh[2,2], Milena Marjanovic[2,2], Emma PM Gregory[2,2], Cord Papenberg[3,3], Venkata Abhishikth Vaddineni[2,2], Laura Gómez de la Peña[4,4], and Zhikai Wang[2,2]

[1]GEOMAR Helmholtz Centre for Ocean Research Kiel
[2]Institut De Physique Du Globe De Paris
[3]Geomar, Kiel, Germany
[4]GEOMAR Helmholtz Centre of Ocean Research

November 30, 2022

Abstract

Plate tectonics characterize transform faults as conservative plate boundaries where the lithosphere is neither created nor destroyed. In the Atlantic, both transform faults and their inactive traces, fracture zones, are interpreted to be structurally heterogeneous, representing thin, intensely fractured, and hydrothermally altered basaltic crust overlying serpentinized mantle. This view, however, has recently been challenged. Instead, transform zone crust might be magmatically augmented at ridge-transform intersections before becoming a fracture zone. Here, we present constraints on the structure of oceanic crust from seismic refraction and wide-angle data obtained along and across the St. Paul fracture zone near 18°W in the equatorial Atlantic Ocean. Most notably, both crust along the fracture zone and away from it shows an almost uniform thickness of 5-6 km, closely resembling normal oceanic crust. Further, a well-defined upper mantle refraction branch supports a normal mantle velocity of 8 km/s along the fracture zone valley. Therefore, the St. Paul fracture zone reflects magmatically accreted crust instead of the anomalous hydrated lithosphere. Little variation in crustal thickness and velocity structure along a 200 km long section across the fracture zone suggests that distance to a transform fault had negligible impact on crustal accretion. Alternatively, it could also indicate that a second phase of magmatic accretion at the proximal ridge-transform intersection overprinted features of starved magma supply occurring along transform faults.

Seismic structure of the St. Paul Fracture Zone and Late Cretaceous to Mid Eocene oceanic crust in the equatorial Atlantic Ocean near 18°W

Kevin Growe[1,2] , Ingo Grevemeyer[1], Satish C. Singh[2], Milena Marjanović[2], Emma P. M. Gregory[2], Cord Papenberg[1], Venkata Vaddineni[2], Laura Gómez de la Peña[1], and Zhikai Wang[2]

[1]GEOMAR Helmholz Centre for Ocean Research Kiel

[2]Université de Paris, Institut de Physique du Globe de Paris; CNRS, Paris, France

Corresponding author: Kevin Growe (kevin.growe93@web.de)

Key Points:

- Seismic structure along the St. Paul fracture zone reflects magmatically accreted oceanic crust
- Oceanic crust across St. Paul shows only small thickness variations, lacking evidence for regional crustal thinning near fracture zones
- Magmatic nature of crust supports a mechanism where transform crust is augmented before being turned into a fracture zone

Abstract

Plate tectonics characterize transform faults as conservative plate boundaries where the lithosphere is neither created nor destroyed. In the Atlantic, both transform faults and their inactive traces, fracture zones, are interpreted to be structurally heterogeneous, representing thin, intensely fractured, and hydrothermally altered basaltic crust overlying serpentinized mantle. This view, however, has recently been challenged. Instead, transform zone crust might be magmatically augmented at ridge-transform intersections before becoming a fracture zone. Here, we present constraints on the structure of oceanic crust from seismic refraction and wide-angle data obtained along and across the St. Paul fracture zone near 18°W in the equatorial Atlantic Ocean. Most notably, both crust along the fracture zone and away from it shows an almost uniform thickness of 5-6 km, closely resembling normal oceanic crust. Further, a well-defined upper mantle refraction branch supports a normal mantle velocity of 8 km/s along the fracture zone valley. Therefore, the St. Paul fracture zone reflects magmatically accreted crust instead of the anomalous hydrated lithosphere. Little variation in crustal thickness and velocity structure along a 200 km long section across the fracture zone suggests that distance to a transform fault had negligible impact on crustal accretion. Alternatively, it could also indicate that a second phase of magmatic accretion at the proximal ridge-transform intersection overprinted features of starved magma supply occurring along the St. Paul transform fault.

Plain Language Summary

Transform faults represent plate boundaries where two plates move past each other without producing new or destroying the existing lithosphere. Most of the Atlantic transform faults and their inactive traces, fracture zones, were characterized by fractured and altered, thin-crust overlying serpentinized mantle rocks. However, recent results reveal that the crust beneath fracture zones may not be as thin and challenge the standard view, introducing a mechanism of secondary magma supply at the intersection between the ridge axis and transform fault. Here, we present results from seismic experiments at the St. Paul fracture zone near 18°W in the equatorial Atlantic. Our results suggest that the subsurface of the St. Paul fracture zone is represented by a nearly uniform crustal thickness of 5-6 km and an upper mantle with a velocity of 8 km/s. Both observations argue for a crust of magmatic origin and the absence of strong alteration of the upper mantle. Collectively, constant crustal thickness and little variation in seismic velocities along the profile crossing the fracture zone suggest that the crustal formation process does not vary as a function of distance from the fracture zone. Alternatively, secondary magma supply at the ridge-transform intersection could overprint any anomalous formation conditions.

1 Introduction

Plate tectonics separates Earth' surface into rigid plates (McKenzie, 1967; Morgan, 1968), and deformation or relative motion between plates reveals three different types of oceanic plate boundaries: (i) constructive plate boundaries at mid-ocean ridges (MOR) where new seafloor is created, (ii) destructive plate boundaries at subduction zones where the oceanic lithosphere is transferred into the mantle and recycled, and (iii) conservative plate boundaries and hence transform faults (TF) where the lithosphere is neither created nor destroyed as plates move past each other (Morgan, 1968). In ocean basins, transform faults offset MOR by tens to several hundreds of kilometers (Searle et al., 1994), splitting them into first-order spreading segments (Macdonald et al., 1988). They are long-lived features, and in the equatorial Atlantic, the largest transform faults, namely Chain, Romanche, and St. Paul, can be followed along their inactive traces, called fracture zones (FZ), towards the margins of the Atlantic Ocean (Wilson, 1965). Fracture zones are prominent linear features on the ocean floor that were identified and named before plate tectonics linked them to seafloor spreading (Menard, 1955; 1967).

Oceanic crust formed along a spreading ridge is generally believed to remain largely unchanged as it is moved by plate motion away from the active plate boundary. Its structure can be best described with respect to a layered structure, where the crust is divided into two main distinct lithologic layers exhibiting different seismic properties (e.g., Raitt, 1963). The upper crust (layer 2) consists of pillow basalts overlaying a basaltic sheeted dike complex (e.g., Vine & Moores, 1972) and reveals high velocity gradients of 1-2 s^{-1} and velocities from 3-5 km/s just below the basement to 6.3-6.8 km/s at a depth of 1-2 km below the basement (e.g., Grevemeyer et al., 2018; White et al. 1992; Whitmarsh, 1978). The mid- and lower crust (layer 3) instead consist of plutonic, mostly gabbroic, rocks and has low velocity gradients of 0.1-0.2 s^{-1} and velocities from ~6.6 km/s at the top of the layer to 7.2 km/s at its base (e.g., Carlson & Miller, 2004; Vine & Moores, 1972). The thickness of layer 3 is much more variable than the thickness of layer 2 such that variations in crustal thickness in several studies are related to thickness variations of layer 3 (e.g., Mutter & Mutter, 1993).

It has long been recognized that oceanic crust varies along spreading segments, with the thickest crust formed at a segment center away from major ridge crest discontinuities and the thinnest crust at segment ends or transform faults (e.g., Macdonald et al., 1988; Tolstoy et al., 1993). Along fast-spreading ridges, thickness variations are generally less than one kilometer (e.g., Canales et al., 2003). At slow- and ultraslow-spreading ridges, crust of ~7-9 km thickness may occur at segment centers and decrease to only 4-6 km at segment ends (e.g., Canales et al., 2000; Dannowski et al., 2011; Grevemeyer et al., 2018; Niu et al., 2015). These along-axis thickness variations can be best explained by focused mantle upwelling at segment centers and lateral melt transport, suggesting that mantle upwelling is intrinsically plume-like (3-D) beneath a slow-spreading ridge but more sheet-like (2-D) beneath a fast-spreading ridge (Bell & Buck, 1992; Lin & Morgan, 1992).

Along-axis changes in oceanic crustal architecture suggest that the end of spreading segments and hence transform faults represent the magmatically starved end-member of the oceanic crust (e.g., Detrick et al., 1993; White et al., 1984) where the principal orientation of tectonic stresses rotate by tens of degrees over a very short distance (Morgan & Parmentier, 1984), changing from normal faulting at the spreading axis to strike-slip along the transform (e.g., Sykes, 1967). In the Pacific, the crustal structure at transform faults reveals a drop of seismic P-wave velocity in the active strike-slip fault, indicating the presence of high porosities along the tectonically active fault trace (Roland et al., 2012). However, it shows little evidence for reduced melt supply as crustal thickness across the fast-slipping transforms indicates only a small reduction, which is in the order of several hundreds of meters (Roland et al., 2012). In contrast, some transform faults in the Atlantic exhibit thin crust ~4-5 km thick (e.g., Ambos & Hussong, 1986; Detrick et al., 1982; Whitmarsh & Calvert, 1986) along transform valleys which is 1-2 km thinner when compared to the neighboring normal oceanic crust (e.g., Grevemeyer et al., 2018; van Avendonk et al., 2017; White et al., 1992). The above observations led to the conclusion that lithosphere along transform faults and fracture zones might be intensely fractured, faulted, and composed of hydrothermally altered basaltic and gabbroic rocks overlying ultramafics that might be extensively serpentinized (Detrick et al., 1993; White et al., 1984).

A recent study suggests that the crust beneath the Chain fracture zone in the equatorial Atlantic region has a nearly normal crustal thickness (Marjanović et al., 2020). This observation has been independently supported using global bathymetric observations and numerical simulation on transform fault tectonics (Grevemeyer et al., 2021) suggesting that crust is (i) initially magmatically emplaced near a ridge-transform intersection (RTI), (ii) experiences tectonic deformation, and extension while being moved along the transform fault and (iii) finally it is augmented by the second stage of magmatism as it passes the opposing RTI. If correct, the formation of crust at transform faults should occur in three distinctive phases, suggesting that the structure of crust present below the valley of an active transform fault should differ profoundly from crust found along its fracture zones.

Here, we use two seismic profiles shot in 2017 and 2018 with modern seismic refraction and wide-angle equipment surveying the St. Paul fracture zone near 18°W in the equatorial Atlantic region (Fig. 1). The seismic data are well-suited for seismic tomography to study the structure along a 140 km-long roughly west-east running profile in the valley of the St. Paul fracture zone and along a 300 km-long north-south trending profile crossing the fracture zone and sampling the adjacent mature oceanic crust. The north-south striking profile is located roughly 850 km east of the eastern RTI of the St. Paul TF, extends from ~0.8°N to ~4°N, crosses the FZ at ~18°W/2°N and samples crustal ages of 70 Ma on the northern and ~45 Ma on the southern plate segment. Itruns parallel to the trend of the Mid-Atlantic Ridge (MAR) and hence should reveal features governed by changes in melt supply towards a transform fault and lateral melt transport, which is expected to diminish when approaching transform faults (e.g., Lin et al., 1990; Macdonald et al., 1988; White et al., 1984). The crustal and upper mantle velocity structures are derived from a joint tomographic inversion of first arrival travel times and wide-angle reflections from the crust-mantle boundary, providing high-resolution constraints on the seismic velocity structure and crustal thickness along the fracture zone and the dependence of crustal accretion as a function of distance to a fracture zone.

2 Regional Setting of the St. Paul Fracture Zone and Study Area

2.1 Regional Setting of the St.Paul Fracture Zone

The St. Paul fracture zone (SPFZ) is one of the major east-west striking equatorial fracture zones of the Atlantic Ocean. At the active MAR, the St. Paul, Romanche and Chain transform faults offset the ridge crest by ~1800 km, causing an age variation of 90 Myr over 400 km north-south distance (Müller et al., 2008). The active domain of the St. Paul transform fault system offsets the MAR by ~600 km and can be subdivided into four strike-slip faults; sandwiched in between are three short intra-transform spreading segments (Fig. 1a). Maia et al. (2016) studied the northern TF segment and found a complex tectonic regime revealing a transpressional zone exhuming deformed and serpentinized mantle rocks, triggered as a response to a change of relative plate motion ∼11 Myr ago. The fossil trace of the transform fault, the fracture zone can be followed using the vertical gravity gradient (Sandwell et al., 2014) across the entire Atlantic Ocean, from the continental shore of Liberia in the east to the Amazonas Basin in the west, resulting in a total length of ∼3000 km. For ages greater than 20 Myr (Mueller et al., 2008) away from both RTI, the bathymetry data indicate the presence of only two fracture zone valleys, suggesting that today's complex transform-fault-system developed roughly 20 Myr ago. Using 2-D ultra-deep multichannel seismic reflection data, Mehouachi and Singh (2018) imaged the lithosphere-asthenosphere boundary along a north-south striking line and revealed a southward thinning of the lithosphere, mimicking the age contrast across the system of fracture zones at ~18°W.

2.2 Study Area

Within our study area, ~800 km east from the active St. Paul transform fault system (Fig. 1a), the ~10 km wide northernmost St. Paul fracture zone valley (SPFZ-1) separates ~70 Ma oceanic lithosphere in the north from 40-50 Ma lithosphere in the south (Müller et al., 2008). Here, the valley is covered by sediments up to a kilometer thick, creating a smooth surface but still forming a 200-300 m deep valley with respect to the surrounding ocean floor (Fig. 1c). Its younger southern edge is flanked by significantly rougher bathymetry, revealing ridge-like features aligned mostly perpendicular to the FZ that we interpret as overshooting ridges, as observed near RTIs globally (e.g., Grevemeyer et al., 2021; Lonsdale, 1986; Marjanović et al., 2020). The older northern flank of the FZ can be subdivided into two distinct domains (Fig 1c). The north-western area to the west of the intersection of seismic profiles shows ridge- and dome-like features mostly parallel to the fracture zone. In contrast, the north-eastern domain reveals a rather smooth seafloor, except for a seamount-like structure located at the eastern limit of the west-east striking seismic line LI-02.

The north-south striking seismic line IS-01 ran over a smooth seafloor of an almost constant depth to the north of St. Paul, except for two ridge-like features near OBS 1 and OBS 5 (Fig 1b). The bathymetry to the south of SPFZ-1 is significantly rougher, showing east-west trending ridge-like features separating SPFZ-1 from a second, parallel fracture zone valley in the south (SPFZ-2) near OBS13. SPFZ-2 is related to the southernmost TF segment of the modern active TF system of St. Paul (Fig. 1a). The seismic line is limited in the south by another FZ parallel ridge south of SPFZ-2 and a deep basin just north of the Romanche TF (Fig. 1a, b).

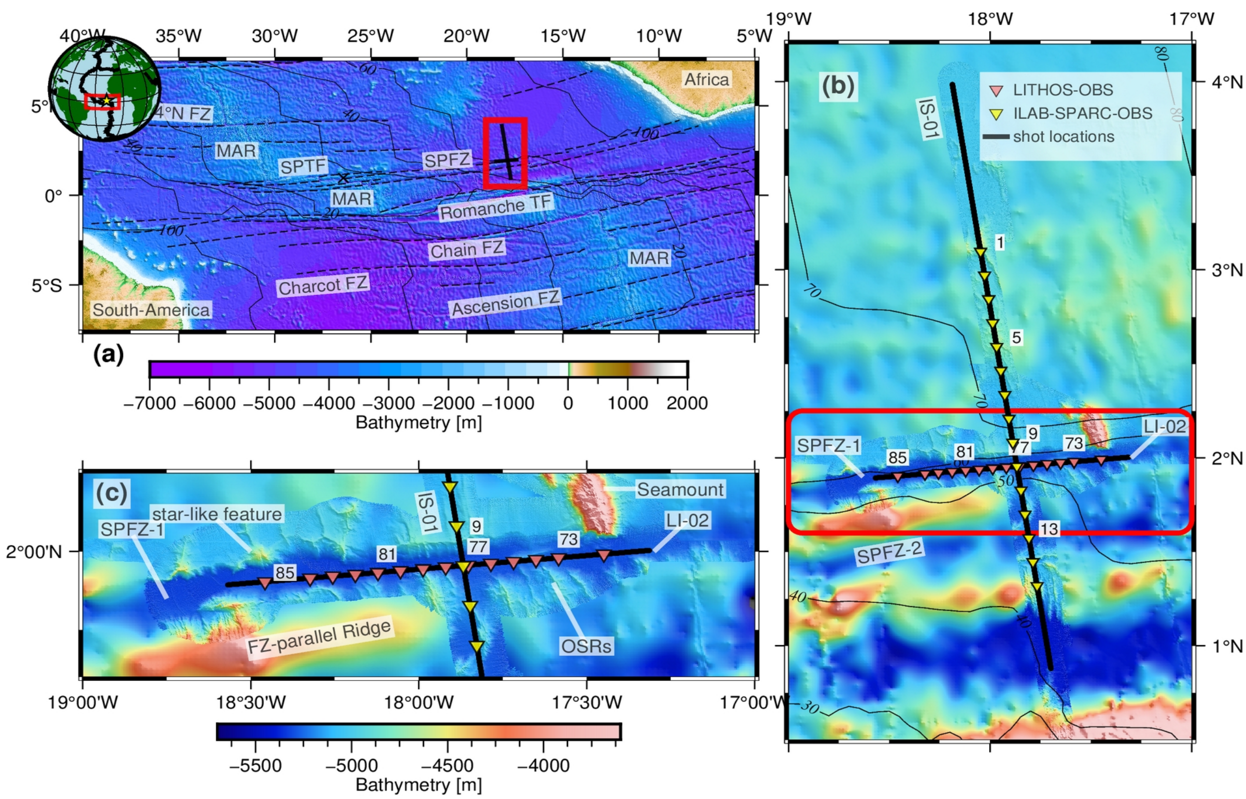

Figure 1: Regional and survey map in the equatorial Atlantic Ocean**. (a)** Bathymetric map showing survey location and tectonic setting around the SPFZ. The bathymetry is from TOPEX satellite gravity data (Sandwell et al., 2014). Thin labelled black lines denote crustal age after Müller et al. (2008) with an interval of 20 Myrs. Dashed lines denote fracture zones mapped by Matthews et al. (2011). Plate boundaries on inset globe are from Bird (2003) and yellow star indicates the survey location. The thick black lines represent the two survey lines (LI-02 and IS-01). Red box marks the survey area shown in (b). The black cross denotes the eastern RTI of the SPFZ. The main regional tectonic features are labeled (see definition of acronyms at the end of the caption). **(b)** Survey area showing shot and OBS locations for both seismic lines (note legend). Every fourth OBS is labeled. The bathymetry is combined with TOPEX data and acquired shipboard high resolution multibeam echo-sounder data (LITHOS: 100x100 m; ILAB-SPARC: 50x50 m). The crustal ages are indicated by thin black contours and labelled with an interval of 10 Myrs. The red box depicts the closeup map shown in (c). **(c)** Closeup of bathymetric map of the surveyed transect of the SPFZ-1 using the same color scale as in (b). Prominent bathymetric features are labeled. Remaining features are displayed as in (b). Acronyms: MAR - Mid-Atlantic Ridge, TF - Transform Fault, SPTF - St.Paul Transform Fault, SPFZ - St.Paul Fracture Zone OSRs - Overshooting Ridges.

3 Data Acquisition and Processing

In the framework of the Trans-Atlantic-iLAB and LITHOS projects, several OBS based seismic refraction lines, as well as multichannel seismic reflection lines, were acquired during three cruises in the central equatorial Atlantic Ocean from 2015-2018. In this study, we present the results from the two seismic refraction and wide-angle profiles along and across the St. Paul fracture zone, at 2°N/18° W, hereafter named as profiles LI-02 and IS-01 (see Supplementary Figs S1 and S2). Profile IS-01 is coincident with the seismic reflection profile of Mehouachi and Singh (2018).

3.1 Acquisition LI-02

Profile LI-02 was acquired during the LITHOS cruise onboard the German *R/V Maria S. Merian* in December 2017, where 12 four-component ocean bottom seismometers (OBS) and two one-component ocean bottom hydrophones (OBH) with a spacing of 7.5 - 15 km were deployed within the fracture zone valley (Fig. 1c). For simplicity, we will refer to all receiver types as OBS. A total of 875 shots were fired at 210 bars on a 142 km long east-west orientated transect. A shot time interval of 90 s with a vessel speed of ∼3.5 knots led to an average spatial shot interval of ∼160 m. The two airgun sub-arrays each consisted of six G-guns, provided a total volume of 86 l, and were towed at a depth of 7.5 m. The OBS data were sampled at 250 Hz. All instruments recorded good quality data containing crustal (Pg) and mantle (Pn) refraction arrivals up to offsets of 90 km, and all but two OBS, OBS 82 and 85, also recorded wide-angle reflections from the Moho (PmP) (Fig. 2). Pg and PmP arrivals could be picked mostly between 5-25 and 15-30 km offsets, respectively. Pn arrivals could be picked mostly up 60 km offset and even up to 80-90 km for some record sections (see all record sections in Figures S1a-n in the supplementary material). Since no streamer data were acquired along the profile, the basement depth and the sediment structures were obtained by mirror imaging (Supplementary material Fig. S3) of the hydrophone component of OBS receiver gathers (e.g., Grion et al., 2007).

3.2 Acquisition IS-01

Line IS-01 is the northernmost part of the north-south profile acquired during the ILAB-SPARC cruise aboard the French *R/V Pourquoi Pas?* in 2018. The profile is in total 850 km-long, crossing farther south the Romanche transform fault (~0°N) (Gregory et al., 2021) and the Chain fracture zone (~2°S) (Marjanović et al., 2020). Here, we use the data from the northernmost 350 km of the line containing 15 four-component OBS with an average instrument spacing of 14.2 km. The OBS data were sampled at 250 Hz. Most OBS receiver gathers provide good quality data where both refraction and wide-angle reflection arrivals can be identified with confidence (Fig. 2). Pg and PmP arrivals were picked mostly between 5-25 and 15-35 km offset, respectively. Pn arrivels could be picked mostly up 50 km offset (Fig. S2). A summary of the acquisition parameters for the two refraction profiles is provided in Table S1.

A total of 1168 shots were fired at a pressure of 140 bars and at a source interval of 300 m. The larger shot interval was chosen to minimize the noise level in the water column for later arrivals. Two sub-arrays containing eight G-guns each provided a total volume of 82 liters and were towed at a depth of 10 m. Real-time source monitoring provided excellent conditions for a well-tuned signal which is critical for such an experiment.

Simultaneously, a 6 km-long streamer containing 960 hydrophones, grouped with a spacing of 6.25 m, was towed at a depth of 12 m to acquire multi-channel seismic (MCS) data along the line. A basic processing sequence included bandpass filtering from 5-125 Hz, normal-move out (NMO) based stacking, and migration with a constant velocity of 1.5 km/s, which provided seismic images of the sediment cover and the depth of the igneous basement (Supplementary material Fig. S4). Due to the large shot interval and consequently low fold, the quality of the seismic image is poor below the basement. The MCS data were therefore mainly used to constrain the depth and shape of the basement below the sediment cover. Thus, both seafloor and basement were picked on the post-stack time-migrated section and converted to depth for the tomographic travel time inversion using the acoustic velocity of water and a constant velocity for sediments of 1.86 km/s derived as a mean from the semblance analysis of the ultra-long streamer data (Marjanović et al., 2020). Additional constrains on the sedimentary blanket along IS-01 are available for the coincident seismic profile of Mehouachi and Singh (2018).

3.3 OBS Processing

The OBS data were corrected for the internal clock drift and were relocated using the symmetry of the direct wave and a least-squares method (e.g., Creager & Dorman, 1982). The acoustic sound speed profile of water was obtained by onboard Expendable Bathythermograph (XBT) and World Ocean Circulation Experiment (WOCE) Conductivity/Temperature/Depth (CTD) data. The OBS depth was further corrected to match the constrained seafloor depth and a corresponding time shift was applied to the travel times. In this study, we only use the pressure components of the OBSs. The processing of the OBS data was carried out with Seismic Unix (Cohen & Stockwell, 2010) using the same sequence and parameters for both lines. A Butterworth-bandpass filter from 4-20 Hz was applied to the OBS gathers to filter low and high frequency noise. Moreover, a predictive deconvolution was applied to suppress some energy of the bubble reverberations and to facilitate the identification of the wide-angle reflection events. The shape and length of the wavelet, which is crucial for the performance of the predictive deconvolution, was obtained using a trace autocorrelation methodology (Yilmaz, 2001).

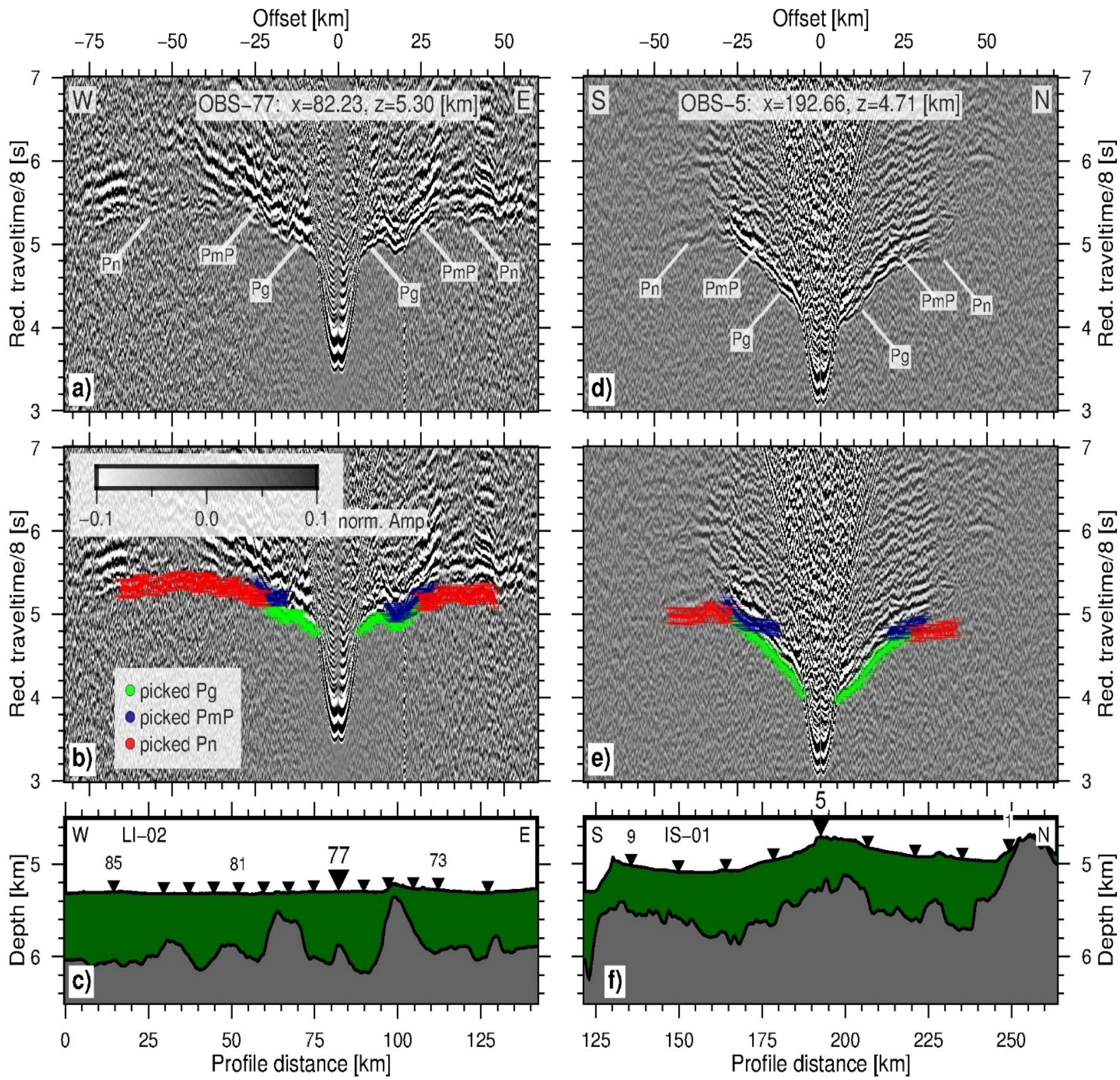

Figure 2: Record sections, labelled events and arrival picks for two selected OBS. **(a,d)** Processed receiver gathers of OBS 77 (panel a; LI-02) and OBS 5 (panel c; IS-01) with labelled seismic events. The travel time is reduced with 8 km/s. The amplitude is normalized by its maximum and clipped to 10 %. The X and Z coordinate represent the along-profile-axis distance and the water depth of the OBS. **(b,e)** The same record sections with travel time picks superimposed where colored dots and error bars illustrate the picked arrivals for the three distinct seismic phases (Pg, PmP, Pn; see legend) and their individual pick uncertainty. **(c,f)** Corresponding OBS locations (black inverse triangles), bathymetry and the sediment thickness (green area) above the igneous basement (gray area). The OBS of the illustrated receiver gather is highlighted. Every fourth OBS is labelled.

4 Tomographic Traveltime Inversion

For the tomographic inversion, a total of ∼10100 refracted first arrivals (Pg and Pn) and ∼2700 wide-angle reflection arrivals (PmP) were manually picked on the 29 receiver gathers (along both lines) and an offset-dependent uncertainty was assigned to each pick (e.g., Fig. 2). The estimated uncertainties are 30-50 ms for Pg, 70 ms for PmP, and 80-110 ms for Pn arrivals. Both the forward modeling and inversion were carried out using the package TOMO2D from Korenaga et al. (2000). This code applies a hybrid scheme of the shortest path method from Moser (1991) for calculating the least traveltimes between the grid nodes followed by a ray bending method (Moser, 1992) to fine-tune these initial ray paths and minimize their travel times. The ray bending is thereby conducted using a conjugate gradient method (Moser, 1992). For the inverse problem the traveltime residuals for each raypath are equalized with perturbations of the velocity and the reflector nodes with respect to a reference model, forming a sparse linear system (Korenaga, 2000). Hereinafter, the linear system is normalized by data and model covariance, regularized with smoothing and damping constraints (Korenaga, 2000) and can be solved by the sparse matrix solver LSQR (Paige & Saunders, 1982).

The model domains were discretized into 726x141 (for line LI-02) and 1167x141 (for line IS-01) cells with a horizontal node spacing of 200 and 300 m, respectively. The larger horizontal node spacing for IS-01 was chosen due to the larger shot interval of 300 m. The variable vertical node spacing increases with depth from 50 m at the seafloor to 250 m at the bottom of the model. Initially, the horizontal and vertical correlation lengths, smoothing, and damping weights that regularize the nonlinear inversion were tested and evaluated. Since the seismic velocity generally varies more vertically than laterally, smaller vertical than horizontal correlation lengths were used, which increased linearly with depth. Based on the smaller shot and receiver spacing and hence the higher resolution, slightly smaller correlation lengths were used for the line LI-02. Additionally, considering the lower uncertainties of Pg picks, we chose smaller regulation weights for the Pg inversion than for the PmP and Pn inversion steps. A 1-D velocity model of oceanic crust hung below the constrained sediment/basement interface (Fig. 3) was used as a starting velocity model. All parameters of the discretization, forward modelling and inversion are also listed in Table S2 in the supplementary material.

The inversion was carried out following a top-to-bottom approach. Hence, first, the near offset Pg arrivals were inverted to constrain the shallower upper crust before adding the further offset Pg arrivals and inverting again to obtain the velocity structure of the upper and intermediate depths of the crust. Thereafter, the PmP reflection arrivals were added and inverted with an initial flat Moho reflector with a predefined constant depth (on average 6 km below the mean basement depth). The reflector is modeled as a floating reflector with only one degree of freedom vertically, and is thus independent from the velocity nodes (Korenaga et al., 2000). A depth kernel weighting factor, which controls the tradeoff between the velocity and the reflector depth ambiguity from the PmP arrivals (Korenaga et al., 2000) was chosen to be 1 such that velocity and reflector depth perturbation are equally weighted. Each iterative inversion stage in the top-to-bottom approach is stopped by reaching a normalized target $\chi 2 \leq 1.2$ or when a maximum number of iterations (eight for each Pg segment and PmP) is reached, which results in an excellent fit to observed and calculated travel times (Fig. 4). The ray coverage in the model domain is represented by the derivative weight sum (DWS; Toomey & Foulger, 1989), which incorporates not only the number of rays going through each cell but also their individual path length through the cell and their uncertainty.

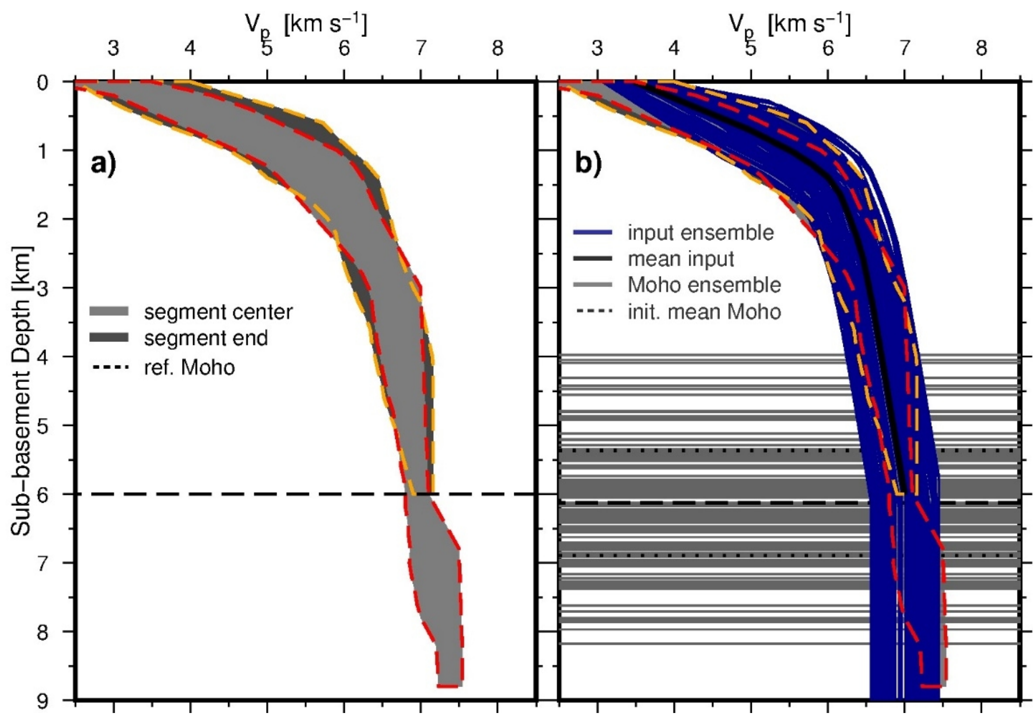

Figure 3: Velocity and Moho reflector input ensembles. **(a)** Reference velocity ensembles and crustal thickness obtained for the central portion of the MAR segments (light grey, dashed orange frame) and the segment ends (dark grey, dashed red frame) after Grevemeyer et al. (2018). **(b)** Randomized input velocity (blue) and initial flat Moho (light grey) ensemble for Monte Carlo analysis. Solid, dashed, and dotted black lines indicate the mean initial 1D-velocity-depth function, the mean initial flat Moho and its standard deviation, respectively.

To minimize the bias from the initial model and to evaluate the model uncertainty, a Monte Carlo analysis (MCA) was performed in which a set of 100 randomized starting velocity models (e.g., Fig. 3) and a set of 100 initial flat Moho reflectors of various constant depths were inverted and averaged to obtain the final crustal model and its standard deviation (see Appendix 1). For the MCA, the 100 1-D input velocity functions were randomized around a reference velocity function for the Atlantic crust, which is derived as a mean from a compilation of velocity-depth profiles from the Atlantic Ocean for ridge segment ends (Grevemeyer et al., 2018; Fig. 3). The 100 initial flat reflectors were randomized around a flat Moho reflector 6 km below the average basement depth.

After obtaining the final average crustal velocity model from the MCA, an initial velocity model for the upper mantle was added and hung below the mean constrained Moho reflector. To create the initial 1-D input velocity function for the upper mantle, we observed an apparent velocity of 8 km/s in the Pn arrivals within the data, and reduced this slightly to 7.8 km/s at the Moho depth. Below the Moho, the mantle velocity increase was defined subsequently by three velocity gradients: 0.1 s-1 from 0 to 1 km, 0.05 s-1 from 1 to 5 km, and 0.04 s-1 from 5 km to the model bottom. In the final stage of the entire cumulative inversion scheme, the picked Pn arrivals were added, and all arrivals were inverted to obtain the final result that included the velocity in the crust, the Moho reflector, the uppermost mantle (Figs 5 and 6). Due to the high uncertainty of the Pn picks (80-110 ms) and a previously well constrained final crustal model, a normalized $\chi^2 \leq 1.2$ was thereby reached after only 2-3 iterations, despite larger damping weights in order to avoid significant changes within the already constrained crust. The model error is estimated by the computation of the RMS-fit and the normalized χ^2, which incorporates the data variance, represented by the individual pick uncertainty.

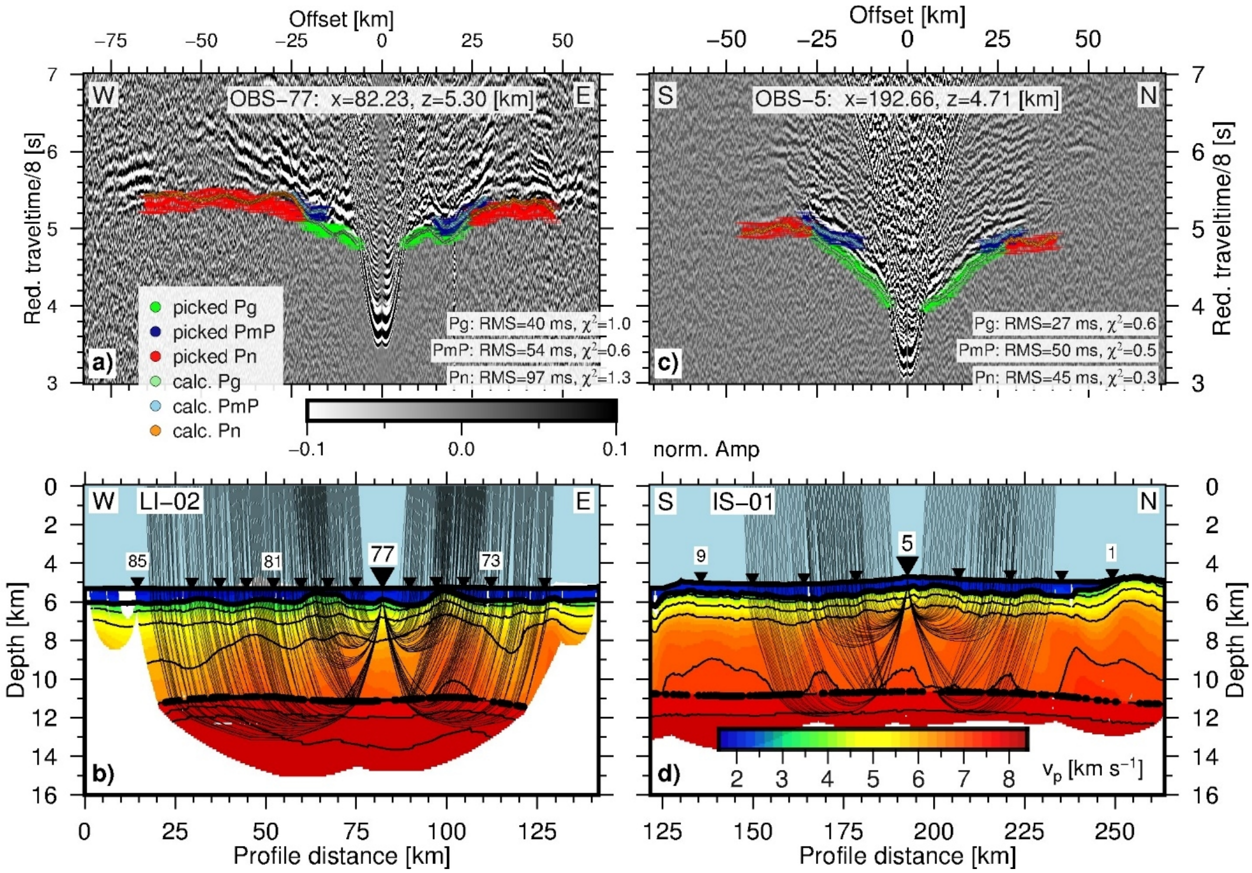

Figure 4: Traveltime fits and raypaths for two selected OBS. **(a,c)** Processed receiver gathers of OBS 77 (panel a) and OBS 5 (panel c) with picked and calculated travel times superimposed and **(b,d)** their corresponding ray paths superimposed on the final velocity models centered at OBS-5 (d) north of and OBS-77 (b) within the SPFZ-1. Thick black dots denote the modelled Moho reflection points, respectively. The velocity contour interval is 1.0 km/s for the crust, starting with 4 km/s, and 0.1 km/s for the mantle, starting at 8.0 km/s. The remaining elements are the same as in Figure 2.

To estimate the spatial resolution and the sensitivity of the inversion scheme with respect to the parametrization of the model space, we conducted multiple checkerboard tests with varying wavelengths and a velocity perturbation amplitude of 10 % (see Figs S6 and S7 in the Supplementary material). The results show that anomalies of 25 km horizontal and 5 km vertical diameter are well resolved with nearly full amplitude for both profiles. Anomalies of 15 km horizontal and 3 km vertical diameter are only relatively well resolved in the upper to intermediate crust. In particular, the low velocity anomalies are poorly recovered in the lower crust.

As our obtained Moho reflectors are rather flat and do not show much undulations we conducted several regularization and resolution tests. To investigate the effect of the regularization on the depth and the topography of the Moho, we significantly reduced the correlation length and the smoothing and damping weights for the PmP inversion during the MCA (Table S3). As expected, the results show more undulations, but with the reduction of the regularization we consequently decrease the data fit to $\chi^2_{PmP}<1$ and thus overfit the PmP-data. A comparison between the resulting Mohos and the crustal thicknesses using different regularizations is presented in the supplements (Figs S8 & S9). We further tested the resolution of our method in terms of the combination of both an anomalous sinusoidal Moho reflector with two different wavelengths, with an oscillating perturbation amplitude of 1 km, and gaussian velocity anomalies with a perturbation amplitude of 10 %, placed above the Moho in the lower crust. The results show a very good recovery of the velocity anomalies and a good recovery of the anomalous reflector for perturbations with a wavelength of 70 km (Figs S10 and S11). Instead, the Moho perturbations with a wavelength of 40 km are not resolved (Figs S12 and S13). We thus deduce that due to the high uncertainties of the PmP picks we cannot resolve small scale undulations of the Moho without introducing overfitting of the data. Hence, we favor the smoother Moho model with a χ^2~1 that perfectly represents the data with respect to its uncertainties.

Finally, to test the sensitivity within the mantle we introduced gaussian anomalies with a horizontal diameter of 50 km, a vertical diameter of 3 km and a perturbation amplitude of 5 % (Figs S14 and S15) below the constrained Moho reflector. The results reveal that positive anomalies in the mantle are well resolved up to a perturbation amplitude of 0.2-0.3 km/s. Conversely, the negative anomalies are with amplitudes up to only 0.1 km/s significantly less recovered. All results of the resolution tests are included in the supplementary material.

5 Tomographic Results

In the following paragraphs the results of the tomographic travel time inversion are presented separately for the two seismic lines: LI-02 running along the St. Paul fracture zone (Fig. 5) and IS-01 crossing the St. Paul fracture zone. Note, the results of line IS-01 running north-south (Fig. 6) are subdivided into the distinct areas of north of the SPFZ-1, crossing the SPFZ-1 and south of the SPFZ-1.

5.1 LI-02: Along the St.Paul Fracture Zone

5.1.1 LI-02: Crustal Seismic Structure along the St.Paul Fracture Zone

The crustal thickness along LI-02 varies from 4.8–5.6±0.3 km, resulting in a mean crust of 5.2 km (Tab. 1 and Fig. 7b). The velocities along the FZ, particularly in the western and central part of the profile, are remarkably lower in the upper and mid-crust with respect to the reference model (0.2-0.7 km/s; Fig A1). Along most of the profile, the seismic velocities do not exceed 5 km/s within a sub-basement-depth of 1 km, and the usual seismic layer 3 velocity of ~6.6 km/s (e.g., Christeson et al., 2019; Grevemeyer et al., 2018) is reached not before 3-4 km depth into the crust (Figs 5 and 8). However, the eastern part of the profile shows slightly higher velocities of up to ±0.2 km/s with respect to the reference model and ±0.4-0.8 km/s with respect to the western part of the profile. Further, these higher velocities (from 90 – 110 km along profile distance) coincide with a basement high within the FZ (Figs 5 and 7) and thicker crust, indicating an enhanced magma supply.

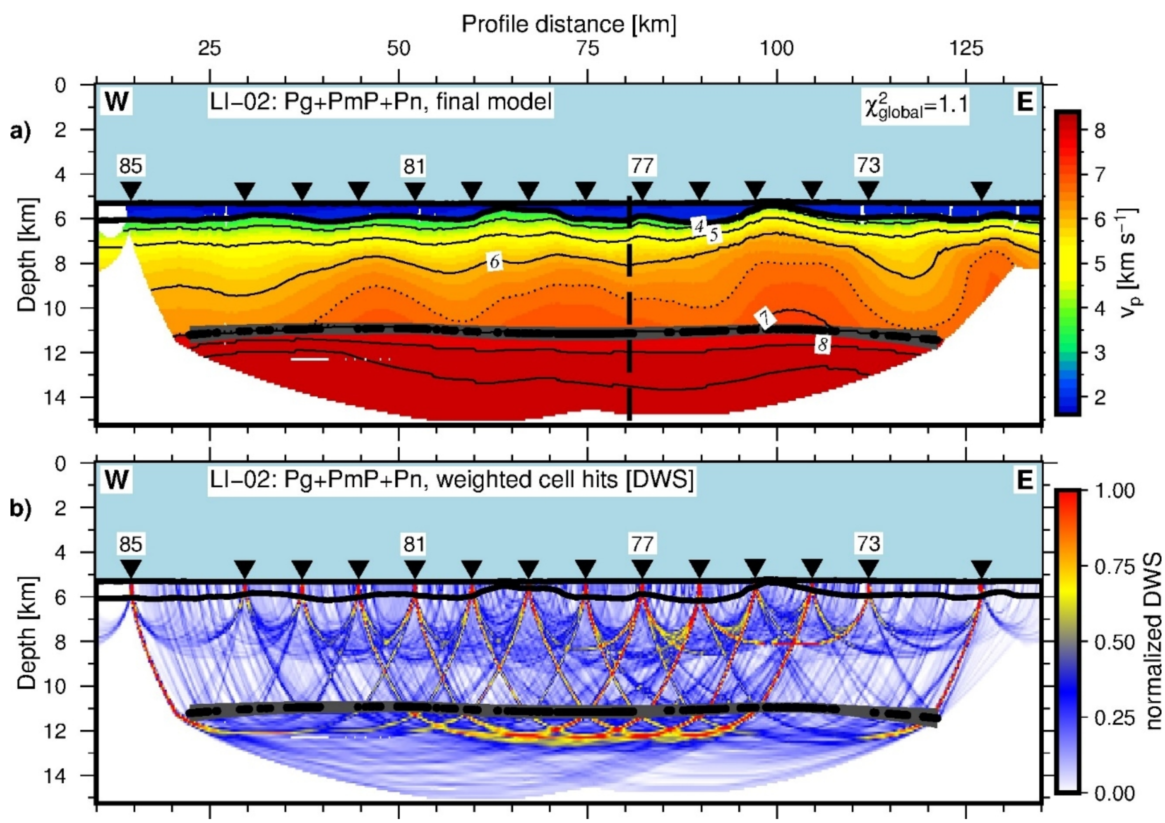

Figure 5: Inversion results for line LI-02. **(a)** Crustal and upper mantle velocity model obtained by cumulative Pg, PmP and Pn inversion. The contour interval is 1 km/s in the crust starting at 4 km/s and 0.1 km/s in the mantle starting at 8.0 km/s. The dotted line represents a usual velocity of the lower crust of 6.6 km/s. Black dots and grey shading denote the modelled Moho reflection points and the Moho standard deviation, respectively. The vertical dashed line depicts the intersection location with line IS-01 (Fig. 1b). The remaining elements and symbols are the same as in Figure 4. **(b)** Corresponding normalized DWS for the crust and upper mantle.

5.1.2 LI-02: Upper Mantle Structure along the St. Paul Fracture Zone

The Pn inversion yields a rather homogeneous upper mantle with velocities of ~8 km/s along the profile LI-02 and hence parallel to the spreading direction (Figs 5 and 7). Abundant far offset Pn arrivals up to 100 km on several OBS gathers provide ray penetration up to 6 km below the Moho, and hence a good ray coverage in the upper mantle (Fig. 5). Therefore, these mantle velocities are real and not attributable to the initial velocity model.

5.1.3 LI-02: Uncertainties along the St. Paul Fracture Zone

The final computed Pg, PmP, and Pn arrivals yield RMS fits of 46, 56, and 91 ms, respectively, and result in a normalized global χ^2 of 1.1. During the MCA, the standard deviation of the velocity model is reduced from 0.3-0.5 km/s to <0.2 km/s in the upper crust and < 0.1 km/s in the intermediate and lower crust (Fig. A1). The standard deviation for the Moho reflector depth and hence the crustal thickness is reduced from an initial 0.75 km to a mean of 0.3 km. The mean values and uncertainties for both crustal thickness and velocities are provided in Table 1.

5.2 IS-01: Across the St. Paul Fracture Zone

5.2.1 IS-01: North of SPFZ-1

The final crustal model for IS-01 reveals a relatively constant crustal thickness along the whole profile (Figs 6 and 7) but can be subdivided into the two parts: north and south of the SPFZ-1 in terms of velocity structure. The part north of the FZ encompasses a distance of ∼110 km (from 130 km to 240 km along profile distance), which displays a crustal thickness of 5.0-5.4±0.3 km (mean=5.3 km). A thick crust, ~6.5±0.5 km (Fig. 7), is observed at the northern end of the profile in a 15-20 km wide zone (at distance ~240 km), which coincides with a high basement topography (Figs 6 and 7). However, since the Moho reflector north of ~240 km (along profile distance) is not constrained by reversed ray coverage (Fig. 6), it may not be resolved properly and is hence excluded from the further interpretation and statistical computations. The velocity structure north of the FZ is relatively uniform and shows significantly higher crustal velocities (+0.2-0.6 km/s) with respect to the reference model (Fig. A2).

The velocity depth-profiles in this region extracted from the final crustal velocity model (in Figure 8 marked as o, p, and q) resemble the seismic structure of usual oceanic crust containing the two-layer gradient structure with a high-velocity gradient in the upper crust and a low-velocity gradient in the intermediate and lower crust representing layers 2 and 3, respectively (Fig. 8 b, c). Here, layer 2 reveals velocities ∼4 km/s at the top increasing to ∼6.2-6.5 km/s at its base (∼1.6±0.3 km sub-basement depth); the velocities of layer 3 increase from ∼6.5-6.7 km/s at the top of the layer to ∼6.9-7.2 km/s at the base of the crust.

When compared to most of the profiles from LI-02, along the FZ, the layer 2-layer 3 boundary is more distinctively defined north of St. Paul. Further, crustal velocities are generally higher, with values of ~4.5-5 km/s in the upper crust compared to <3.5 km/s at the top of the crust along the FZ, and values of >6.8 km/s in the lower crust compared to ~6.3-6.8 km/s at the base of the crust along the FZ. However, the eastern domain of LI-02 (profiles d, e in Fig. 8) shows a closer similarity to the crust north of St. Paul, with a potential layer 2-layer 3 transition occurring at ~1.7 km below the basement.

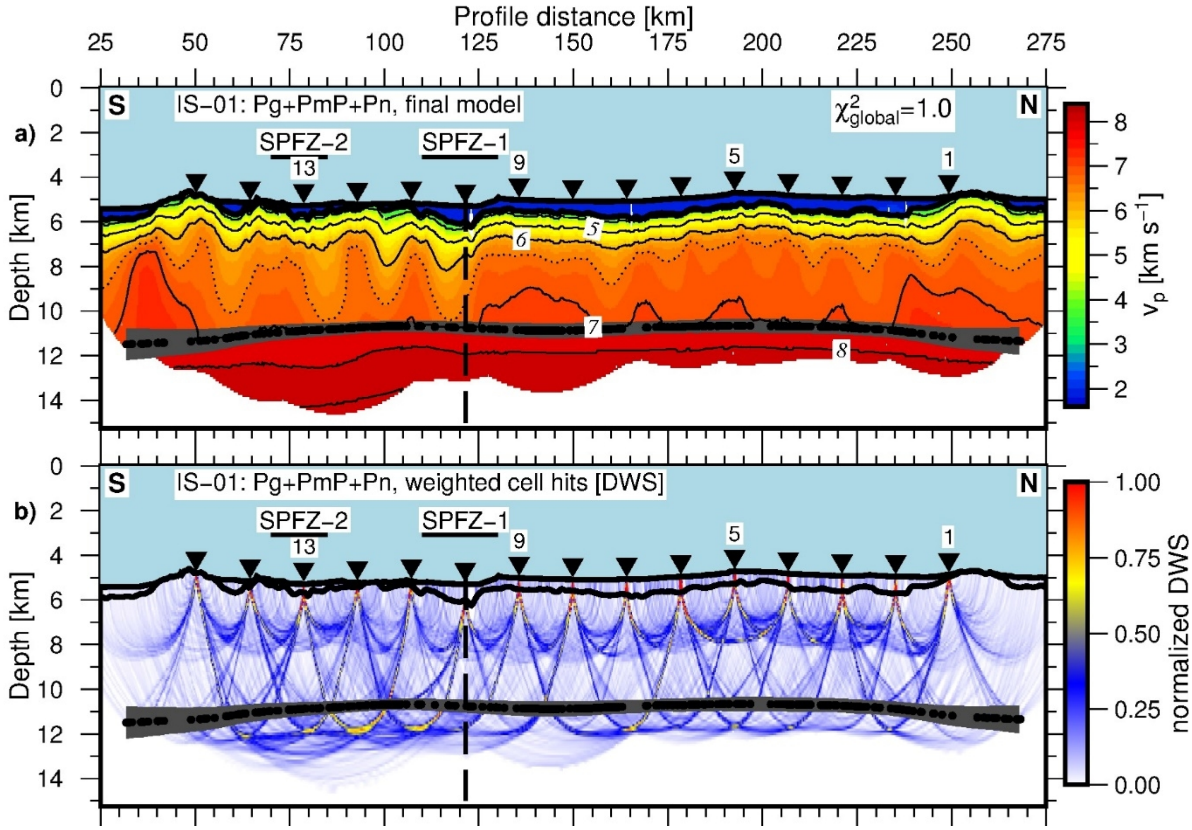

Figure 6: Inversion results for line IS-01. **(a)** Crustal and upper mantle velocity model obtained by cumulative Pg, PmP and Pn inversion. **(b)** Corresponding DWS for the crust and upper mantle. Thick horizontal labelled bars indicate the two FZs and their extent derived from the bathymetry (Fig. 1b). The remaining figure elements and contour intervals are the same as in Figure 5.

5.2.2 IS-01: Across SPFZ-1

Across the SPFZ-1 from north to south, the crustal thickness decreases from 5.2±0.3 km to 4.8±0.3 km (Figs 6 and 7). Within a distance of ~20 km from the center of the valley, the crust thickens again to 5.3±0.4 km, resulting in a zone of reduced crustal thickness about 20 km-wide The FZ exhibits only slightly lower velocities compared to the reference model at segment ends (Fig. A2). However, with respect to the adjacent crust in the north of the FZ it reveals a remarkable velocity reduction of 0.4-0.8 km/s throughout the upper and mid-crustal region (Fig. 8c: compare profile n with o, p, q).

5.2.3 IS-01: South of SPFZ-1

The southern part of the profile differs remarkably from the observations in the northern part, showing more heterogeneities both in crustal thickness and velocities (Figs 6 and 7). The crust thickens from the FZ southwards from a rather thin crust of 4.8±0.3 km to 5.6±0.3 km within a distance of ∼60 km (from 115 km to 55 km along reverse profile distance) and reaches a maximum thickness of 6.7±0.4 km below another basement high at the southern end of the profile. However, similarly to the northern limit of the profile, the crustal thickness for distance <55 km is not very well constrained and hence is not included in the statistical computations and discussion. The velocity distribution shows both positive and negative anomalies with respect to the reference model, but the velocities are generally lower than those north of the FZ by 0.2–0.8 km/s (Figs 8 and A2). The strong velocity variations affect both the upper and the lower crust. Parts of the structure south of St. Paul, for example, the low velocity zone just north of the SPFZ-2 (profile m in Fig. 8a, c), show a similar range of velocities to the structure along the FZ. However, they also show a clear division into two layers with a high gradient upper crust and low gradient mid- to lower-crust (occurring at ~1.5 km for profile m), and so cannot be considered to exhibit the same crustal structure as inside the FZ. Conversely, other sections south of St. Paul, such as at ~70 km along profile (profile l in Fig. 8a,c), show a more similar velocity structure to the crust north of the FZ.

5.2.4 IS-01: Upper Mantle Structure across SPFZ

The Pn inversion yields rather homogeneous upper mantle velocities of 7.8-8 km/s along the whole profile IS-01 (Figs 6 and 7). Due to a decreasing signal/noise ratio at far offsets in some record sections and a conservative picking approach of only including picks with uncertainties of <0.12 s, Pn offsets of good quality were generally limited to offsets smaller than 60 km.

5.2.5 IS-01: Uncertainties across SPFZ

The final computed Pg, PmP, and Pn arrivals yield RMS fits of 41, 67, and 85 ms, respectively, resulting in a global normalized $\chi 2$ = 1.0 for both the crustal and the joint crustal and mantle models. An example of traveltime fits is illustrated in Figure 4. During the MCA, the velocity standard deviation was reduced from 0.3-0.5 km/s to ∼0.2 km/s in the upper crust and < 0.1 km/s in the middle and lower crust (Fig. A2). The significantly higher uncertainty in the shallow crust is caused by predominantly vertical travel path of the rays and the resulting low sensitivity. The ray coverage is highest between 1.5-2.0 km of sub-basement depth since this is the depth where the most rays turn (Fig. 6). Note that beyond the receiver line the crustal velocities are constrained by only one-sided ray coverage and thus yield a very high uncertainty. The standard deviation for the Moho reflector depth and hence the crustal thickness north of the FZ, the FZ itself and south of the FZ is reduced from 0.75 km to 0.3 km. Mean values and uncertainties for both crustal thickness and velocities are provided in Table 1.

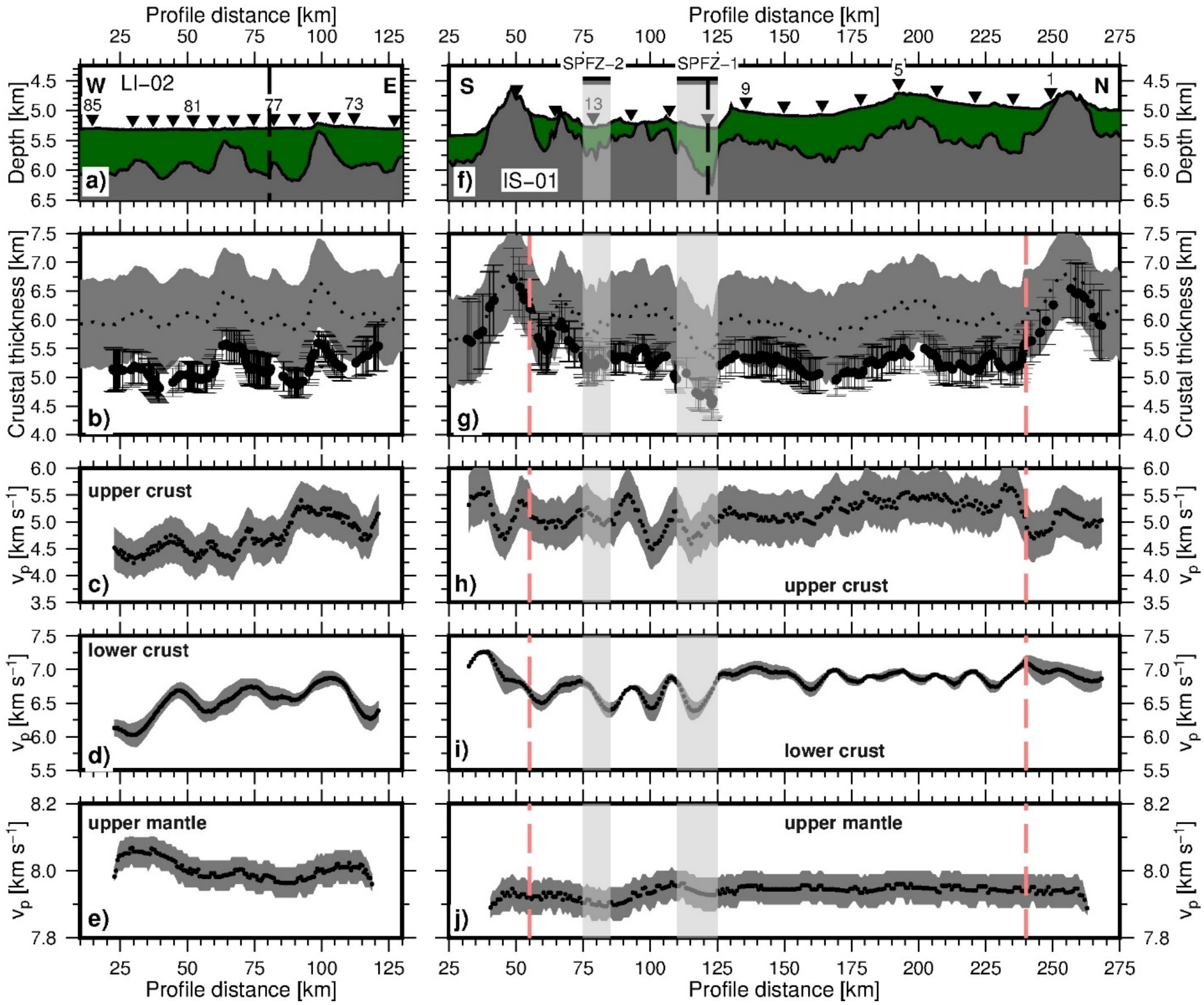

Figure 7: Bathymetry, sediment and crustal thickness as well as mean velocities for upper and lower crust and upper mantle along both refraction lines (LI-02: panels a-e, IS-01: panels f-j). **(a,f)** Bathymetry, sediment thickness (green region) above the basement (gray region) and OBS locations. **(b,g)** Black dots with error bars denote the crustal thickness obtained from the modelled Moho reflection points and their standard deviation. The dotted line and grey shading denote the mean and standard deviation of the crustal thickness input ensemble. **(c-e, h-j)** Vertically averaged velocities for the upper crust (panels c,h; 0.25 - 1.25 km sub-basement), lower crust (panels d,i; 0.25 -2.5 km above Moho) and the upper mantle (panels e,j; 0.25 -1.25 km below Moho) and their corresponding standard deviation (grey shading) along the two lines, respectively. Vertical light grey shading indicates the extent of the two fracture zone valleys (SPFZ-1,SPFZ-2; Fig. 1). Vertical red dashed line excludes the edge regions that are not constrained by reverse ray coverage for IS-01. Remaining elements are the same as in Figure 2 and 5.

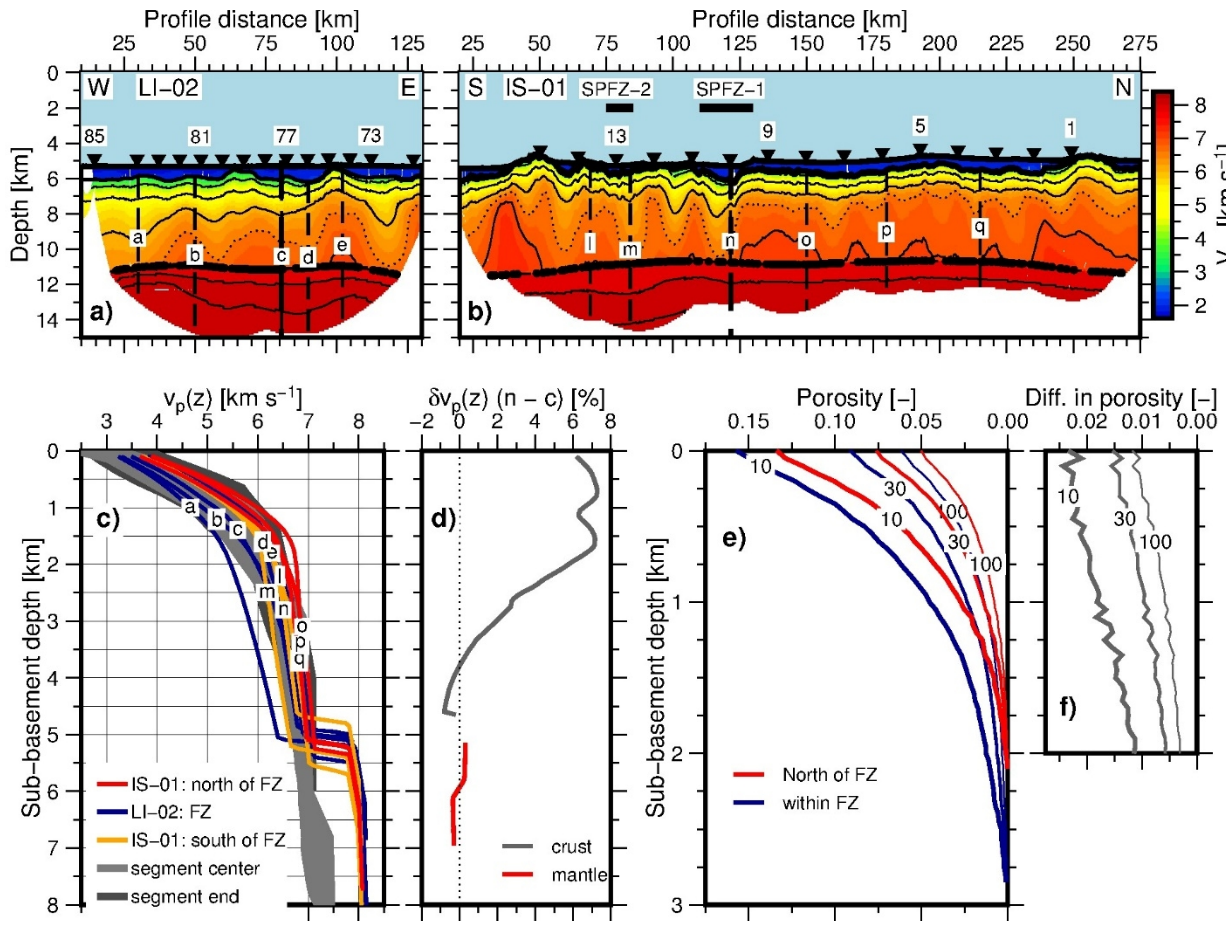

Figure 8: Velocity and porosity compilation for the two lines. **(a,b)** The locations for the selected 1-D velocity-depth profiles (labelled vertical dashed lines) of line LI-02 (a) and line IS-01 (b) are superimposed on the final velocity models. Remaining figure elements are the same as in Figure 5. **(c)** Extracted velocity depth profiles. Each profile represents the average of the velocity-depth profiles for four adjacent horizontal nodes. **(d)** Velocity difference within the vicinity of the profile intersection (profile n – profile c). **(e)** Porosity estimates using DEMA for averaged velocity depth functions of the SPFZ-1 (averaged from 15 -120 km distance alongside LI-02) and the crust north of it (averaged from 130 -240 km distance alongside IS-01). The labels indicate different aspect ratios of the fractures. **(f)** Difference in porosity between the crust within the fracture zone and north of it (FZ – North).

5.3 Summary of Results

Table 1 lists the findings of this study regarding crustal and upper mantle properties for three distinct regions: north of St. Paul, south of St. Paul, and along the St. Paul FZ itself. The mean upper crustal velocity is obtained from averaging vertically and horizontally down from 0.25-1.25 km of sub-basement depth. The lower crustal velocity is obtained by vertical and horizontal averaging of the 0.25–2.5 km (reversed depth) of the lower crust just above the constrained Moho reflector. The mean upper mantle velocity is obtained from vertical and horizontal averaging between 0.5-2 km below the constrained Moho reflector. Only regions with sufficient ray coverage contribute to these statistical computations. The overall variability of the velocity structure in the survey area is also summarized in Figure 9, where 1-D velocity depth profiles are extracted for both lines with an interval of three horizontal nodes and colored for the distinct regions.

Table 1: Summary of the main findings regarding crustal and upper mantle properties.

Parameter / Location	**North of FZ**	**Along FZ**	**South of FZ**
Crustal thickness [km]	5.3 ± 0.3	5.2 ± 0.3	5.4 ± 0.3
Vp upper crust [km/s]	5.2 ± 0.5	4.7 ± 0.4	5.1 ± 0.4
Vp lower crust [km/s]	6.9 ± 0.1	6.5 ± 0.1	6.7 ± 0.1
Vp upper mantle [km/s]	7.9 ± 0.05	8.0 ± 0.05	7.9 ± 0.05

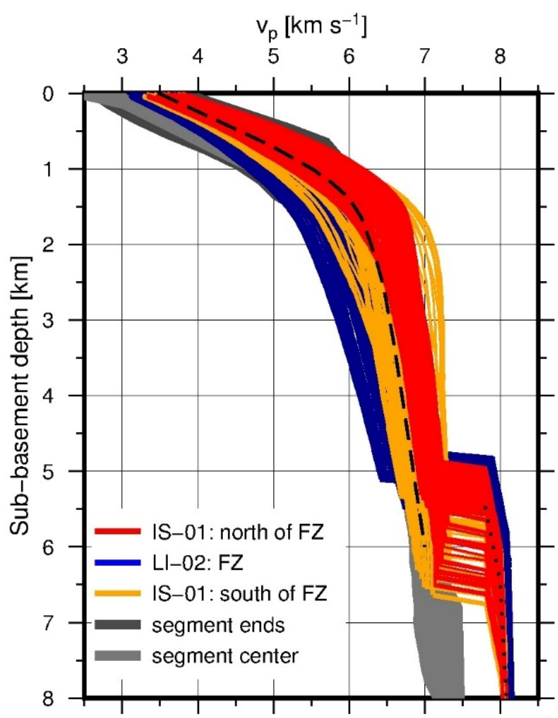

Figure 9: Velocity-depth compilation. The 1-D velocity-depth functions are extracted with an interval of three horizontal nodes (0.6 km for LI-02 and 0.9 km for IS-01, respectively) and color coded for the distinct regions (see legend). Grey shading indicates the reference velocity ensemble from Grevemeyer et al. (2018). The dashed and dotted lines denote the mean initial velocity-depth function for the crust and the initial velocity-depth function used below the constrained Moho for the Pn inversion, respectively.

6 Discussion

6.1 Crustal Thickness along the St. Paul Fracture Zone

In the literature the term fracture zone has been loosely used for both the tectonically and seismically active transform fault offsetting the spreading axis and its inactive fracture zone (e.g., Detrick et al., 1993). Here, we will use the term “transform fault” for the active plate boundary offsetting the spreading axis, while with the term “fracture zone”, we will refer to the inactive fossil trace where lithosphere of contrasting age meets and subsidence occurs on either side depending upon their thermal structures (e.g., Menard, 1967; Sandwell, 1984). This clear separation between the fracture zones and the transform faults is important as recent evidence suggest that crust accreted along a transform fault might be affected by processes acting at ridge-transform intersections before it converts into a fracture zone (e.g., Grevemeyer et al., 2021; Marjanović et al., 2020).

The St. Paul fracture zone reveals an average crustal thickness of ~5.2 km, which is roughly 1 km thinner when compared to the global average of normal oceanic crust of 6.15 km thickness (e.g., Christeson et al., 2019), but close to the thickness of oceanic crust in the equatorial Atlantic, from 5.6-6.0 ±0.1 km (Vaddineni et al., 2021). Interestingly, it did not show any significant change in the crustal thickness with respect to the crust found either to the north or south of the FZ. Furthermore, its thickness is in the same order of magnitude as the Chain FZ (Marjanović et al., 2020) and falls in the range of other FZ surveyed in the Atlantic Ocean, e.g., ∼4.5 km at Tydeman FZ (e.g., Calvert & Potts, 1985; Potts et al., 1986a), ~5 km for the Mercurius FZ (Peirce et al., 2019). Additionally, Davy et al. (2020) observed a crustal thickness of ~6 km for the Late Cretaceous Marathon FZ. A new compilation of crustal thicknesses of major Atlantic TF and FZ (Marjanović et al., 2020) indicates thin crust at some transform faults (2-5 km) whereas most fracture zones have crustal thicknesses in the range of usual oceanic crust (5-7 km). An exception, however, is the Kane FZ, which shows a significantly thinner crust (2-3 km) (Cormier et al., 1984; Detrick & Purdy, 1980).

In general, the thinner crust found along transform faults and fracture zones is clearly consistent with the concept of focused mantle upwelling along mid-ocean ridges (e.g., Lin et al., 1990; Tolstoy et al., 1993), supporting magmatically starved conditions acting at transform faults. Further, geological observations and sampling of rocks from transform valleys at slow- and ultraslow-spreading ridges often reveals exposed upper mantle rocks near segment ends (e.g., Cannat, 1993; Cannat et al., 1995). These observations are consistent with the inferences from Detrick et al. (1993), suggesting that crust found at both transform faults and fracture zones is “thin, intensely fractured, and hydrothermally altered basaltic section overlying ultramafics that are extensively serpentinized in places”. However, the crust within the St. Paul FZ is only slightly (0.1-0.3 km) thinner when compared to oceanic crust adjacent to the FZ. A gradual crustal thinning over a distance of several tens of kilometers on either side of a fracture zone or transform fault, as reported previously for some fracture zones in the North Atlantic (White et al., 1984), is not observed, neither across the St. Paul FZ as shown in our data nor across the Chain FZ (Marjanović et al., 2020). One interpretation might be that the crust found along transform faults may deviate significantly from oceanic crust in fracture zones, as envisioned recently (Grevemeyer et al., 2021).

A similar deduction has been made recently to explain the crustal structure across the Chain FZ. Marjanović et al. (2020) suggested that lateral dyke propagation along the adjacent spreading axis into the transform fault augments crust at RTIs. Such a dyke injection is supported by the presence of J-shaped ridges in the vicinity of RTIs observed in a global study of transform faults (Grevemeyer et al., 2021). Bathymetric data obtained along the St. Paul FZ reveal a number of such J-shaped ridges, though ridge tips are often blanketed by sediments (Fig. 1c). Dyking is possibly controlled by 3-D mantle upwelling as envisioned by Lin et al. (1990) at slow spreading ridges. At the 21°30’N segment of the MAR, ridge propagation forced by lateral dyking has not only advanced into the transform domain, but cut through a transform fault, causing its die-off (Dannowski et al., 2018). We therefore propose that a second phase of RTI magmatic accretion might be an important process shaping the crust and lithosphere at the proximal end of transform faults. However, the proposed model is still rather conceptual and thus we cannot rule out that magma migrates also along the base of crust. A scenario where magma is supplied within the mantle before intruding into the crust may explain better the layer-2/layer-3 type layered structure of the crust found along St. Paul than a model where dyking alone is governing RTI magmatism.

The occurrence of a second phase of RTI magmatism is supported by geological sampling, revealing that lithosphere along transform valleys is generally characterized by mantle exhumation (e.g., Fox et al., 1986; Tucholke & Lin, 1994), while outside corners and fracture zones are dominated by magmatically accreted basaltic crust (e.g., Karson & Dick, 1984). The observation that even the floor of a fracture zone valley (Karson & Dick, 1983) is composed of basaltic rocks supports the interpretation that transform crust is being augmented at RTIs by magmatism.

Finally, it is important to emphasize if crust and mantle are indeed modified by a second phase of magmatic activity at RTIs it may also explain some of the local variability observed both in our models and features not explicitly modelled here, like amplitude variations of either PmP or Pn. Thus, in contrast to oceanic crust emplaced at a spreading segment, at the RTI magmatism only may modulate the pre-existing highly hydrated lithosphere. We therefore cannot rule out that fragments of serpentinized mantle or hydrated lower crust occur along fracture zones. However, our data strongly support the view that the overall structure of the St. Paul FZ is magmatic in origin rather than featuring hydrated lithosphere as proposed previously (e.g., Detrick et al., 1993).

6.2 Seismic Velocity Structure along the St. Paul Fracture Zone

Crustal seismic velocities along the SPFZ reveal significantly reduced values when compared to the crust north of the FZ. Throughout the upper and middle crust, velocities are reduced by 0.2-1.1 km/s. The velocity structure within the FZ, however, still shows the typical features of a two layered structure of normal oceanic crust formed at segment ends (Fig. 8c), i.e., a high-velocity gradient upper crust and a low-velocity gradient lower crust. This decrease in seismic velocity throughout the entire crust might be best explained by the presence of large-scale porosity and fracturing of crustal rocks. Nevertheless, the observed layered structure closely resembling oceanic crust supports that crust, though fractured, was magmatically accreted. Therefore, the crust found along the St. Paul FZ differs profoundly from the conventional wisdom where crust at discontinuities is generally characterized by basically a single layer and thin crust (e.g., Davy et al., 2020). For a mature oceanic crust near 15°N/55°30’W in the Atlantic Ocean, Davy et al. (2020) suggest that the structure of ridge crest discontinuities is controlled by the behavior of adjacent spreading segments. Therefore, crust accreted at discontinuities near magmatically starved spreading segments will mimic those conditions, while crust formed at transforms or higher-order ridge offsets adjacent to magmatically robust segments will reflect magmatically accreted crust. The accretion near St. Paul seems to have occurred during a period of constant magma supply from the mantle.

To estimate the porosities associated with decreasing velocity, we carried out a differential effective medium analysis (DEMA) after Taylor and Singh (2002). The DEMA was performed for a host rock of basaltic composition and assuming a population of aligned, elongate, fluid-filled fractures with aspect ratios (ARs) between 10 and 100 (Supplementary Fig. S5). The porosities are computed for laterally averaged 1-D velocity-depth profiles for both within the SPFZ-1 (line LI-02, from 25- 120 km along profile distance) and the crust resembling normal oceanic crust north of the SPFZ-1 (line IS-01, from 130-240 km along profile distance). The results and their deviation for three different ARs (10, 30, 100) are illustrated in Figures 8e and 8f. We obtain porosities decreasing from up to ~15% in the top of the crust to ∼0 % at sub-basement depths at 2.0-2.75 km for an AR of 10. For an AR of 100 in contrast, the porosity is reduced from only ∼6 % at the top of the basement to ∼0 % at depths of 1.5-2 km. Depending on the AR the DEMA reveals porosities that are ~2.25 % (AR=10) to 0.5-1 % (AR=100) higher for the FZ with respect to the crust north of it (Fig. 8f). A recent study of the crust at the Romanche TF indicate that the porosity could be 15% near the seafloor decreasing to 1% at the base of the crust (Gregory et al., 2021). If similar porosity was present within the active St. Paul TF, the reduced porosity could be explained by combination of lateral dyke injection at the RTI (Marjanović et al., 2020) and hydrothermal alteration and mineral precipitation (Audhkhasi & Singh, 2019; Grevemeyer et al., 1999) during the early development of the fracture zone.

Increased porosity, which in turn causes decreasing seismic velocities, might be related to past deformation along the shear zone of the transform fault and/or emplacement of crust in a tectonically dominated environment at RTIs. This observation nurtures previous interpretation that fracture zones might be formed by hydrothermally altered basaltic and gabbroic sections that are to some degree fractured and faulted, as envisioned earlier (e.g., Detrick et al., 1993; White et al., 1984). However, even though crust might be partially altered and fractured, within the St. Paul FZ the mantle rocks do not seem to consist of extensively serpentinized peridotite. Instead, the presence of clear PmP reflection arrivals along the FZ valley and a continuous upper mantle Pn refraction with apparent velocity of ∼ 8 km/s support a relatively dry mantle with a low degree of hydration or even the absence of upper mantle serpentinization along the entire section of the SPFZ-1. Inverted velocities along LI-02 are in the order of ~8 km/s (Fig. 7) and therefore much faster than mantle velocity of <7.5-7.8 km/s reported for some Atlantic transform faults (e.g, Detrick et al., 1993; Davy et al. 2020), supporting our interpretation. The dehydration of the mantle might be caused by the presence of higher temperature and crustal thickening dyke injection at the RTI, where the transform fault becomes a fracture zone.

6.3 Crustal Thickness as a Function of Distance across St. Paul Fracture Zone

Most previous studies along the axis of the MAR have revealed a strong dependence of crustal thickness variations along the ridge crest (e.g., Lin et al., 1990) and hence distance to a transform fault. For example, between 33-35°N of the MAR, Canales et al. (2000), and Hooft et al. (2000) observed that crustal thickness varies significantly as a function of distance from both the Oceanographer transform fault and non-transform offsets, showing thick crust at segment centers (up to 8 km) and thin crust at segments' ends (<3 km). Similar features are observed at the MAR at 21°N (Dannowski et al., 2011), and 5°S (Planert et al., 2009) and along the ultra-slow spreading Southwest Indian Ridge at 50°E (Niu et al., 2015), and 66°E (Muller et al., 1999). In general, crustal thickness at segment ends of slow-spreading ridges is in the order of 4-6 km thick and at segment centers thickness may increase to 7-9 km (e.g., Grevemeyer et al., 2018). It is, therefore, remarkable that our north-south profile reveals an almost constant thickness of 5.2-5.6 km over 100 km from the FZ with no obvious dependence of crustal thickness with distance to the St. Paul fracture zone at 2°N. Similar features are reported for the MAR in the vicinity of the Chain fracture zone, where crustal thickness is in the order of 4.6 to 5.9 km, showing no significant imprint of the transform discontinuity on ridge crest segmentation (Marjanović et al., 2020). One explanation might be that mantle upwelling in the equatorial Atlantic has been more sheet-like, and hence more similar to the type of mantle upwelling imagined for fast-spreading ridges rather than plume-like or 3-D mantle upwelling suggested for the slow-spreading MAR (Lin & Morgan, 1992). However, the reason why mantle upwelling in the equatorial Atlantic should differ from elsewhere along the MAR (e.g., Hooft et al., 2000; Planert et al., 2009; Dannowski et al., 2011) remains elusive.

Another interesting feature is that the observed crustal thickness averages ~5.4 km along the ~200 km long north-south trending profile (IS-01). Farther south, between 0° and ~3°S around the Chain FZ, crustal thickness is 4.6-5.9 km (Marjanović et al., 2020) and at 2°S of the MAR the crustal thickness ranges from 5.6 to 6.0 km along a 600 km long flow line profile (Vaddineni et al., 2021). However, Christeson et al. (2020) reported from five ridge parallel profiles at 31°S a significant crustal thickness variations of 3.6 to 7.0 km for different crustal ages (6-60 Ma), but an almost constant thickness along each profile and thus for crust of the same age, suggesting that the equatorial and south Atlantic shows consistently thinner crust when compared to the average thickness of 7 km reported by White et al. (1992) for the Atlantic. However, we have to note that that data compiled by White et al. (1992) occurred predominantly in the North Atlantic with a large number of experiments in the north-western Atlantic where crust is in the order of 7-8 km (e.g., Purdy, 1983; Minshull et al., 1991), suggesting that previous estimates might be biased. In contrast, the majority of crustal thickness estimates, either along our profiles or elsewhere in the equatorial or south Atlantic region, compares well with global estimates of the global mean crustal thickness (e.g., Chen, 1992; Christeson et al., 2019; Harding et al., 2017; Van Avendonk et al., 2017), revealing an average global crustal thickness of 6.15 km (Christeson et al., 2019). Therefore, most observed crustal thickness estimates compare well to predictions from petrological models, suggesting an average crustal thickness of 6 km emplaced at a normal mantle temperature of 1300°C (e.g., McKenzie & Bickle, 1988; Korenaga et al., 2002). However, slightly reduced crustal thickness in the equatorial Atlantic of ~5.3 km between Chain and Romanche, roughly 6 km north of Romanche (Gregory et al., 2021) and <5.5 km along our longitudinal profile may supports a cooler mantle underlying the equatorial Atlantic. This interpretation is supported by the exceptionally low degree of melting of the upper mantle in the equatorial Atlantic as indicated by the chemical composition of mantle-derived mid-ocean ridge peridotites and basalts (Bonatti et al., 1993; Dalton et al., 2014) and upper mantle S-wave velocity (Grevemeyer, 2020; James et al., 2014).

6.4 Anisotropy

To assess the crustal and mantle anisotropy, the velocity structure from both seismic lines was compared in the vicinity of their intersection, averaging properties over a roughly 1 km long section (due to different node spacing we averaged 0.8 km along LI-02 and 1.2 km along IS-01). Figure 8d shows the velocity structure of the profiles at the intersection. Positive values indicate faster velocities mapped along line IS-01 running roughly north-south and hence parallel to the strike of the ridge axis. Anisotropy reaches a maximum of ~7% in the upper 2 km of the crust and decreases continuously to zero at a depth of ~4 km below the basement and thus may occur within the sheeted dykes. Within the upper mantle, no significant velocity anisotropy can be observed.

Our observation of the upper to mid-crustal anisotropy indicates higher velocities perpendicular to the fracture zone (i.e., along the strike of the ridge) with respect to velocities obtained parallel to the fracture zone (i.e., perpendicular to the ridge axis). It is interesting to note that our observations are consistent with that at the East Pacific Rise, where 4% of anisotropy was observed with the fast direction roughly trending along the strike of the ridge crest (e.g., Dunn & Toomey, 2001), which was interpreted to represent the effect of ridge-parallel trending faults. At St. Paul, the fast-direction seems also to be orientated parallel to the spreading axis. Therefore, if the observed crustal anisotropy would be caused by a set of faults it would support a set of faults cutting through FZ. Alternatively, anisotropy could be related to the emplacement of dykes, which are the dominant feature at 1 to 3 km depth in oceanic crust. One interpretation might therefore be that crustal anisotropy reflects J-shaped ridges migrating into the transform domain. However, one must be careful in interpreting the crustal anisotropy as it is derived from two crossing profiles.

Another interesting feature is the lack of any apparent upper mantle anisotropy. Gaherty et al. (2004) observed 3.4% of upper mantle anisotropy in the North Atlantic to the south of Bermuda and in the Pacific mantle anisotropy is a striking feature, with values reaching 6-7% in short offset experiments at the East Pacific Rise (Dunn & Toomey, 1997; Dunn et al., 2000). Therefore, the absence of any anisotropy is a puzzling feature and it might therefore be reasonably to argue that mantle velocity along the fast direction and hence along the fracture zone might be with 7.9-8.1 km/s rather low. However, as stresses rotate over a short distance when approaching a transform fault (Morgan & Parmentier, 1984), mantle flow might be distorted along fracture zones and hence anisotropic pattern. In general, a velocity of ~8 km/s is in the range of observations from mature lithosphere when being sampled along ridge parallel profile (e.g., Davy et al., 2020; Gaherty et al. 2004) and much lower when compared to, for example, a flow line profile at 2°S where Vaddineni et al. (2021) observed in 20 to 30 Myr old lithosphere an upper mantle velocity of ~8.2 km/s. Observations obtained from the travel times of Pn arrivals of regional earthquakes recorded at moored hydrophones support this discrepancy, revealing for equatorial upper mantle a seismic velocity of 7.7 km/s in the slow and 8.4 km/s in the fast direction (de Melo et al., 2020). Therefore, it might be reasonable to suggest that some small degree of uppermost hydration may occur along the SPFZ to explain somewhat lower mantle velocity in the fast direction of anisotropy.

7 Conclusions

We presented new constraints from seismic reflection and wide-angle data surveying the crustal and upper mantle structure along and across the St. Paul fracture zone, one of the largest transform faults in the equatorial Atlantic Ocean. High-resolution P-wave travel time tomography revealed a number of key observations:

1.) Crustal structure along the fracture zone shows the typical layering of magmatically accreted oceanic crust with a crustal thickness of 5 to 5.5 km, a clearly defined seismic Moho and an upper mantle velocity of ~8 km/s.

2.) Crustal thickness across the fracture zone is in the order of 5 to 6 km, showing only a few hundreds of meters of crustal thinning in the vicinity of the St. Paul fracture zone. However, crust at St. Paul is slightly thinner than anywhere else along the line. Nevertheless, the roughly 200 km long well-resolved part of the fracture zone crossing profile did not show the same features and strong crustal thickness variation of 2-4 km found along the active Mid-Atlantic Ridge elsewhere (e.g., Canales et al., 2000; Dannowski et al., 2011; Hooft et al., 2000; Planert et al., 2009) and thus did not show strong evidence supporting decreased melt production and hence occurrence of magmatically starved crust at transform faults (e.g., Lin et al., 1990; Tolstoy et al., 1993).

3.) Crustal seismic velocities along St. Paul are a few percent slower than farther away from it. This observation may suggest that crust along the fracture zone has either higher porosity, probably caused by a larger degree of fracturing, or it may reflect anisotropy. Unfortunately, anisotropy is poorly resolved in the two crossing profiles.

4.) Mantle velocity of ~8 km/s along the transform fault did not reveal strong evidence for serpentinization of the uppermost mantle below the FZ, a feature which has previously been reported for a number of Atlantic fracture zones (e.g., Detrick et al., 1993) and was interpreted in terms of highly fracture and hydrated lithosphere. However, with ~8 km/s upper mantle velocity it is only slightly faster along the transform fault that with ~7.95 km/s across it, hardly showing any evidence for a strong mantle anisotropy, which is believed to be an intrinsic feature of the ocean lithosphere formed by seafloor spreading.

We prefer to interpret our observation with respect to a model where magmatically starved and tectonically disruptive lithosphere envisioned for transform faults (e.g., Detrick et al., 1993) is magmatically augmented at the proximal ridge-transform intersection before transform crust is turning into a fracture zone. Such a scenario has recently been envisioned to explain the fact that world-wide transform faults are several hundreds of meters deeper than their adjacent fracture zones and is supported by high-resolution bathymetry, showing a phase of accretion at RTIs (Grevemeyer et al., 2021). Marjanović et al. (2020) suggested that this phase of accretion is probably controlled by dyke propagation along the adjacent spreading ridge into the transform fault domain. Therefore, lithosphere found today in the St. Paul FZ has been magmatically overprinted while passing along its eastern RTI, explaining why crust along the St. Paul FZ reflects magmatically accreted lithosphere.

Appendix

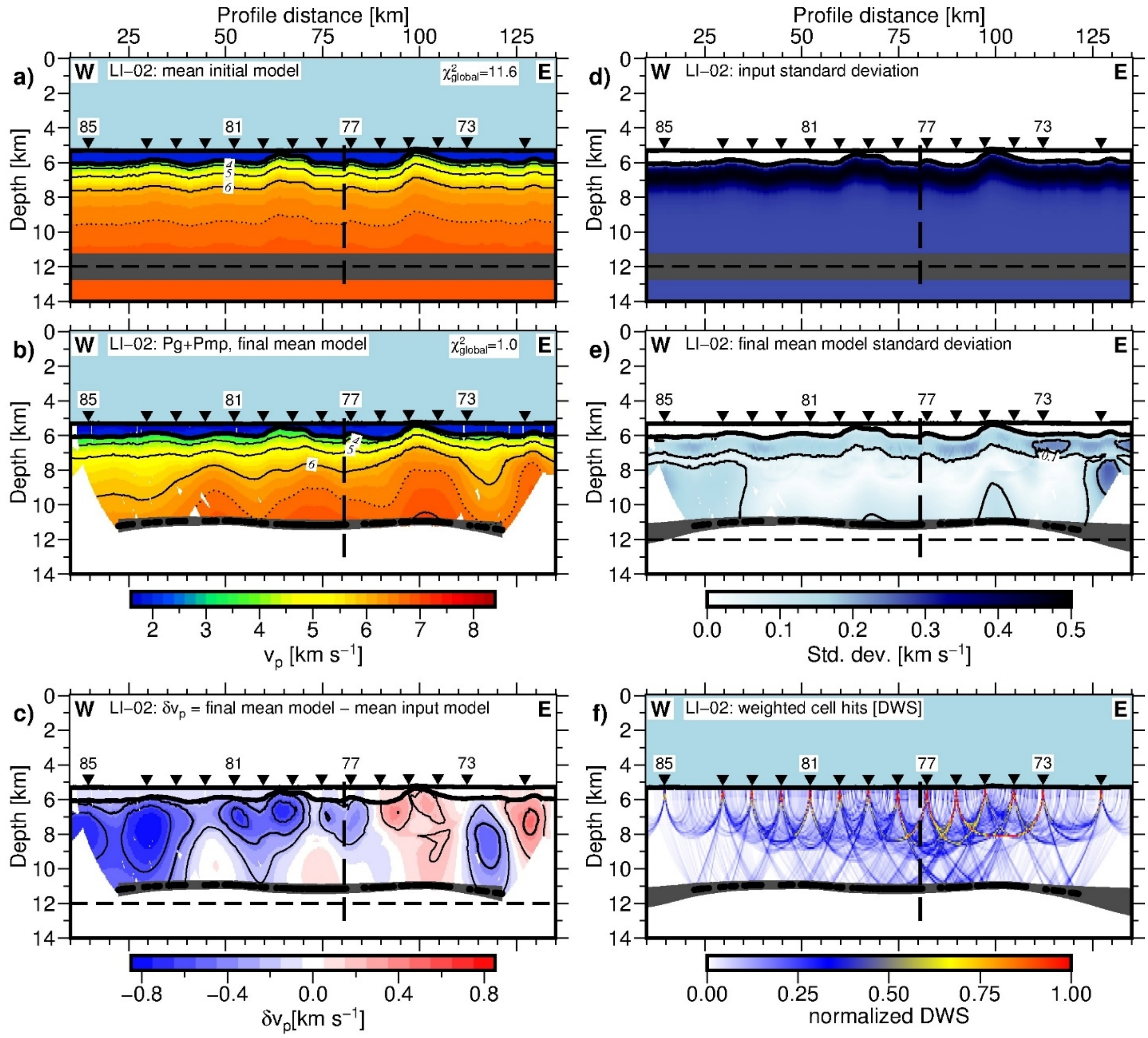

Figure A1: Results from Monte Carlo analysis for the line LI-02 along St. Paul FZ (Fig. 1c): **(a)** Mean initial crustal velocity model (Grevemeyer et al., 2018). **(b)** Mean final crustal velocity model obtained by cumulative inversion of Pg and PmP arrivals. The velocity contour is 1 km/s starting from 4 km/s. **(c)** Velocity deviation between mean final and mean initial model (final - initial). The contour interval is 0.2 km/s starting at 0.2 km/s. **(d)** The initial standard deviation of the mean input velocity model. **(e)** The standard deviation of the final mean model. The contour interval is 0.1 km/s. **(f)** Weighted cell hits (DWS) of the final mean model. Black dots, horizontal black dashed line and grey shading denote the modelled Moho reflection points, the mean initial flat Moho and the Moho standard deviation, respectively. All remaining elements are the same as in Figure 5.

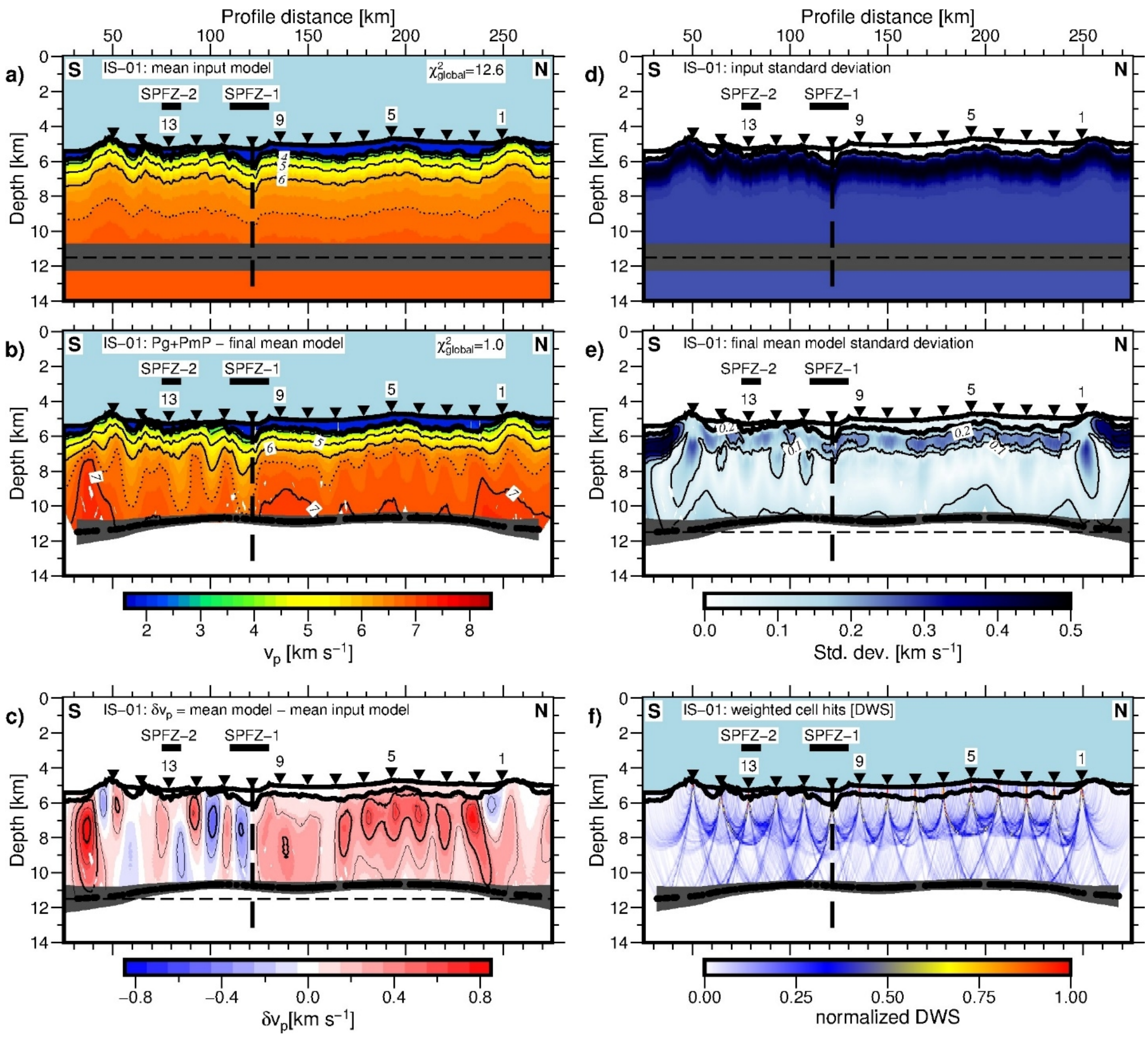

Figure A2: MCA results for line IS-01 across SPFZ (Fig. 1b): All figure elements are the same as in Figure A1 and Figure 6.

Acknowledgements

This research was funded by the German Science Foundation (DFG grant MerMET 15-93) and the European Research Council under the European Union's Seventh Framework Programme (FP7/2007-2013) under Advance Grant agreement no. 339442. We would like to thank captains and the crews of the German R/V Maria S. Merian and the French RV Pourquoi-pas? for excellent sea-going support, enabling the successful data acquisition. We further thank Justin Estep, an anonymous reviewer and the associate editor for valuable comments and suggestions that improved this manuscript. All figures are produced with GMT (Wessel et al., 2013). The MCS and OBS data will be made available on the Pangea open access data repository upon the acceptance of the manuscript (LITHOS-data: https://doi.pangaea.de/10.1594/PANGAEA.907944; ILAB-SPARC-data: https://doi.pangaea.de/10.1594/PANGAEA.xxxxxx).

References

Ambos, E.L & Hussong D.M. (1986). Oceanographer transform fault structure compared to that of surrounding oceanic crust: Results from seismic refraction data analysis. *Journal of geodynamics*, 5.1, pp. 79–102. https://doi.org/10.1016/0264-3707(86)90024-4

Bell, R. E., & Buck, W. R. (1992). Crustal control of ridge segmentation inferred from observations of the Reykjanes Ridge. Nature, 357, 583–586. https://doi.org/10.1038/357583a0

Bird, P. (2003). "An updated digital model of plate boundaries". *Geochemistry, Geophysics, Geosystems,* 4.3. https://doi.org/10.1029/2001GC000252

Bonatti, E.,Seyler, M., & Sushevskaya, N. (1993)., A cold suboceanic mantle belt at the Earth equator. *Science* 261, 315-320. https://doi.org/10.1126/science.261.5119.315

Cannat, M. (1993). Emplacement of mantle rocks in the seafloor at mid-ocean ridges, *Journal of Geophysical Research*, 98, 4163-4172. https://doi.org/10.1029/92JB02221

Cannat, M., Mevel, C., Maia, M., Deplus, C., Durand, C., Gente, P., Agrinier, P., Belarouchi, A., Dubuisson, G., Humler, E., & Reynolds, J.(1995). Thin crust, ultramafic exposures, and rugged faulting patterns at the Mid-Atlantic Ridge (22–24° N), *Geology* 23, 49-52. https://doi.org/10.1130/0091-7613(1995)023<0049:TCUEAR>2.3.CO;2

Carlson, R. L., & Miller, D. J. (2004). Influence of pressure and mineralogy on seismic velocities in oceanic gabbros: Implications for the composition and state of the lower oceanic crust, *Journal of Geophysical Research*, 109, B09205. https://doi.org/10.1029/2003JB002699

Calvert, A.J., & Potts, C.G. (1985). Seismic evidence for hydrothermally altered mantle beneath old crust in the Tydeman fracture zone. *Earth and Planetary Science Letters,* 75.4, pp. 439–449. https://doi.org/10.1016/0012-821X(85)90187-6

Canales, J. P., Detrick, R. S., Lin, J., Collins, J. A., & Toomey, D. R. (2000). Crustal and upper mantle seismic structure beneath the rift mountains and across a nontransform offset at the Mid-Atlantic Ridge (35 N). *Journal of Geophysical Research: Solid Earth*, *105*(B2), 2699-2719. https://doi.org/10.1029/1999JB900379

Chen, Y. J. (1992). Oceanic crustal thickness versus spreading rate. *Geophysical Research Letters*, *19*(8), 753-756. https://doi.org/10.1029/92GL00161

Christeson, G. L., Goff, J. A., & Reece, R. S. (2019). Synthesis of oceanic crustal structure from two-dimensional seismic profiles. *Reviews of Geophysics*, 57, 504–529. https://doi.org/10.1029/2019RG000641

Christeson, G. L., Reece, R. S., Kardell, D. A., Estep, J. D., Fedotova, A., & Goff, J. A. (2020). South Atlantic Transect: Variations in Oceanic Crustal Structure at 31° S. *Geochemistry, Geophysics, Geosystems*, *21*(7), e2020GC009017. https://doi.org/10.1029/2020GC009017

Cohen, J.K. , Stockwell, J.W. (2010). CWP/SU: Seismic Unix Release 41: A free package for seismic research and processing: Center for Wave Phenomena, Colorado School of Mines. Available online at https://wiki.seismic-unix.org/

Cormier, M. H., Detrick, R. S., & Purdy, G. M. (1984). Anomalously thin crust in oceanic fracture zones: New seismic constraints from the Kane fracture zone. *Journal of Geophysical Research: Solid Earth*, *89*(B12), 10249-10266. https://doi.org/10.1029/JB089iB12p10249

Creager, K. C., & Dorman, L. M. (1982). Location of instruments on the seafloor by joint adjustment of instrument and ship positions. *Journal of Geophysical Research: Solid Earth*, *87*(B10), 8379-8388. https://doi.org/10.1029/JB087iB10p08379

Dalton, C. A., Langmuir, C. H., & Gale, A. (2014). Geophysical and geochemical evidence for deep temperature variations beneath mid-ocean ridges. *Science*, *344*(6179), 80-83. https://www.doi.org/10.1126/science.1249466

Dannowski, A., Grevemeyer, I., Phipps Morgan, J., Ranero, C. R., Maia, M., & Klein, G. (2011). Crustal structure of the propagating TAMMAR ridge segment on the Mid-Atlantic Ridge, 21.5 N. *Geochemistry, Geophysics, Geosystems*, *12*(7). https://doi.org/10.1029/2011GC003534

Dannowski, A., Morgan, J. P., Grevemeyer, I., & Ranero, C. R. (2018). Enhanced mantle upwelling/melting caused segment propagation, oceanic core complex die off, and the death of a transform fault: The Mid-Atlantic Ridge at 21.5 N. *Journal of Geophysical Research: Solid Earth*, *123*(2), 941-956. https://doi.org/10.1002/2017JB014273

Davy, R. G., Collier, J. S., Henstock, T. J., VoiLA Consortium, Rietbrock, A., Goes, S., et al. (2020). Wide-angle seismic imaging of two modes of crustal accretion in mature Atlantic Ocean crust. *Journal of Geophysical Research: Solid Earth*, *125*(6), e2019JB019100. https://doi.org/10.1029/2019JB019100

de Melo, G. W., Parnell-Turner, R., Dziak, R. P., Smith, D. K., Maia, M., do Nascimento, A. F., & Royer, J. Y. (2021). Uppermost Mantle Velocity beneath the Mid-Atlantic Ridge and Transform Faults in the Equatorial Atlantic Ocean. *Bulletin of the Seismological Society of America*, *111*(2), 1067-1079. https://doi.org/10.1785/0120200248

Detrick Jr, R. S., & Purdy, G. M. (1980). The crustal structure of the Kane fracture zone from seismic refraction studies. *Journal of Geophysical Research: Solid Earth*, *85*(B7), 3759-3777. https://doi.org/10.1029/JB085iB07p03759

Detrick, R. S., Cormier, M. H., Prince, R. A., Forsyth, D. W., & Ambos, E. L. (1982). Seismic constraints on the crustal structure within the Vema fracture zone. *Journal of Geophysical Research: Solid Earth*, *87*(B13), 10599-10612. https://doi.org/10.1029/JB087iB13p10599

Detrick, R. S., White, R. S., & Purdy, G. M. (1993). Crustal structure of North Atlantic fracture zones. *Reviews of Geophysics*, *31*(4), 439-458. https://doi.org/10.1029/93RG01952

Dunn, R. A., & Toomey, D. R. (1997). Seismological evidence for three-dimensional melt migration beneath the East Pacific Rise. *Nature*, *388*(6639), 259-262. https://doi.org/10.1038/40831

Dunn, R. A., & Toomey, D. R. (2001). Crack-induced seismic anisotropy in the oceanic crust across the East Pacific Rise (9 30′ N). *Earth and Planetary Science Letters*, *189*(1-2), 9-17. https://doi.org/10.1016/S0012-821X(01)00353-3

Dunn, R. A., Toomey, D. R., & Solomon, S. C. (2000). Three-dimensional seismic structure and physical properties of the crust and shallow mantle beneath the East Pacific Rise at 9° 30'N. *Journal of Geophysical Research: Solid Earth*, *105*(B10), 23537-23555. https://doi.org/10.1029/2000JB900210

Gaherty, J. B., Lizarralde, D., Collins, J. A., Hirth, G., & Kim, S. (2004). Mantle deformation during slow seafloor spreading constrained by observations of seismic anisotropy in the western Atlantic. *Earth and Planetary Science Letters*, *228*(3-4), 255-265. https://doi.org/10.1016/j.epsl.2004.10.026

Gregory, E., Singh, S. C., Marjanović, M., & Wang, Z. (2021). Serpentinized peridotite versus thick mafic crust at the Romanche oceanic transform fault, *Geology,* 49 (9): 1132–1136. https://doi.org/10.1130/G49097.1

Grevemeyer, I. (2020). Upper Mantle Structure beneath the Mid-Atlantic Ridge from Regional Waveform Modeling. *Bulletin of the Seismological Society of America*, *110*(1), 18-25. https://doi.org/10.1785/0120190080

Grevemeyer, I., Kaul, N., Villinger, H., & Weigel, W. (1999). Hydrothermal activity and the evolution of the seismic properties of upper oceanic crust. *Journal of Geophysical Research: Solid Earth*, *104*(B3), 5069-5079. https://doi.org/10.1029/1998JB900096

Grevemeyer, I., Ranero, C. R., & Ivandic, M. (2018). Structure of oceanic crust and serpentinization at subduction trenches. *Geosphere*, *14*(2), 395-418. https://doi.org/10.1130/GES01537.1

Grevemeyer, I., Rüpke, L.H., Morgan, J.P., Iyer, K, & Devey, C.W. (2021). Extensional tectonics and two-stage crustal accretion at oceanic transform faults. *Nature,* 591, 402–407. https://doi.org/10.1038/s41586-021-03278-9

Grevemeyer, I., Singh, S.C., Papenberg, C. (2019). Ocean bottom seismometer and ocean bottom hydrophone seismic refraction and wide angle data from profile P02 of Maria S. Merian cruise MSM69 with links to sgy data files. PANGAEA. https://doi.org/10.1594/PANGAEA.907944

Grion, S., Exley, R., Manin, M., Miao, X., Pica, A. L., Wang, Y., et al. (2007). Mirror imaging of OBS data. *first break*, *25*(11). https://doi.org/10.3997/1365-2397.2007028

Harding, J. L., Van Avendonk, H. J., Hayman, N. W., Grevemeyer, I., Peirce, C., & Dannowski, A. (2017). Magmatic-tectonic conditions for hydrothermal venting on an ultraslow-spread oceanic core complex. *Geology*, *45*(9), 839-842. https://doi.org/10.1130/G39045.1

Hooft, E. E. E., Detrick, R. S., Toomey, D. R., Collins, J. A., & Lin, J. (2000). Crustal thickness and structure along three contrasting spreading segments of the Mid-Atlantic

Ridge, 33.5–35 N. *Journal of Geophysical Research: Solid Earth*, *105*(B4), 8205-8226. https://doi.org/10.1029/1999JB900442

James, E. K., Dalton, C. A., & Gaherty, J. B. (2014). R ayleigh wave phase velocities in the A tlantic upper mantle. *Geochemistry, Geophysics, Geosystems*, *15*(11), 4305-4324. https://doi.org/10.1002/2014GC005518

Korenaga, J., Holbrook, W. S., Kent, G. M., Kelemen, P. B., Detrick, R. S., Larsen, H. C., et al. (2000). Crustal structure of the southeast Greenland margin from joint refraction and reflection seismic tomography. *Journal of Geophysical Research: Solid Earth*, *105*(B9), 21591-21614. https://doi.org/10.1029/2000JB900188

Korenaga, J., Kelemen, P. B., & Holbrook, W. S. (2002). Methods for resolving the origin of large igneous provinces from crustal seismology. *Journal of Geophysical Research: Solid Earth*, *107*(B9), ECV-1. https://doi.org/10.1029/2001JB001030

Lin, J., Purdy, G. M., Schouten, H., Sempere, J. C., & Zervas, C. (1990). Evidence from gravity data for focusedmagmatic accretionalong the Mid-Atlantic Ridge. *Nature*, *344*(6267), 627-632. https://doi.org/10.1038/344627a0

Lin, J., & Morgan, J. P. (1992). The spreading rate dependence of three-dimensional mid-ocean ridge gravity structure. *Geophysical Research Letters*, *19*(1), 13-16. https://doi.org/10.1029/91GL03041

Macdonald, K. C., Fox, P. J., Perram, L. J., Eisen, M. F., Haymon, R. M., Miller, S. P., et al. (1988). A new view of the mid-ocean ridge from the behaviour of ridge-axis discontinuities. *Nature*, *335*(6187), 217-225. https://doi.org/10.1038/335217a0

Maia, M., Sichel, S., Briais, A., Brunelli, D., Ligi, M., Ferreira, N., et al. (2016). Extreme mantle uplift and exhumation along a transpressive transform fault. *Nature Geoscience*, *9*(8), 619-623. https://doi.org/10.1038/ngeo2759

Marjanović, M., Singh, S. C., Gregory, E. P., Grevemeyer, I., Growe, K., Wang, Z., et al. (2020). Seismic crustal structure and morphotectonic features associated with the Chain Fracture Zone and their role in the evolution of the equatorial Atlantic region. *Journal of Geophysical Research: Solid Earth*, *125*(10), e2020JB020275. https://doi.org/10.1029/2020JB020275

Matthews, K. J., Müller, R. D., Wessel, P., & Whittaker, J. M. (2011). The tectonic fabric of the ocean basins. *Journal of Geophysical Research: Solid Earth*, *116*(B12). https://doi.org/10.1029/2011JB008413

McKenzie, D. P., & Parker, R. L. (1967). The North Pacific: an example of tectonics on a sphere. *Nature*, *216*(5122), 1276-1280. https://doi.org/10.1038/2161276a0

Mckenzie, D. A. N., & Bickle, M. J. (1988). The volume and composition of melt generated by extension of the lithosphere. *Journal of petrology*, *29*(3), 625-679. https://doi.org/10.1093/petrology/29.3.625

Mehouachi, F., & Singh, S. C. (2018). Water-rich sublithospheric melt channel in the equatorial Atlantic Ocean. *Nature Geoscience*, *11*(1), 65-69. https://doi.org/10.1038/s41561-017-0034-z

Menard, H. W. (1967). Extension of northeastern-Pacific fracture zones. *Science*, *155*(3758), 72-74. https://doi.org/10.1126/science.155.3758.72

Menard, H. W. (1955). Deformation of the northeastern Pacific basin and the west coast of North America. *Geological Society of America Bulletin*, *66*(9), 1149-1198. https://doi.org/10.1130/0016-7606(1955)66[1149:DOTNPB]2.0.CO;2

Minshull, T. A., White, R. S., Mutter, J. C., Buhl, P., Detrick, R. S., Williams, C. A., & Morris, E. (1991). Crustal structure at the Blake Spur fracture zone from expanding spread profiles. *Journal of Geophysical Research: Solid Earth*, *96*(B6), 9955-9984. https://doi.org/10.1029/91JB00431

Morgan, W. J. (1968). Rises, trenches, great faults, and crustal blocks. *Journal of Geophysical Research*, *73*(6), 1959-1982. https://doi.org/10.1029/JB073i006p01959

Morgan, J. P., & Parmentier, E. M. (1984). Lithospheric stress near a ridge-transform intersection. *Geophysical Research Letters*, *11*(2), 113-116. https://doi.org/10.1029/GL011i002p00113

Moser, T. J. (1991). Shortest path calculation of seismic rays. *Geophysics*, *56*(1), 59-67. https://doi.org/10.1190/1.1442958

Moser, T. J., Nolet, G., & Snieder, R. (1992). Ray bending revisited. *Bulletin of the Seismological Society of America*, *82*(1), 259-288.

Müller, R. D., Sdrolias, M., Gaina, C., & Roest, W. R. (2008). Age, spreading rates, and spreading asymmetry of the world's ocean crust. *Geochemistry, Geophysics, Geosystems*, *9*(4). https://doi.org/10.1029/2007GC001743

Muller, M. R., Minshull, T. A., & White, R. S. (1999). Segmentation and melt supply at the Southwest Indian Ridge. *Geology*, *27*(10), 867-870. https://doi.org/10.1130/0091-7613(1999)027<0867:SAMSAT>2.3.CO;2

Niu, X., Ruan, A., Li, J., Minshull, T. A., Sauter, D., Wu, Z., et al. (2015). Along-axis variation in crustal thickness at the ultraslow spreading S outhwest I ndian R idge (50° E) from a wide-angle seismic experiment. *Geochemistry, Geophysics, Geosystems*, *16*(2), 468-485. https://doi.org/10.1002/2014GC005645

Paige, C. C., & Saunders, M. A. (1982). LSQR: An algorithm for sparse linear equations and sparse least squares. *ACM Transactions on Mathematical Software (TOMS)*, *8*(1), 43-71.

Peirce, C., Reveley, G., Robinson, A. H., Funnell, M. J., Searle, R. C., Simão, N. M., et al. (2019). Constraints on crustal structure of adjacent OCCs and segment boundaries at 13° N on the Mid-Atlantic Ridge. *Geophysical Journal International*, *217*(2), 988-1010. https://doi.org/10.1093/gji/ggz074

Planert, L., Flueh, E. R., & Reston, T. J. (2009). Along-and across-axis variations in crustal thickness and structure at the Mid-Atlantic Ridge at 5 S obtained from wide-angle seismic tomography: Implications for ridge segmentation. *Journal of Geophysical Research: Solid Earth*, *114*(B9). https://doi.org/10.1029/2008JB006103

Potts, C. G., Calvert, A. J., & White, R. S. (1986). Crustal structure of Atlantic fracture zones-III. The Tydeman fracture zone. *Geophysical Journal International*, *86*(3), 909-942. https://doi.org/10.1111/j.1365-246X.1986.tb00668.x

Purdy, G. M. (1983). The seismic structure of 140 Myr old crust in the western central Atlantic Ocean. *Geophysical Journal International*, *72*(1), 115-137. https://doi.org/10.1111/j.1365-246X.1983.tb02808.x

Raitt, M. (1963). The crustal rocks. *The sea*, *3*, 85-102.

Roland, E., Lizarralde, D., McGuire, J. J., & Collins, J. A. (2012). Seismic velocity constraints on the material properties that control earthquake behavior at the Quebrada-Discovery-Gofar transform faults, East Pacific Rise. *Journal of Geophysical Research: Solid Earth*, *117*(B11). https://doi.org/10.1029/2012JB009422

Sandwell, D. T. (1984). Thermomechanical evolution of oceanic fracture zones. *Journal of Geophysical Research: Solid Earth*, *89*(B13), 11401-11413. https://doi.org/10.1029/JB089iB13p11401

Sandwell, D. T., Müller, R. D., Smith, W. H., Garcia, E., & Francis, R. (2014). New global marine gravity model from CryoSat-2 and Jason-1 reveals buried tectonic structure. *Science*, *346*(6205), 65-67. https://doi.org/10.1126/science.1258213

Searle, R. C., Thomas, M. V., & Jones, E. J. W. (1994). Morphology and tectonics of the Romanche Transform and its environs. *Marine Geophysical Researches*, *16*(6), 427-453. https://doi.org/10.1007/BF01270518

Sykes, L. R. (1967). Mechanism of earthquakes and nature of faulting on the mid-oceanic ridges. *Journal of Geophysical Research*, *72*(8), 2131-2153. https://doi.org/10.1029/JZ072i008p02131

Taylor, M. A. J., & Singh, S. C. (2002). Composition and microstructure of magma bodies from effective medium theory. *Geophysical Journal International*, *149*(1), 15-21. https://doi.org/10.1046/j.1365-246X.2002.01577.x

Tolstoy, M., Harding, A. J., & Orcutt, J. A. (1993). Crustal thickness on the Mid-Atlantic Ridge: Bull's-eye gravity anomalies and focused accretion. *Science*, *262*(5134), 726-729. https://doi.org/10.1126/science.262.5134.726

Toomey, D. R., & Foulger, G. R. (1989). Tomographic inversion of local earthquake data from the Hengill-Grensdalur central volcano complex, Iceland. *Journal of Geophysical Research: Solid Earth*, *94*(B12), 17497-17510. https://doi.org/10.1029/JB094iB12p17497

Van Avendonk, H. J., Davis, J. K., Harding, J. L., & Lawver, L. A. (2017). Decrease in oceanic crustal thickness since the breakup of Pangaea. *Nature Geoscience*, *10*(1), 58-61. https://doi.org/10.1038/ngeo2849

Vaddineni, V. A., Singh, S.C., Grevemeyer, I., Audhkhasi, P., & Papenberg, C. (2021). Evolution of the Crustal and upper Mantle seismic structure from 0-27 Ma in the equatorial Atlantic Ocean at 2°43′S. *Journal of Geophysical Research: Solid Earth, e2020JB021390*. https://doi.org/10.1029/2020JB021390

Vine, F. J., & Moores, E. M. (1972). A model for the gross structure, petrology, and magnetic properties of oceanic crust. *Studies in Earth and Space Sciences: A Memoir in Honor of Harry Hammond Hess*, 195-205.

Wessel, P., Smith, W. H., Scharroo, R., Luis, J., & Wobbe, F. (2013). Generic mapping tools: improved version released. *Eos, Transactions American Geophysical Union*, *94*(45), 409-410. https://doi.org/10.1002/2013EO450001

White, R. S., Detrick, R. S., Sinha, M. C., & Cormier, M. H. (1984). Anomalous seismic crustal structure of oceanic fracture zones. *Geophysical Journal International*, *79*(3), 779-798. https://doi.org/10.1111/j.1365-246X.1984.tb02868.x

White, R. S., McKenzie, D., & O'Nions, R. K. (1992). Oceanic crustal thickness from seismic measurements and rare earth element inversions. *Journal of Geophysical Research: Solid Earth*, *97*(B13), 19683-19715. https://doi.org/10.1029/92JB01749

Whitmarsh, R. B. (1978). Seismic refraction studies of the upper igneous crust in the North Atlantic and porosity estimates for layer 2. *Earth and Planetary Science Letters*, *37*(3), 451-464. https://doi.org/10.1016/0012-821X(78)90061-4

Whitmarsh, R. B., & Calvert, A. J. (1986). Crustal structure of Atlantic fracture zones—I. The Charlie-Gibbs fracture zone. *Geophysical Journal International*, *85*(1), 107-138. https://doi.org/10.1111/j.1365-246X.1986.tb05174.x

Wilson, J. T. (1965). A new class of faults and their bearing on continental drift. *Nature*, *207*(4995), 343-347.

Yilmaz, Ö. (2001). *Seismic data analysis: Processing, inversion, and interpretation of seismic data*. Society of exploration geophysicists.

Supporting Information for "Seismic structure of the St. Paul Fracture Zone and Late Cretaceous to Mid Eocene oceanic crust in the equatorial Atlantic Ocean near 18°W"

Kevin Growe[1,2], Ingo Grevemeyer[1], Satish Singh[2], Milena Marjanović[2], Emma P. M. Gregory[2], Cord Papenberg[1], Venkata Vaddineni[2], Laura Gómez de la Peña[1], and Zhikai Wang[2]

[1]GEOMAR Helmholz Centre for Ocean Research Kiel

[2]Université de Paris, Institut de Physique du Globe de Paris; CNRS, Paris, France

Contents of this file

1. Figures S1 to S15
2. Tables S1 to S3

Introduction

Table S1 lists the acquisition parameters of the two seismic refraction lines used for this study. Figures S1a-S1n and S2a-S2o show all OBS record sections with corresponding traveltime fits and raypaths, for both lines, LI-02 and IS-01, respectively. Figures S3 and S4 illustrate the OBS mirrow image and the post-stack time-migrated MCS sections, that were used to constrain the basement depth below the seafloor for line LI-02 and IS-01, respectively. Figure S5 depicts the porosity-velocity-aspect-ratio dependencies computed with a differential effective medium analysis after Taylor and Singh (2002). Figures S6-S15 show the results of several resolution tests for the tomographic inversion: 1. crustal checkerboard tests, 2. Moho regularization tests 3. Moho resolution tests and 4. mantle resolution tests. Their results and implications are briefly discussed in the main text. Table S2 lists all discretization, forward and inversion parametrization used for this study. And finally, Table S3 compares the different parametrization for the PmP inversion.

Table S1. Refraction line acquisition parameters.

Parameter/Line	**LI-02**	**IS-01**
Profile length [km]	143	350
Number of OBS	14	15
Mean OBS-spacing [km]	8.6	14.2
Number of shots	875	1167
Shot spacing [km]	~0.16	0.3
Sampling frequency [Hz]	250	250
Total airgun volume [l]	86	82
Airgun array towing depth [m]	7.5	10

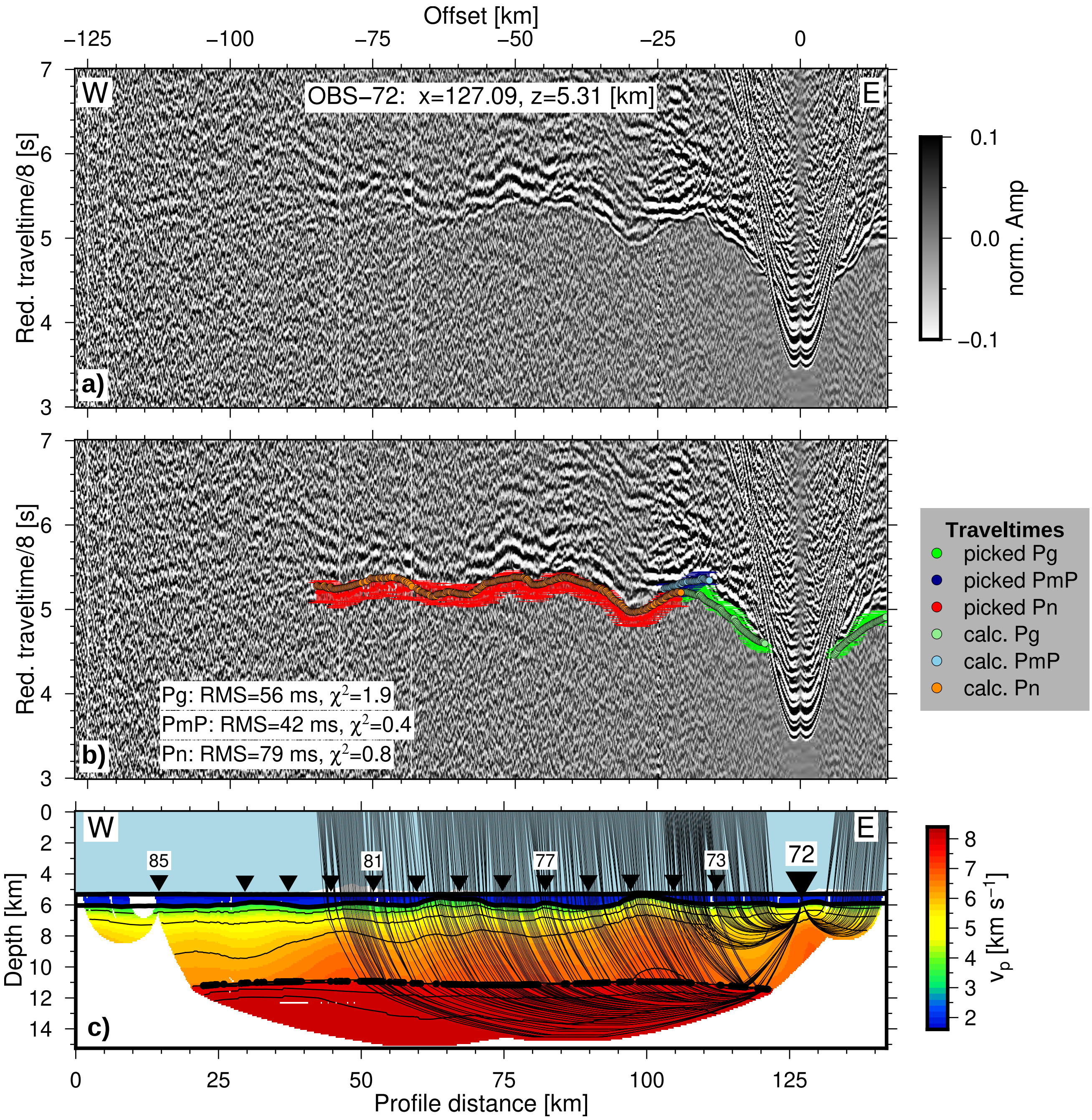

Figure S1a. **(a)** Record section of OBS 72 (LI-02) with **(b)** superimposed picked (small dots with error bars, indicating pick uncertainty) and computed traveltimes (larger dots). The time is reduced with a reduction velocity of 8 km/s. The amplitude is normalized and clipped to 10 %. **(c)** Corresponding raypaths superimposed on final velocity model. The velocity contour interval is 1.0 km/s for the crust, starting with 4 km/s, and 0.1 km/s for the mantle, starting at 8.0 km/s. Remaining figure elements are the same as in Fig. 4 in the main text.

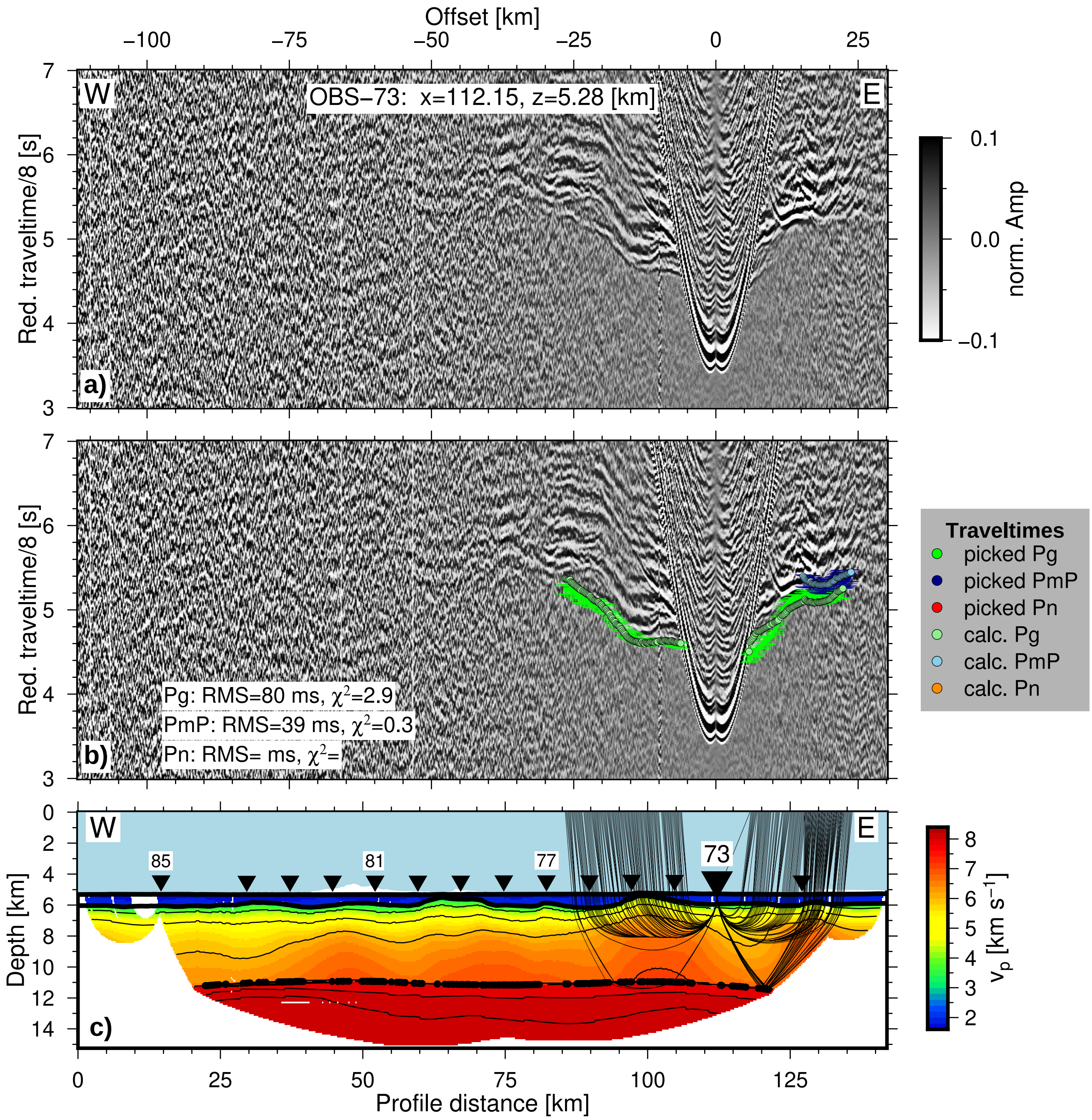

Figure S1b. Record section, traveltime fit and raypaths for OBS 73 (LI-02).

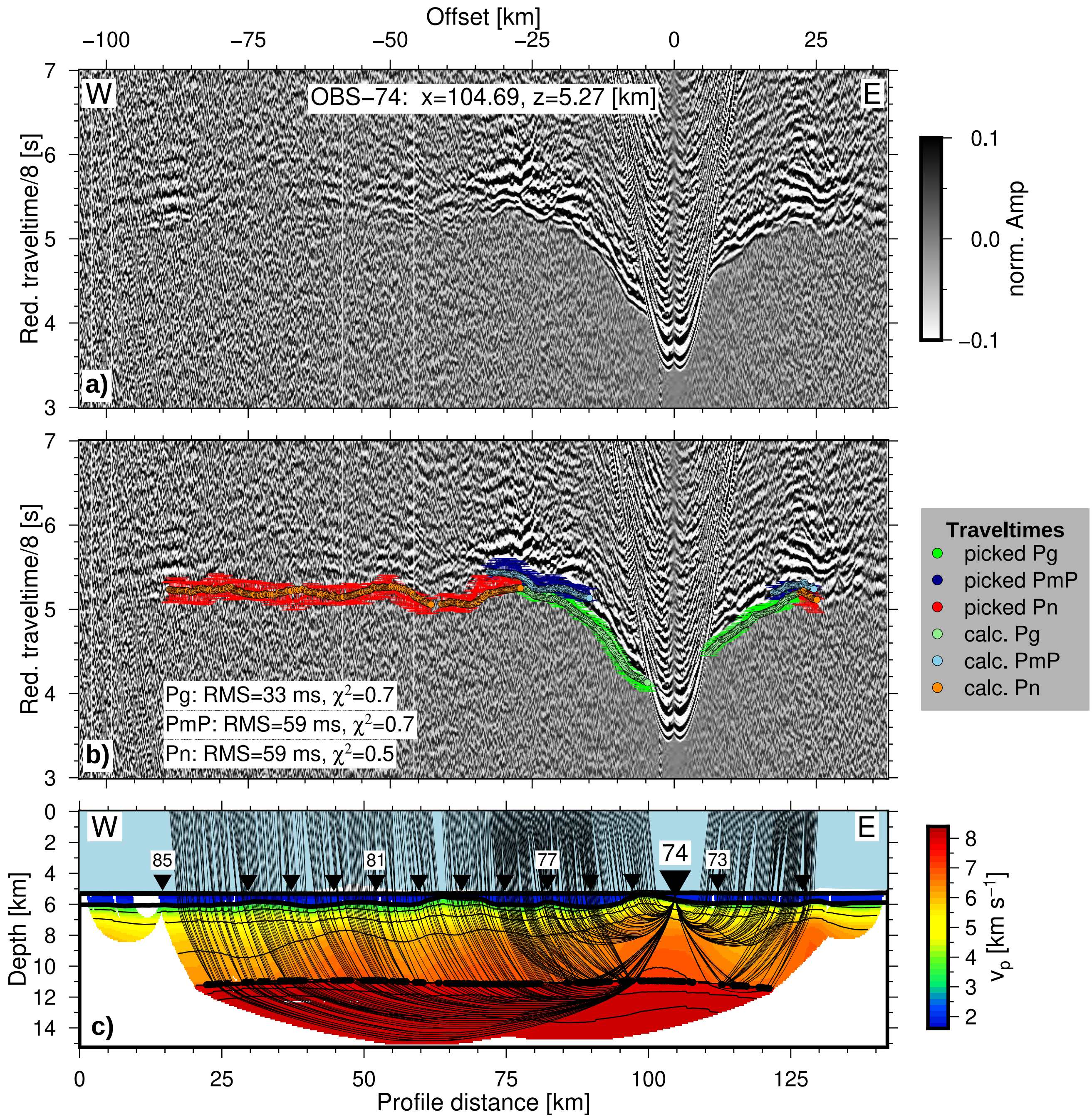

Figure S1c. Record section, traveltime fit and raypaths for OBS 74 (LI-02).

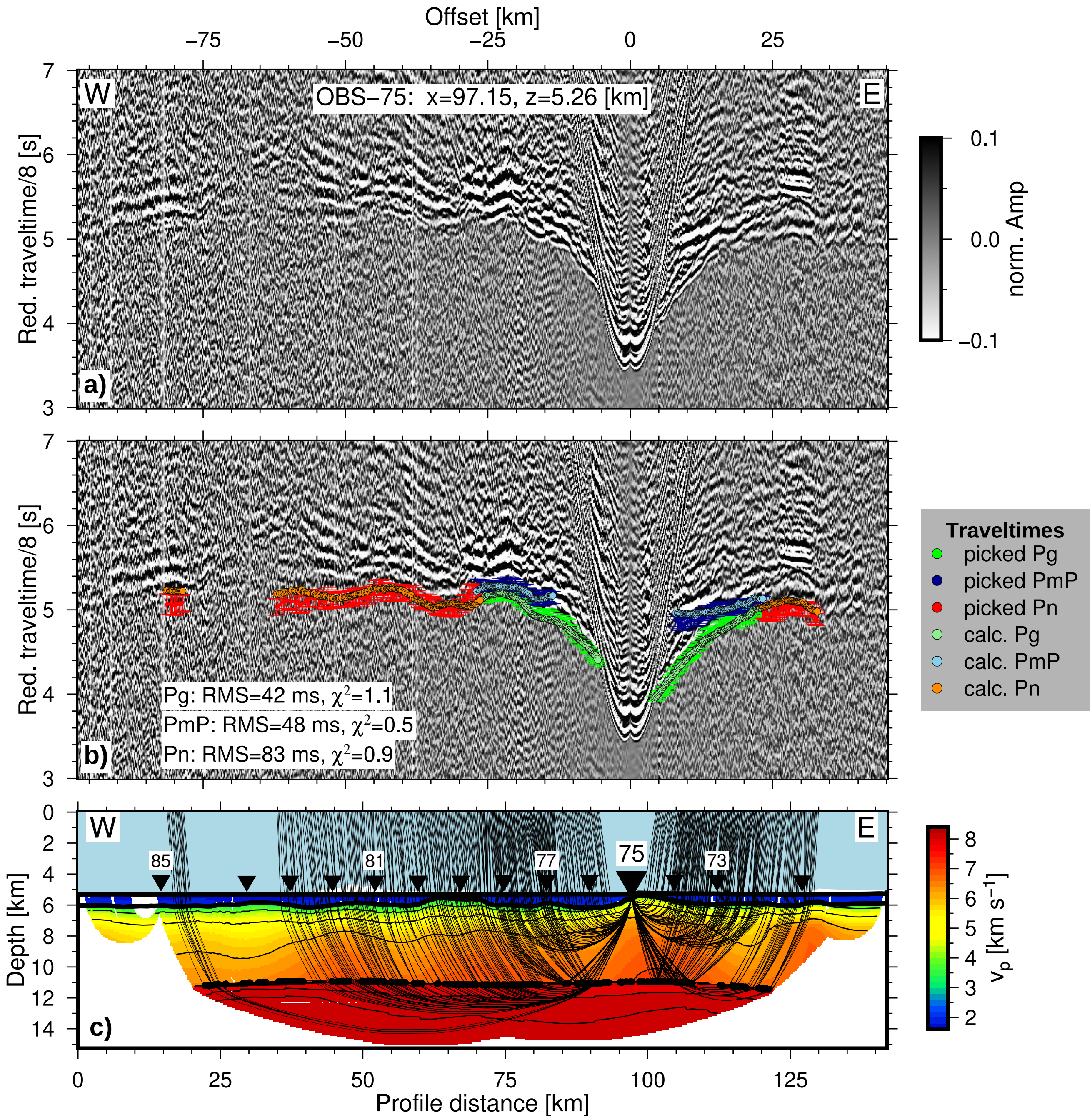

Figure S1d. Record section, traveltime fit and raypaths for OBS 75 (LI-02).

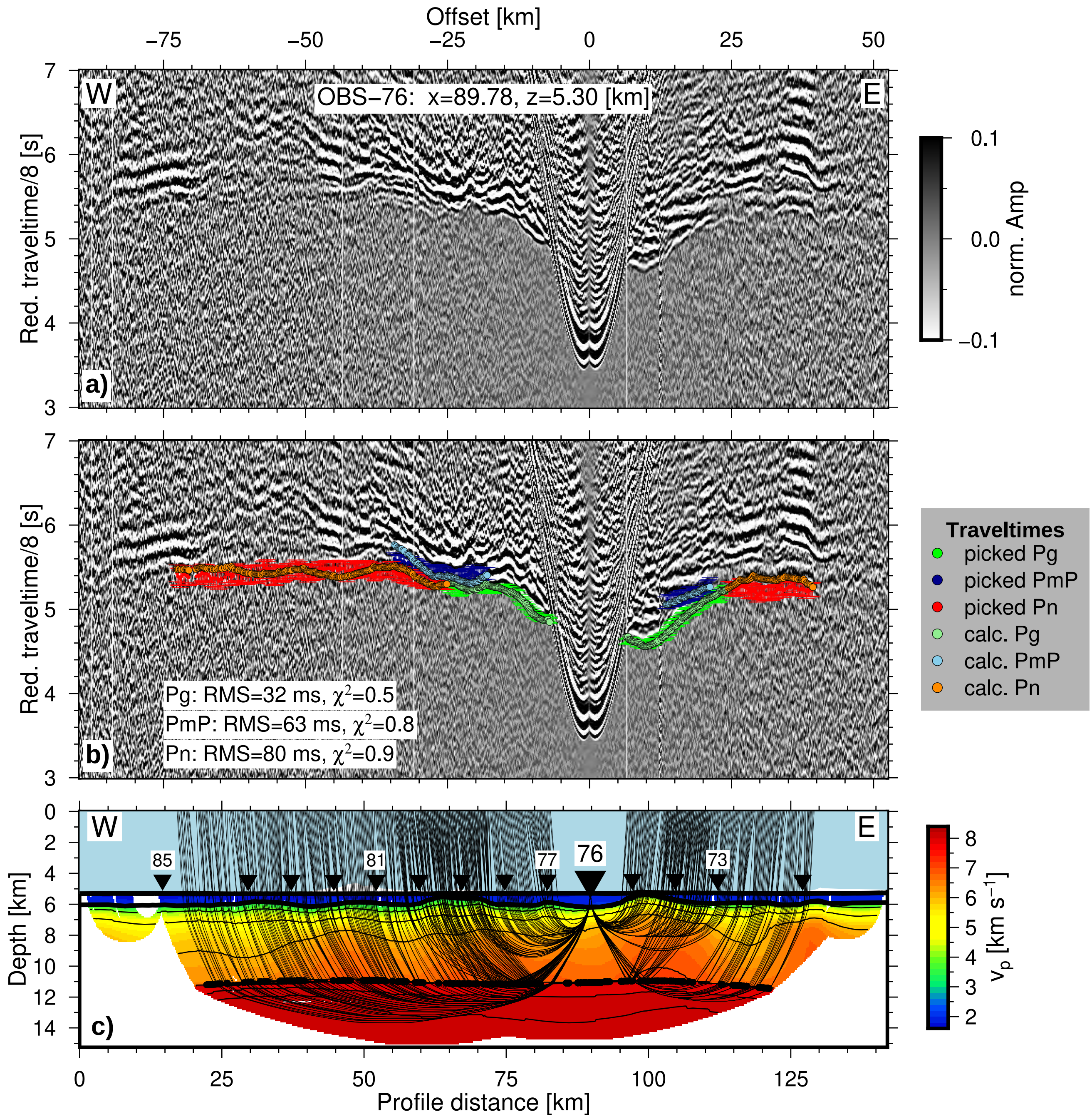

Figure S1e. Record section, traveltime fit and raypaths for OBS 76 (LI-02).

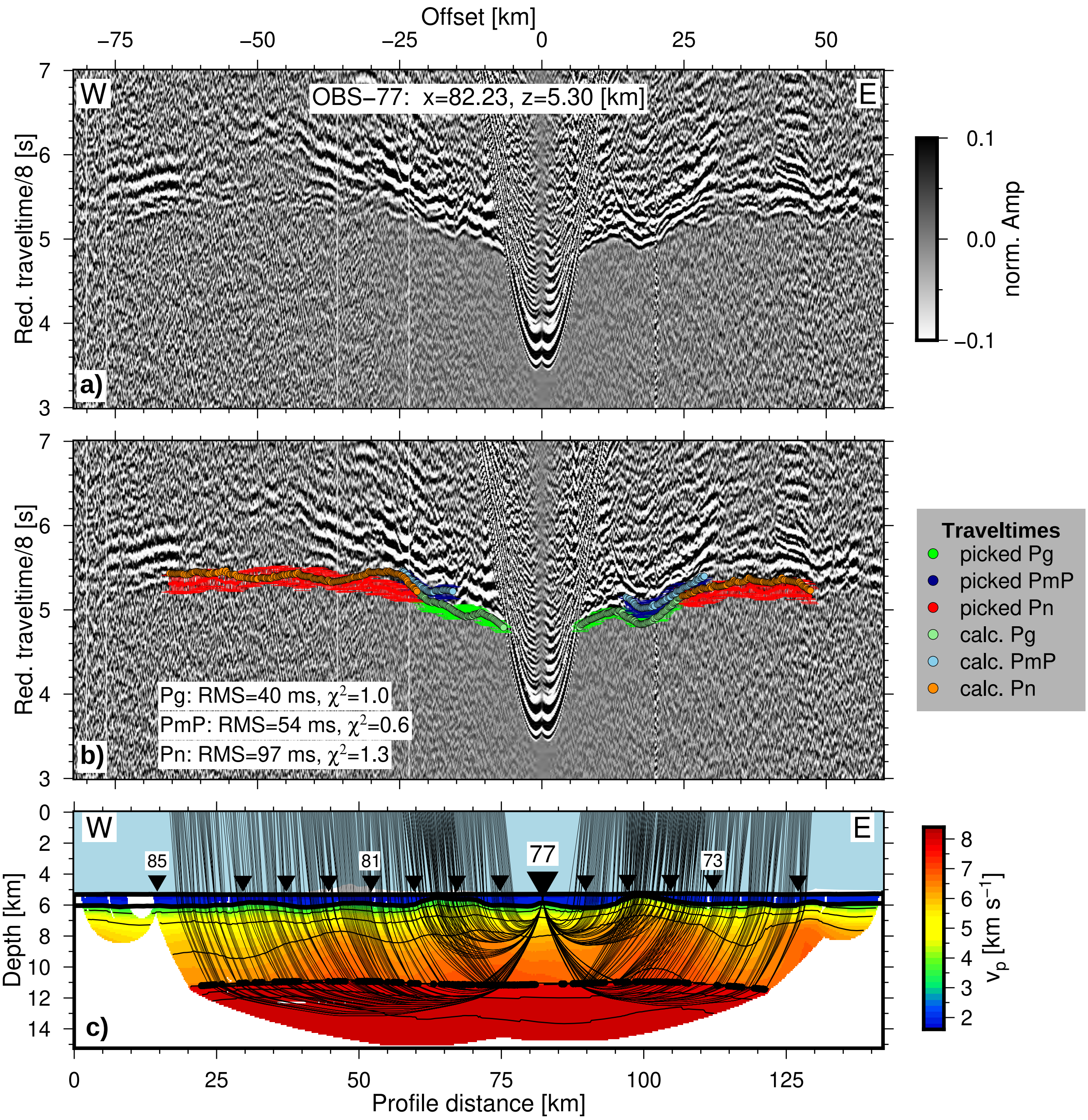

Figure S1f. Record section, traveltime fit and raypaths for OBS 77 (LI-02).

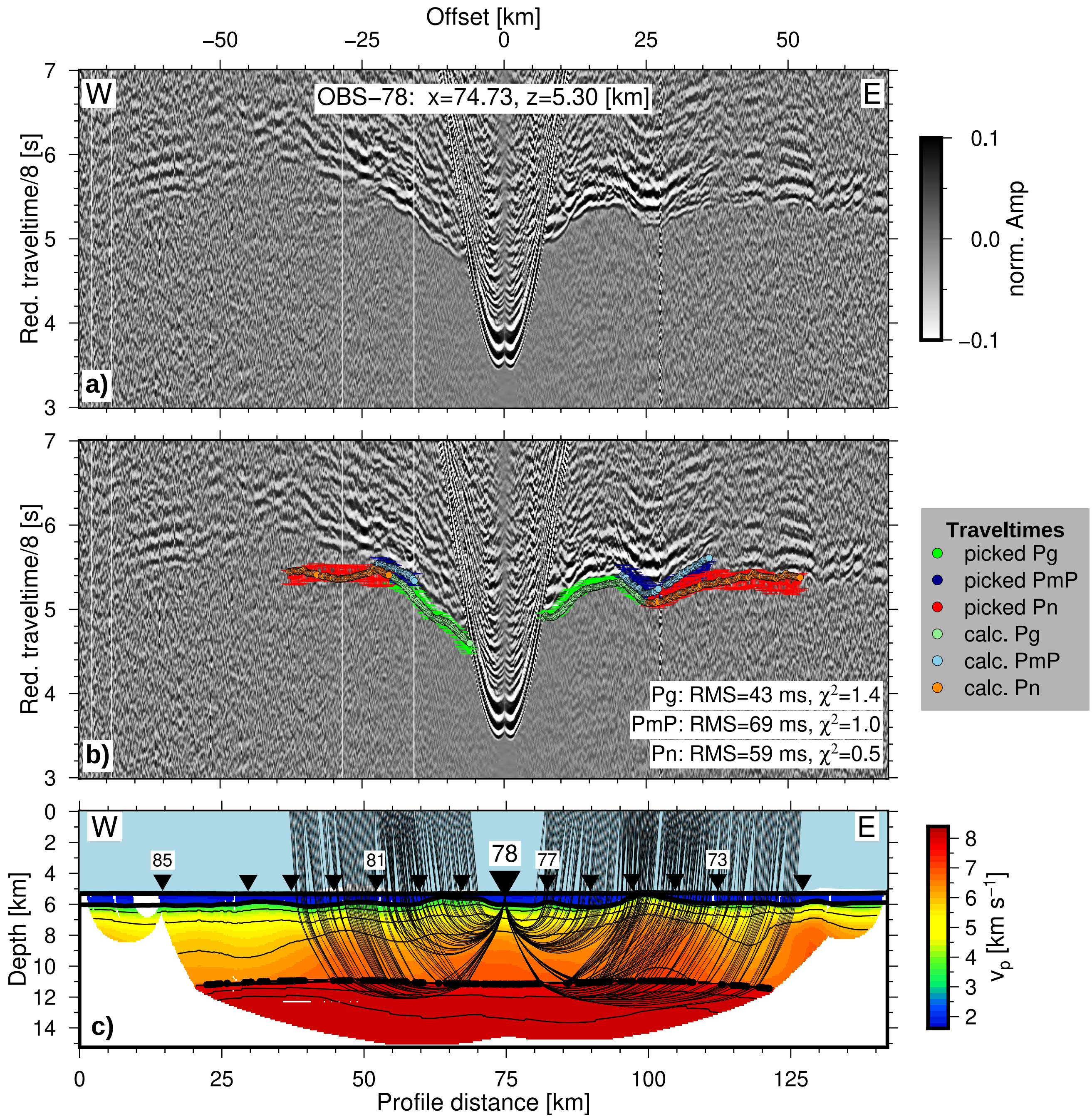

Figure S1g. Record section, traveltime fit and raypaths for OBS 78 (LI-02).

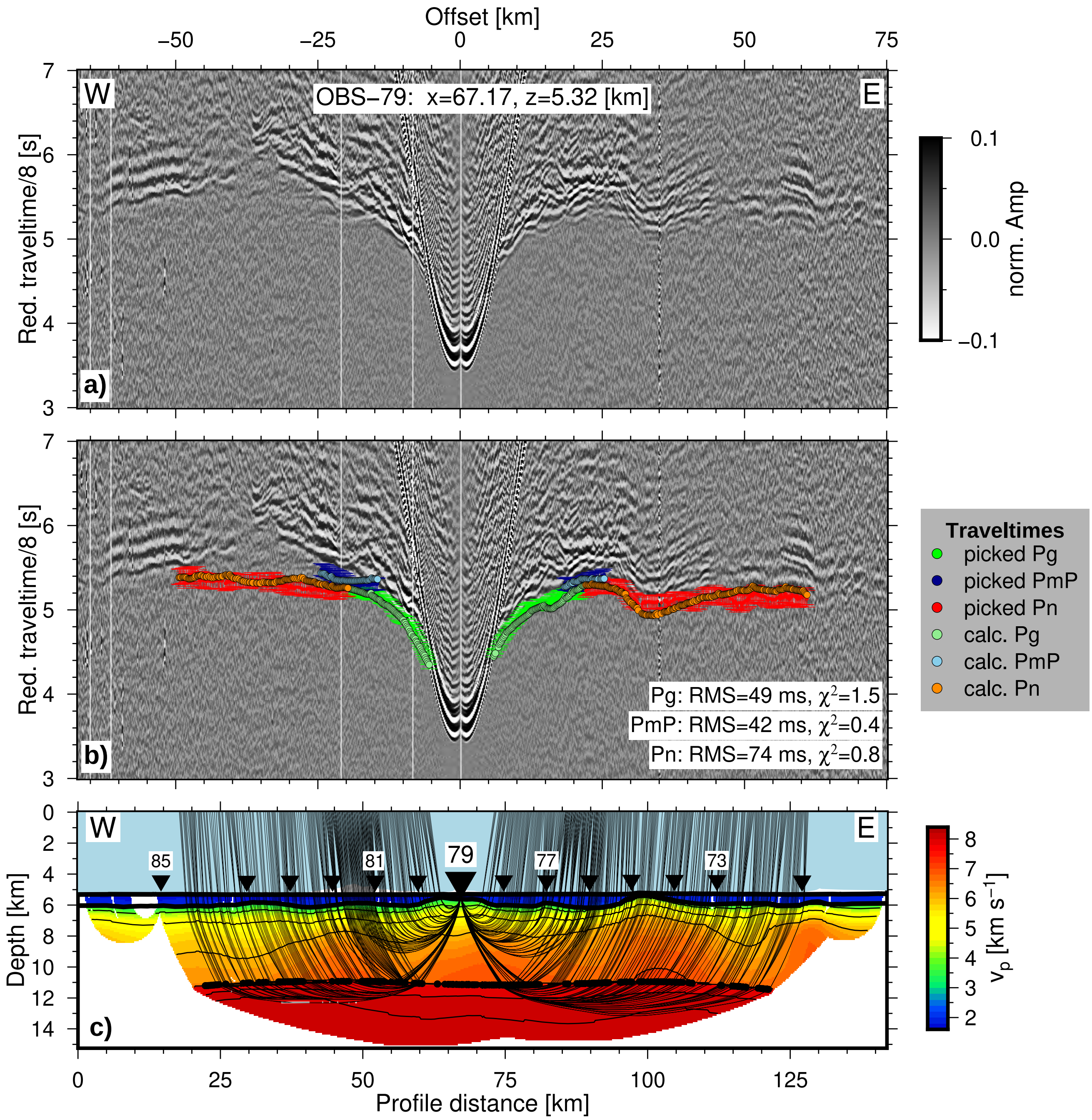

Figure S1h. Record section, traveltime fit and raypaths for OBS 79 (LI-02).

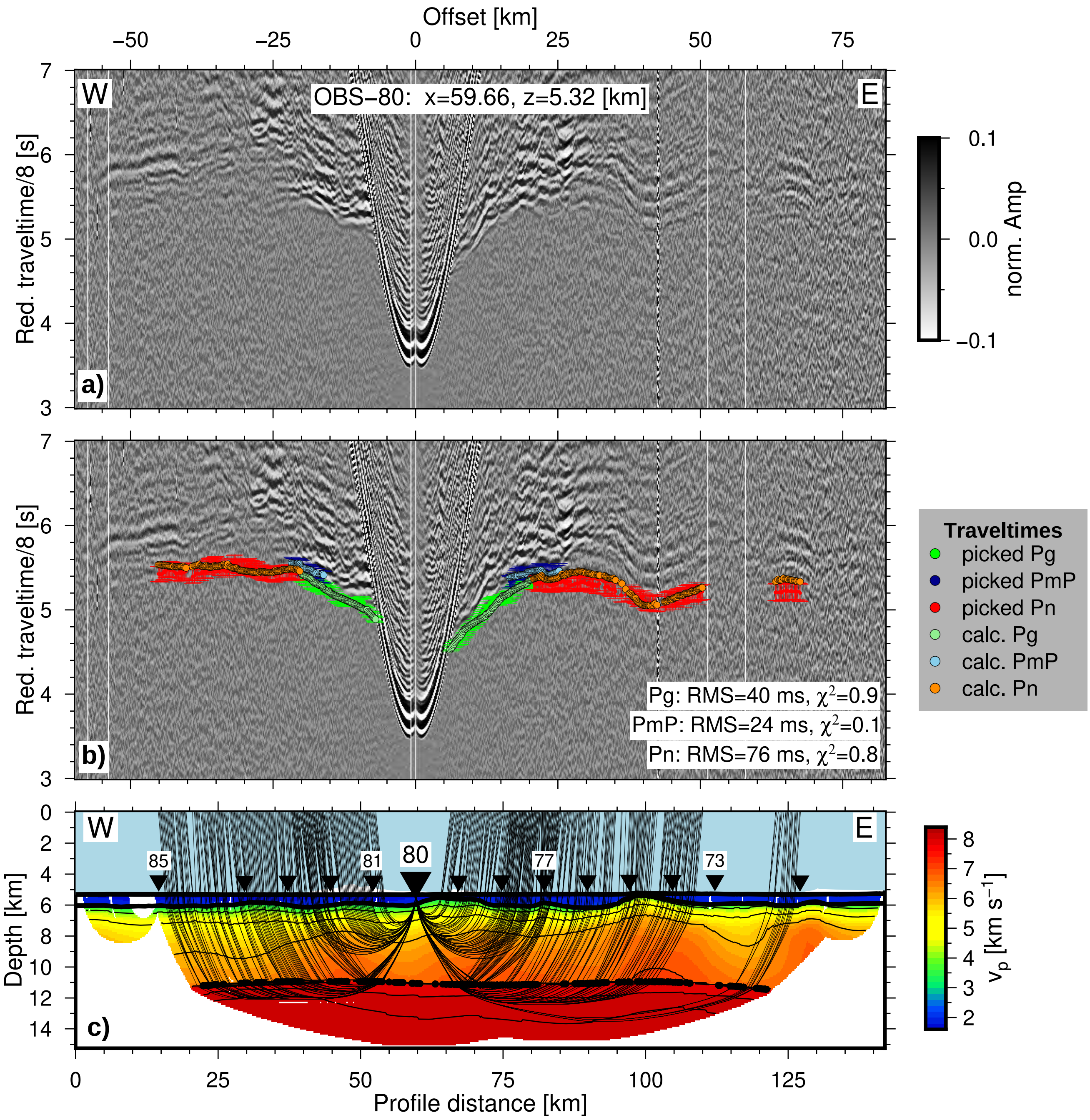

Figure S1i. Record section, traveltime fit and raypaths for OBS 80 (LI-02).

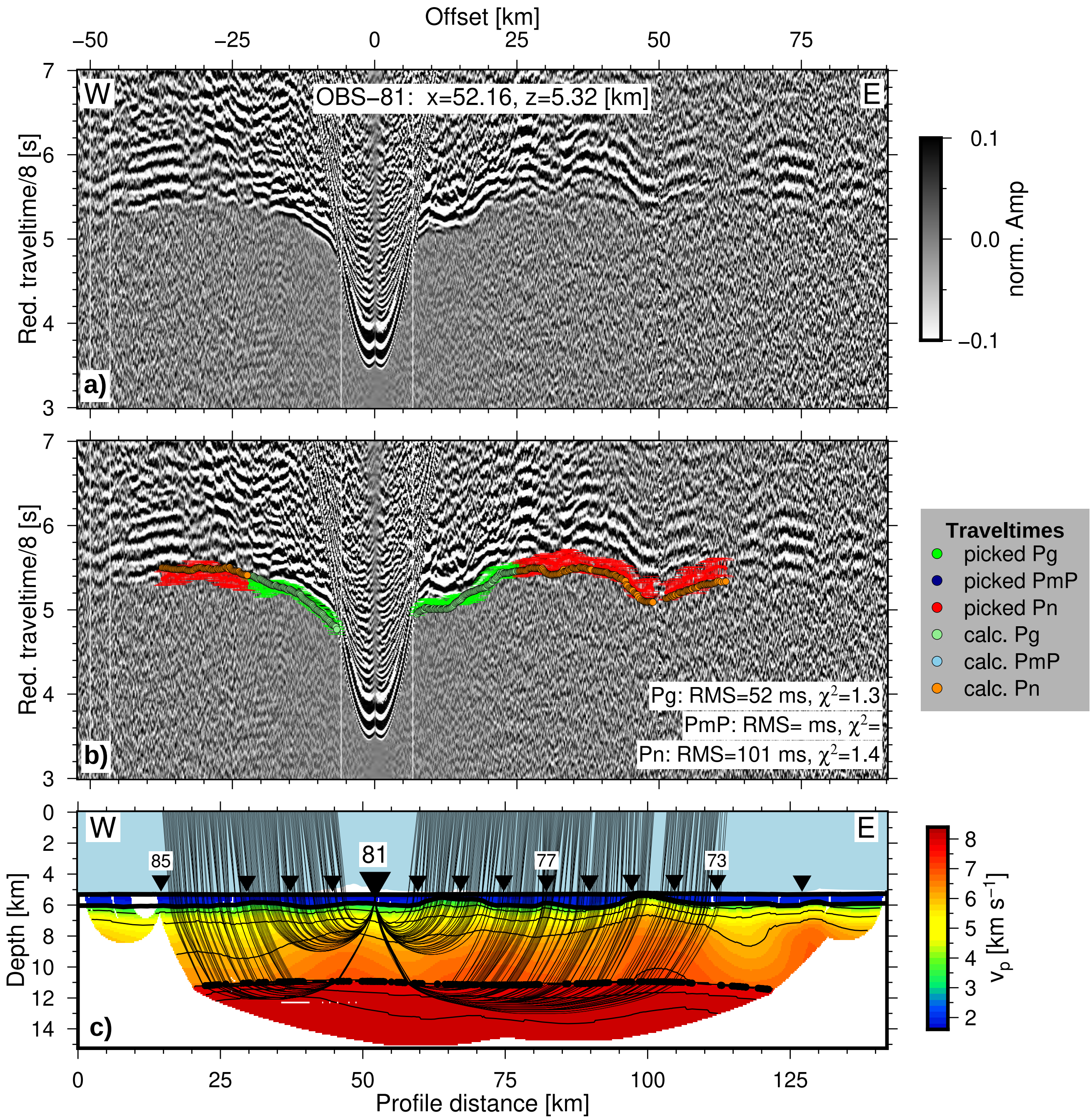

Figure S1j. Record section, traveltime fit and raypaths for OBS 81 (LI-02).

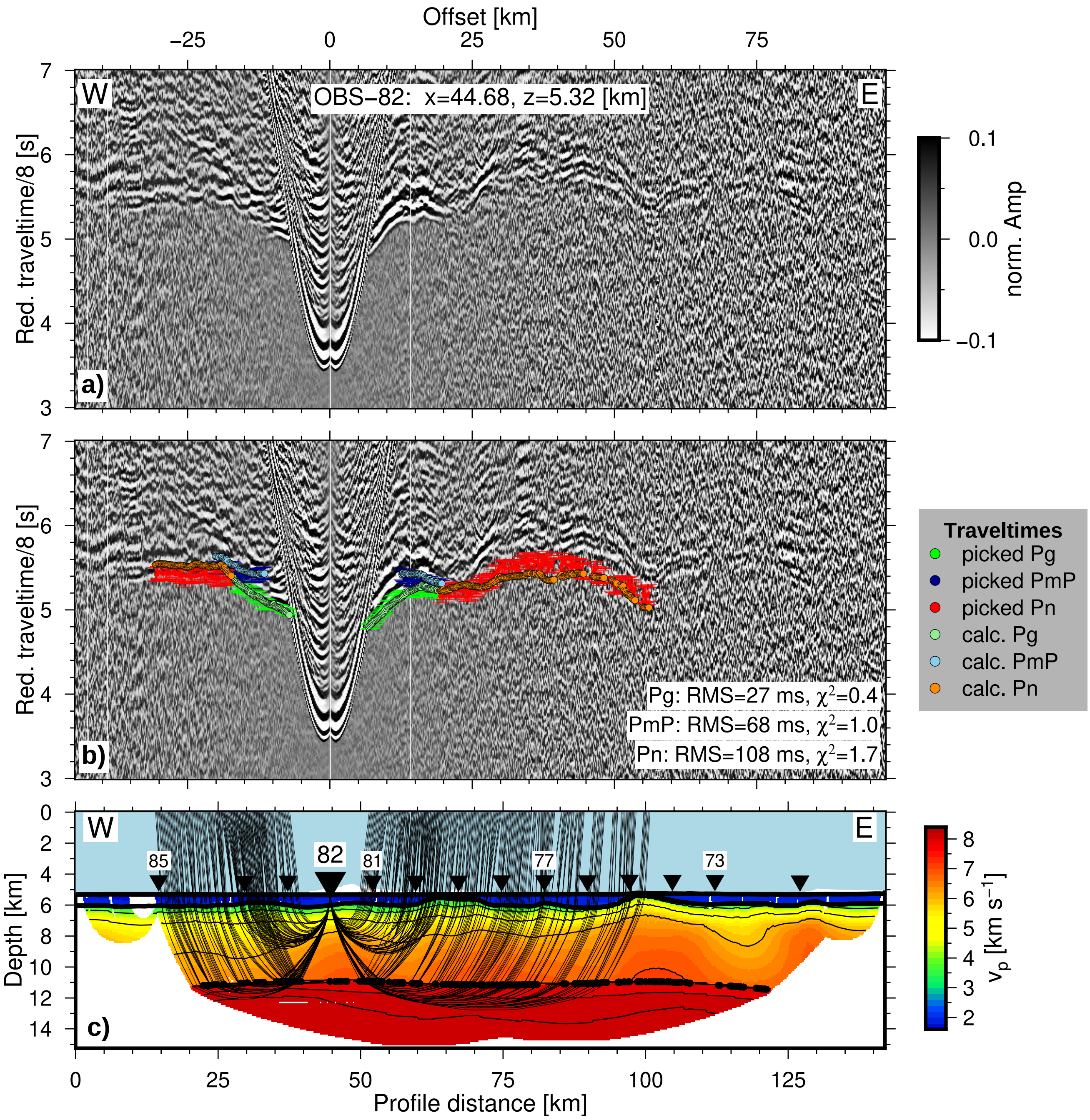

Figure S1k. Record section, traveltime fit and raypaths for OBS 82 (LI-02) .

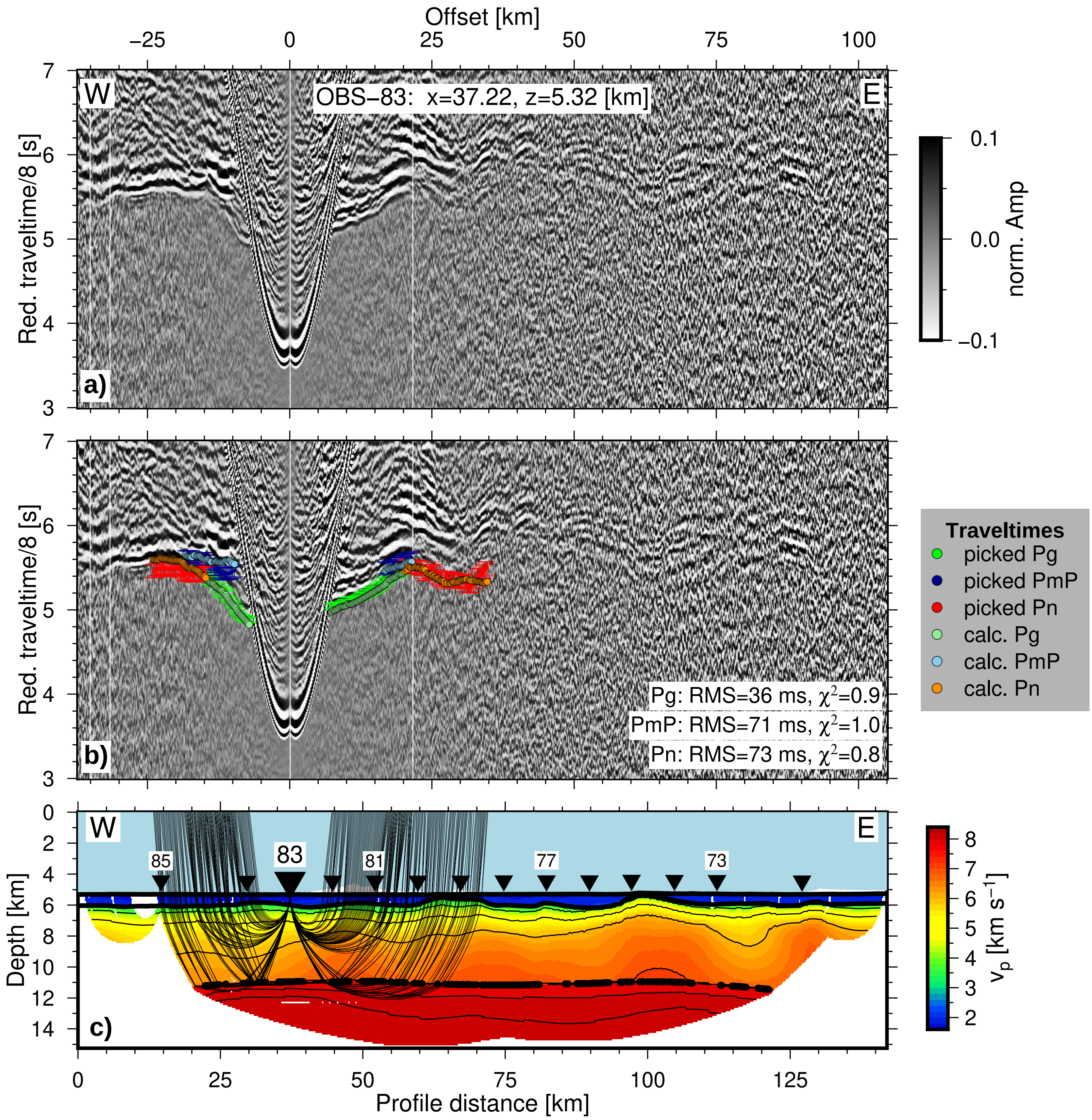

Figure S1l. Record section, traveltime fit and raypaths for OBS 83 (LI-02).

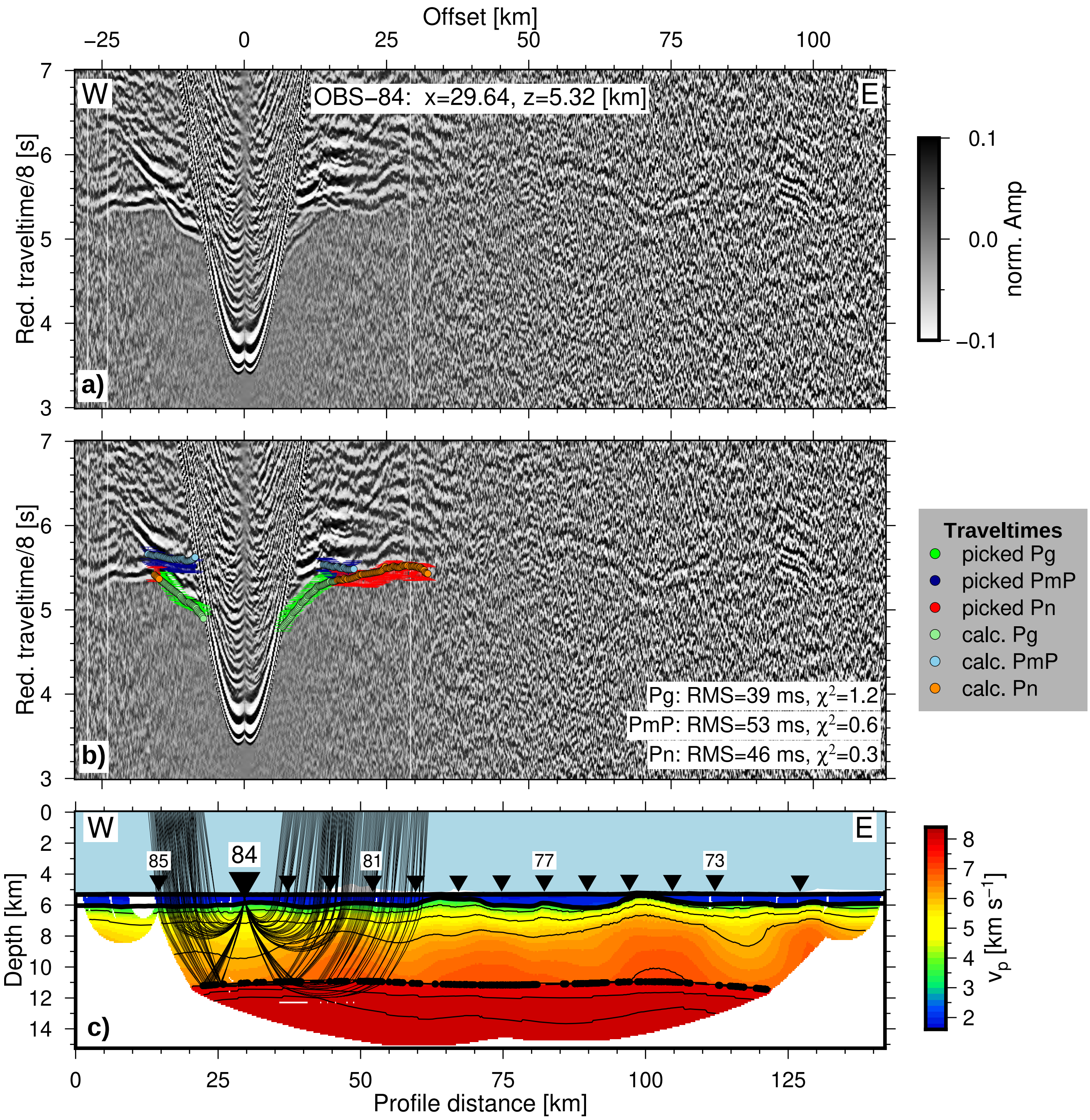

Figure S1m. Record section, traveltime fit and raypaths for OBS 84 (LI-02).

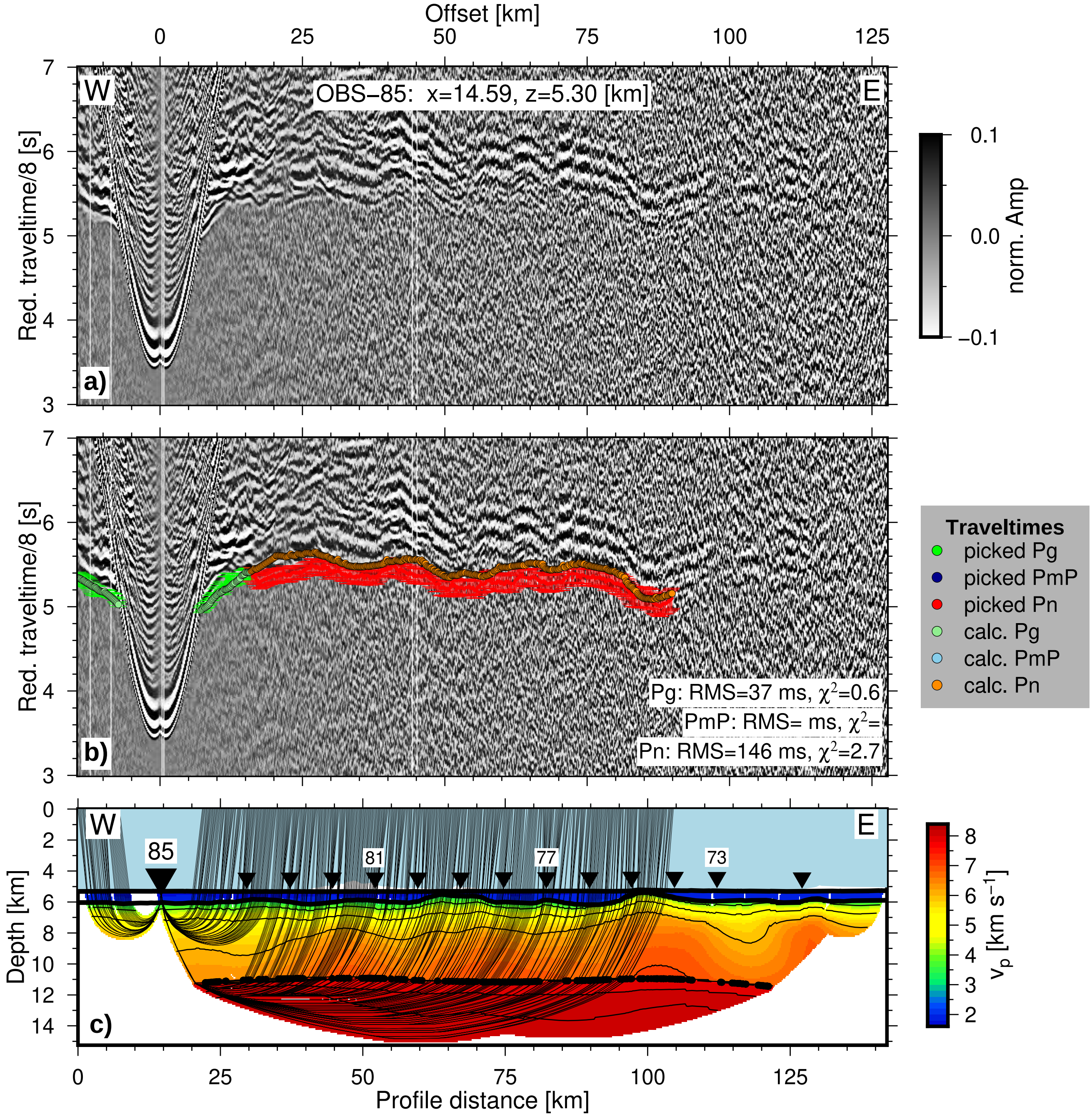

Figure S1n. Record section, traveltime fit and raypaths for OBS 85 (LI-02).

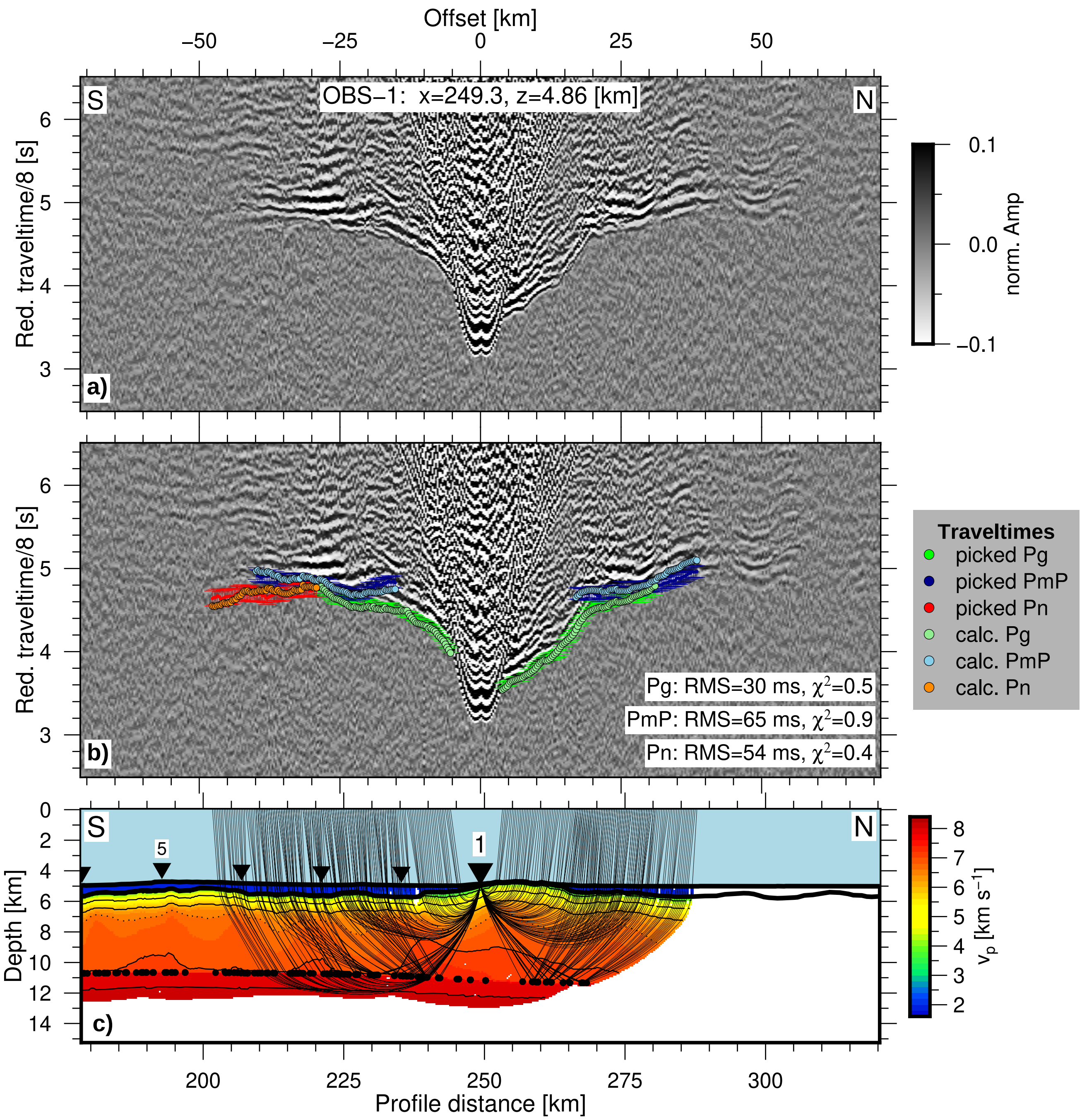

Figure S2a. Record section, traveltime fit and raypaths for OBS 01 (IS-01).

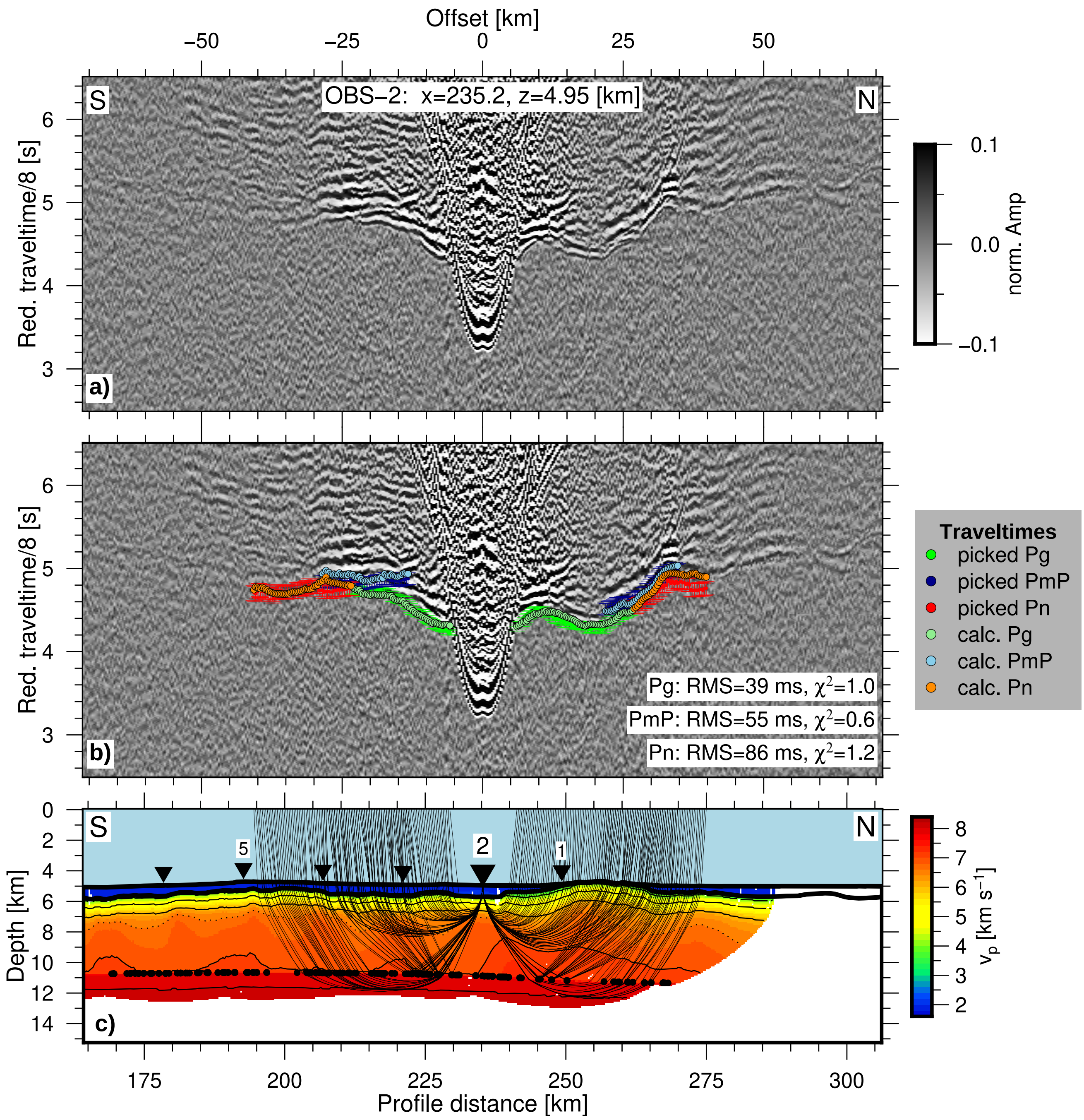

Figure S2b. Record section, traveltime fit and raypaths for OBS 02 (IS-01).

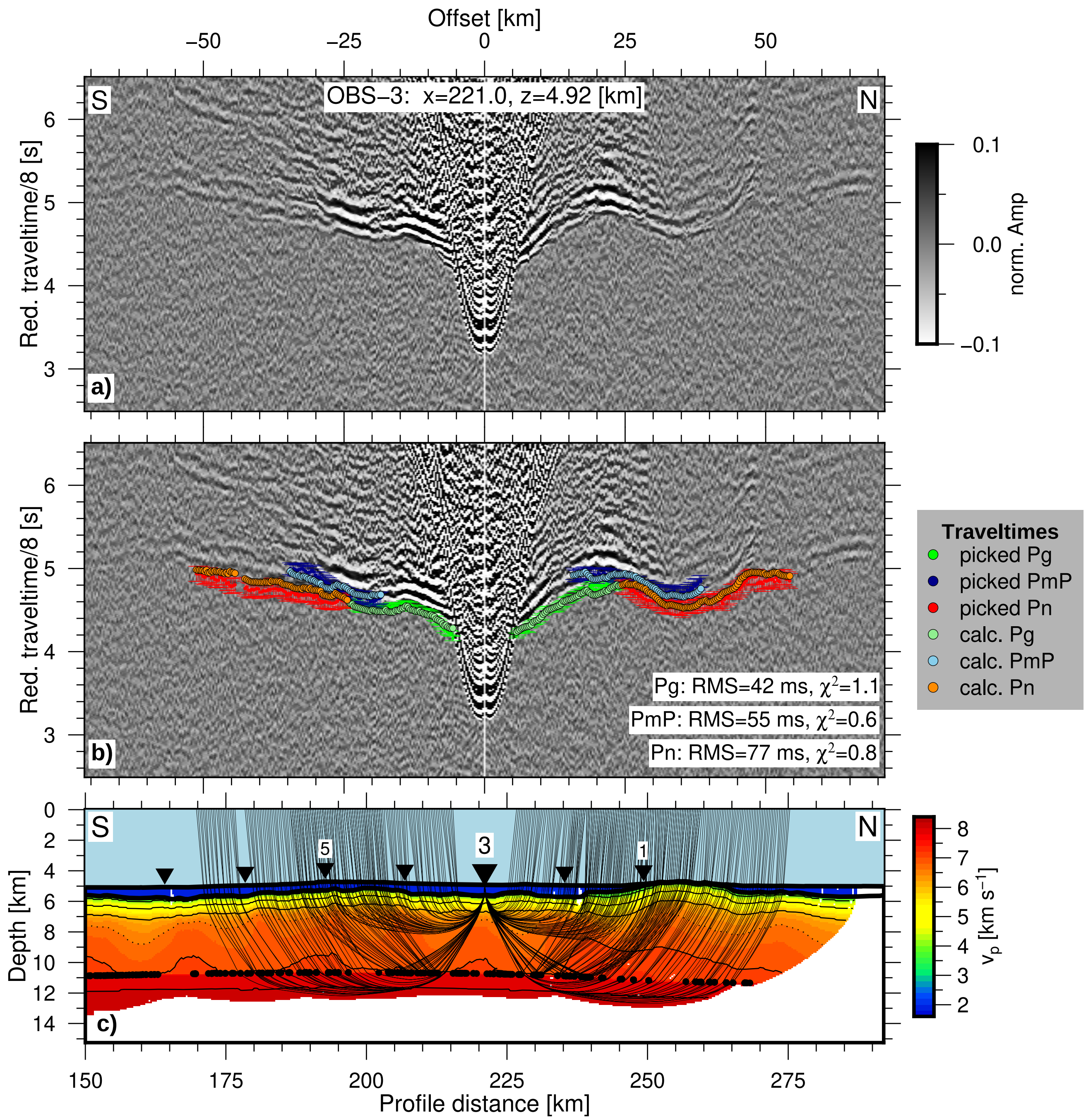

Figure S2c. Record section, traveltime fit and raypaths for OBS 03 (IS-01).

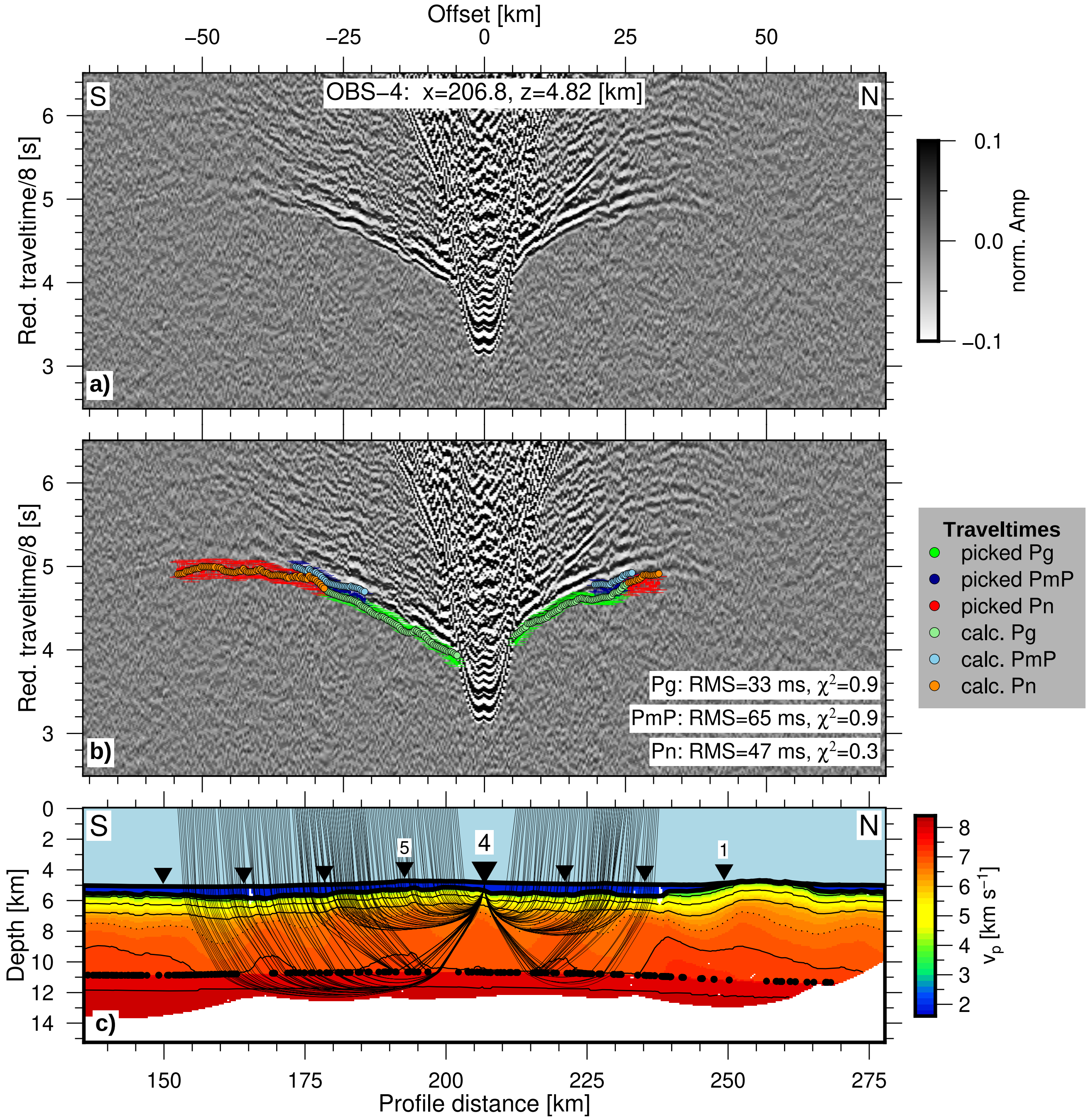

Figure S2d. Record section, traveltime fit and raypaths for OBS 04 (IS-01).

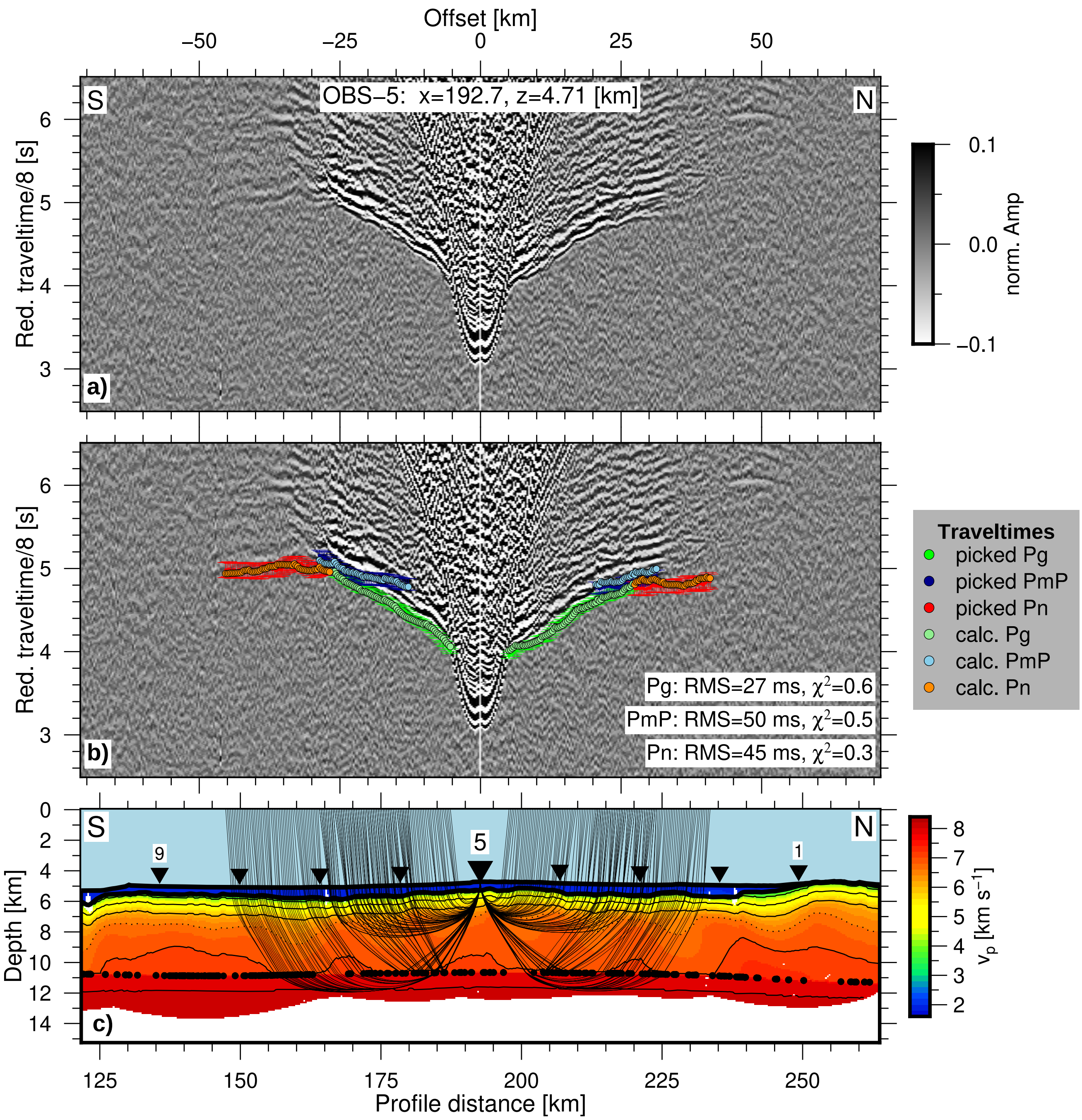

Figure S2e. Record section, traveltime fit and raypaths for OBS 05 (IS-01).

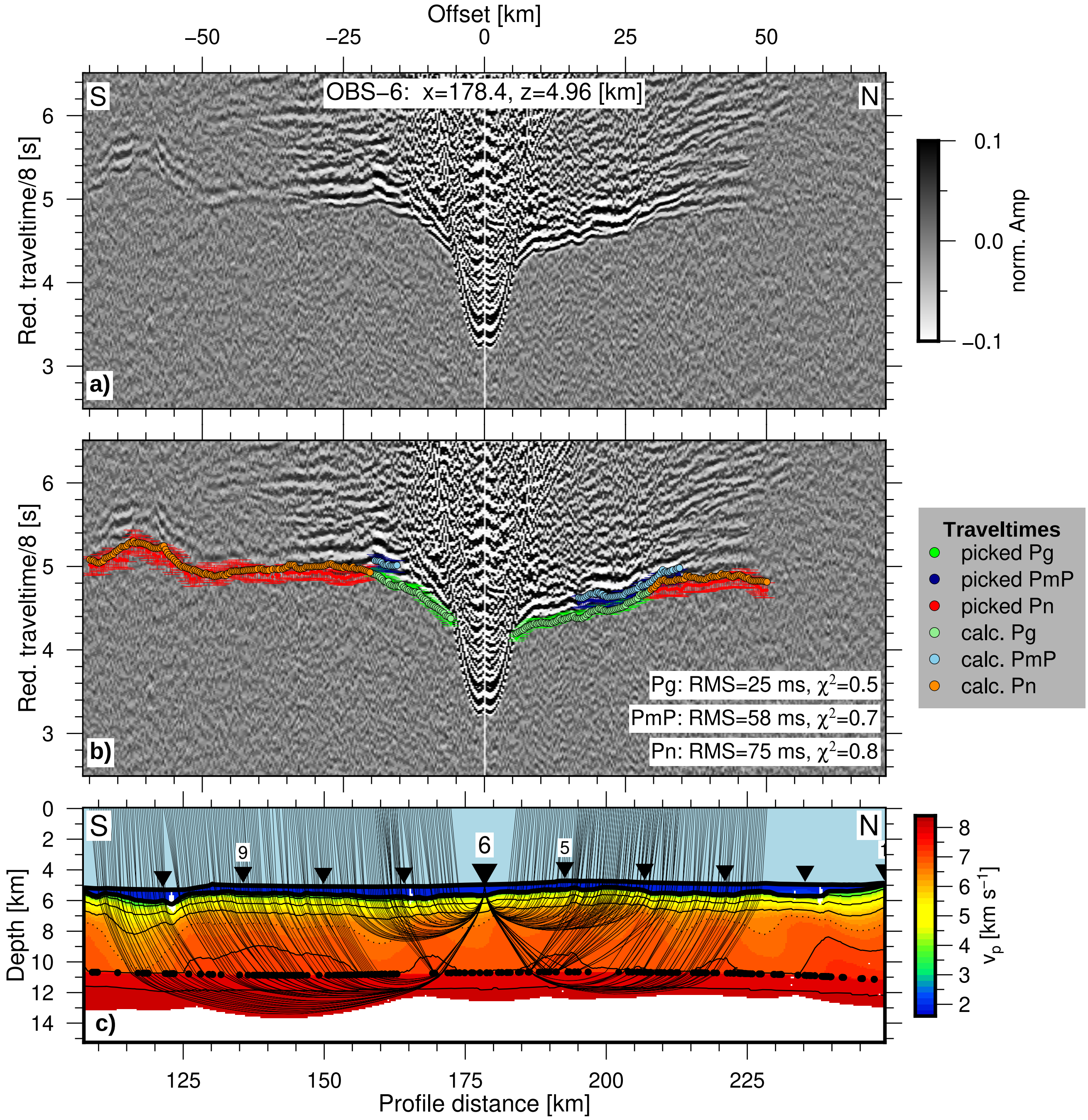

Figure S2f. Record section, traveltime fit and raypaths for OBS 06 (IS-01).

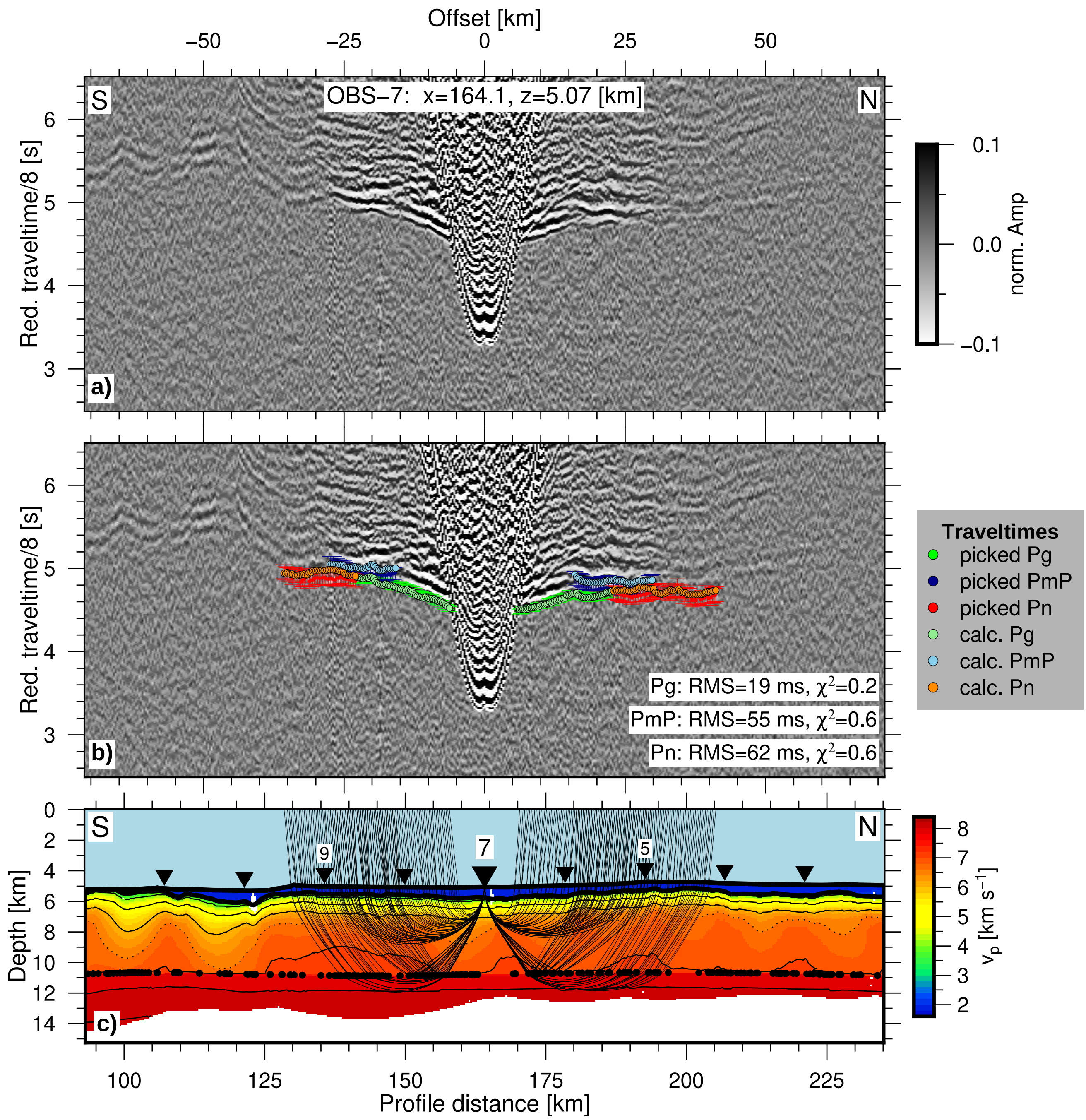

Figure S2g. Record section, traveltime fit and raypaths for OBS 07 (IS-01).

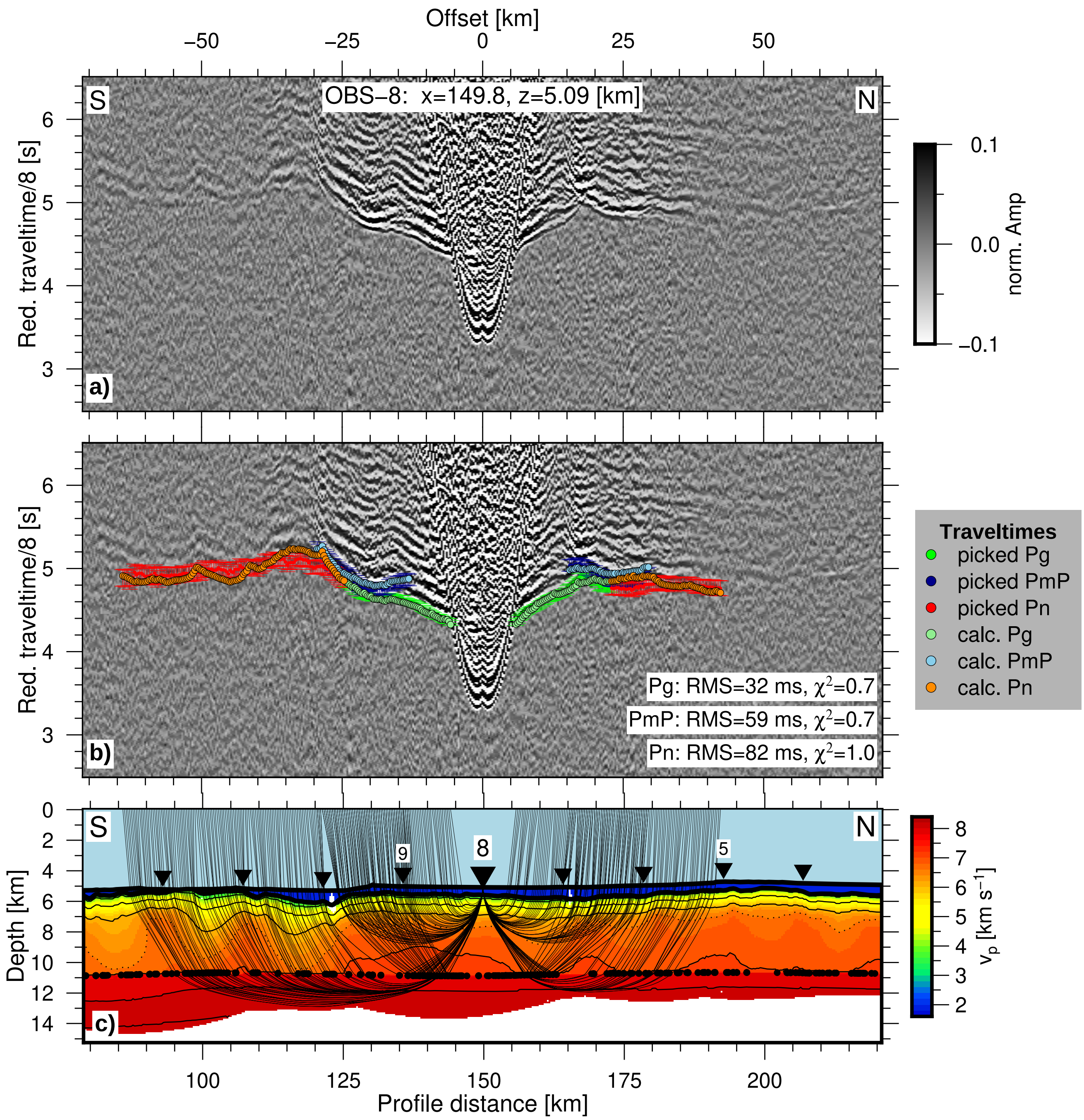

Figure S2h. Record section, traveltime fit and raypaths for OBS 08 (IS-01).

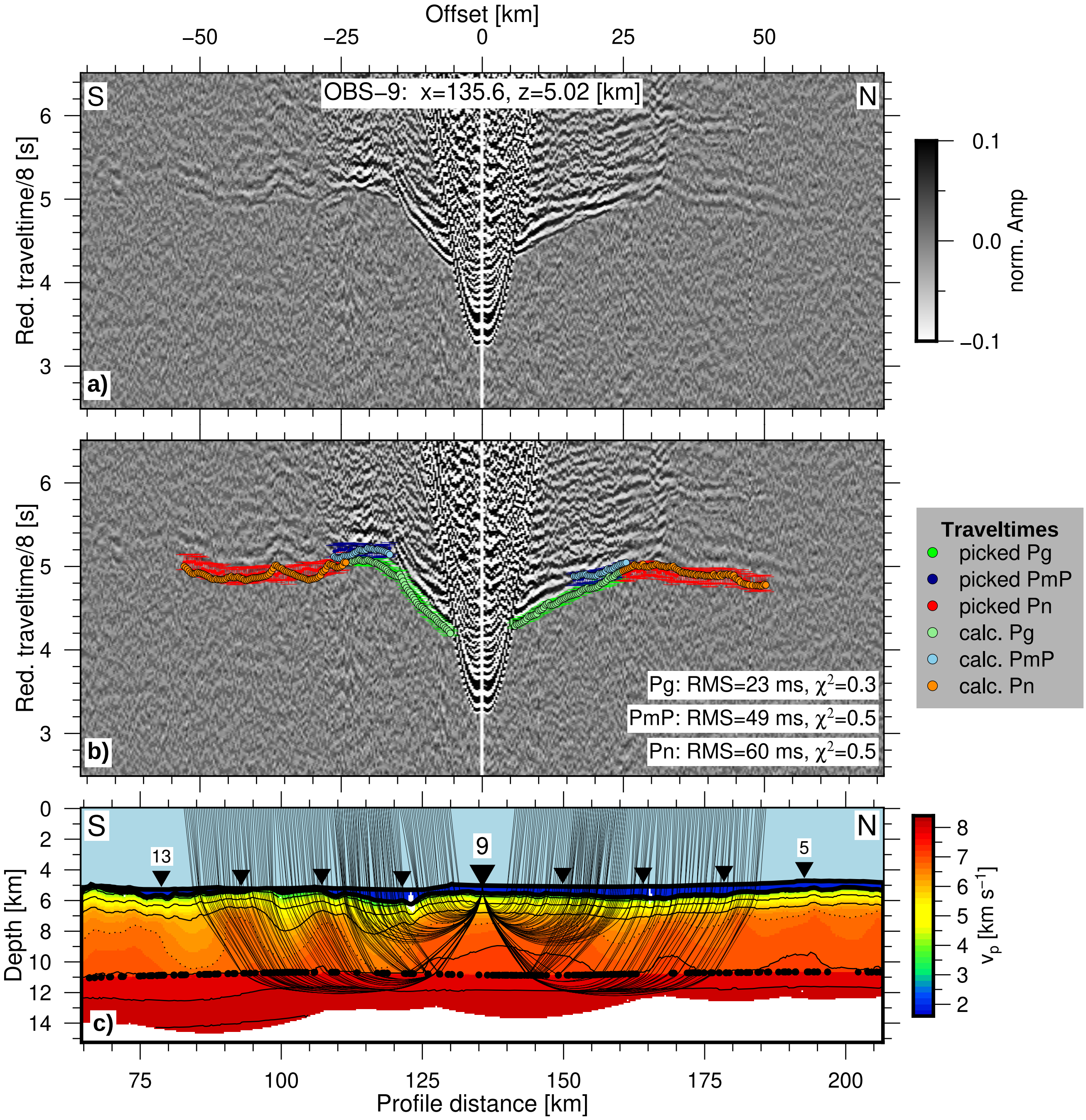

Figure S2i. Record section, traveltime fit and raypaths for OBS 09 (IS-01).

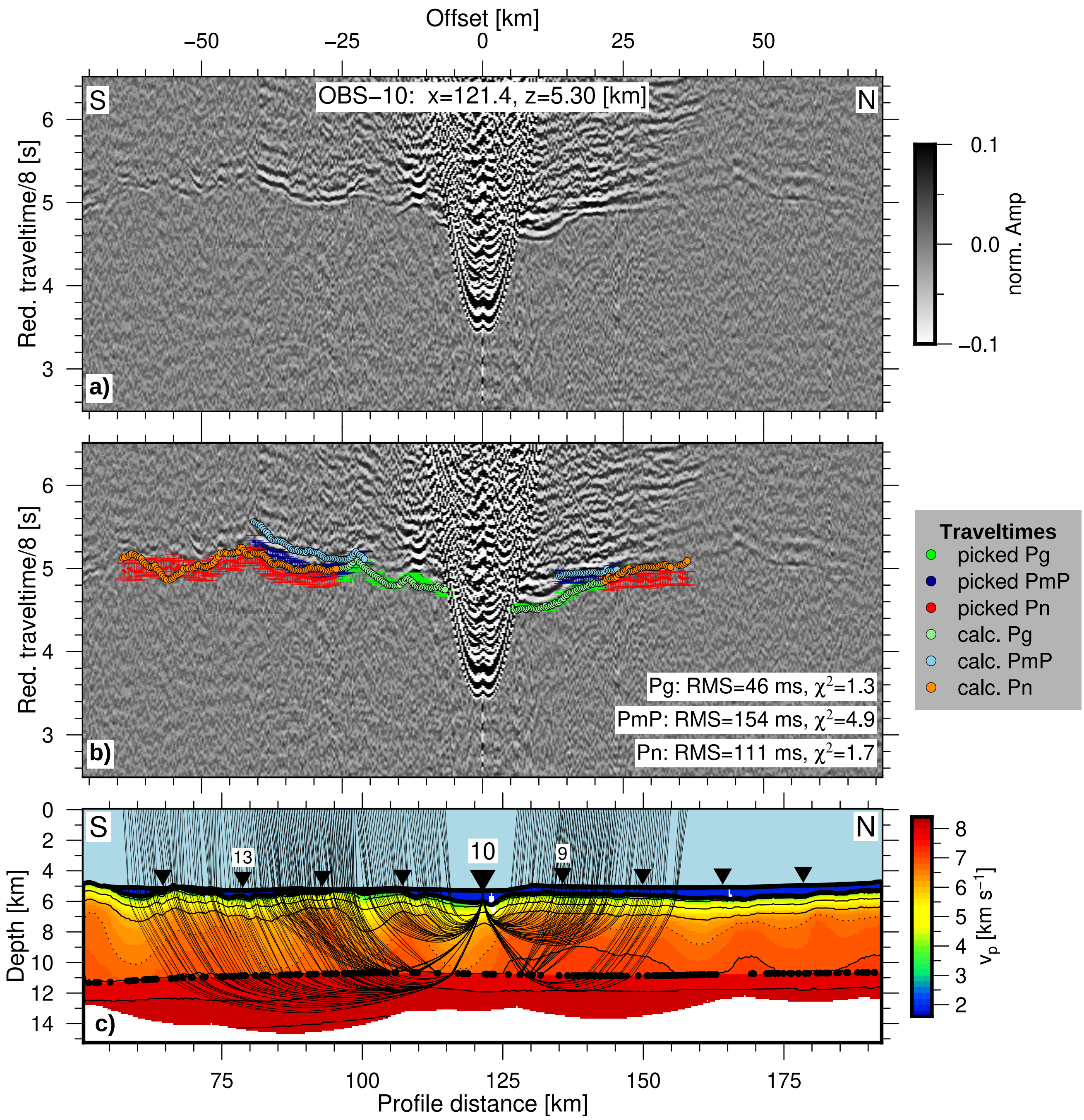

Figure S2j. Record section, traveltime fit and raypaths for OBS 10 (IS-01).

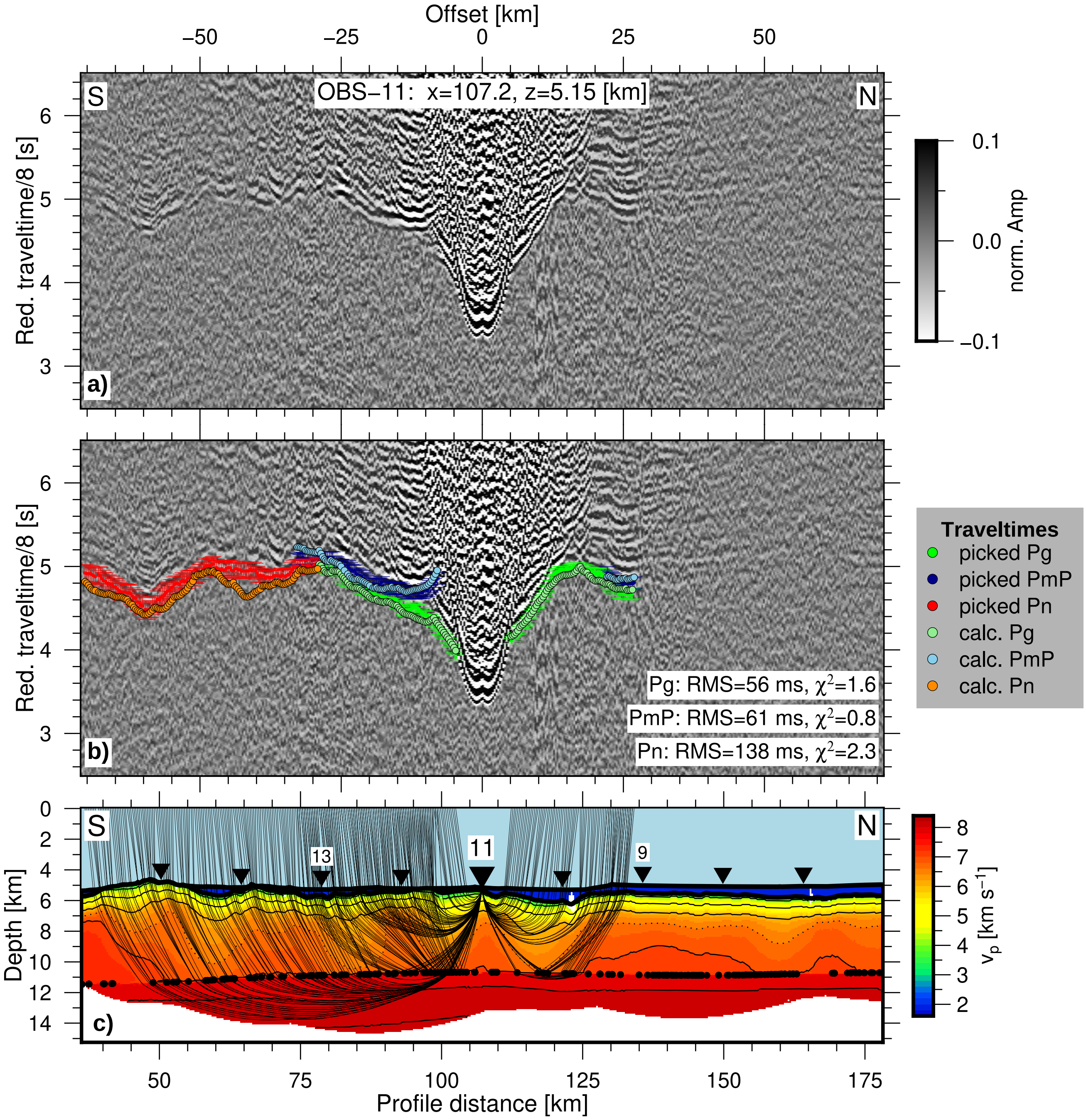

Figure S2k. Record section, traveltime fit and raypaths for OBS 11 (IS-01).

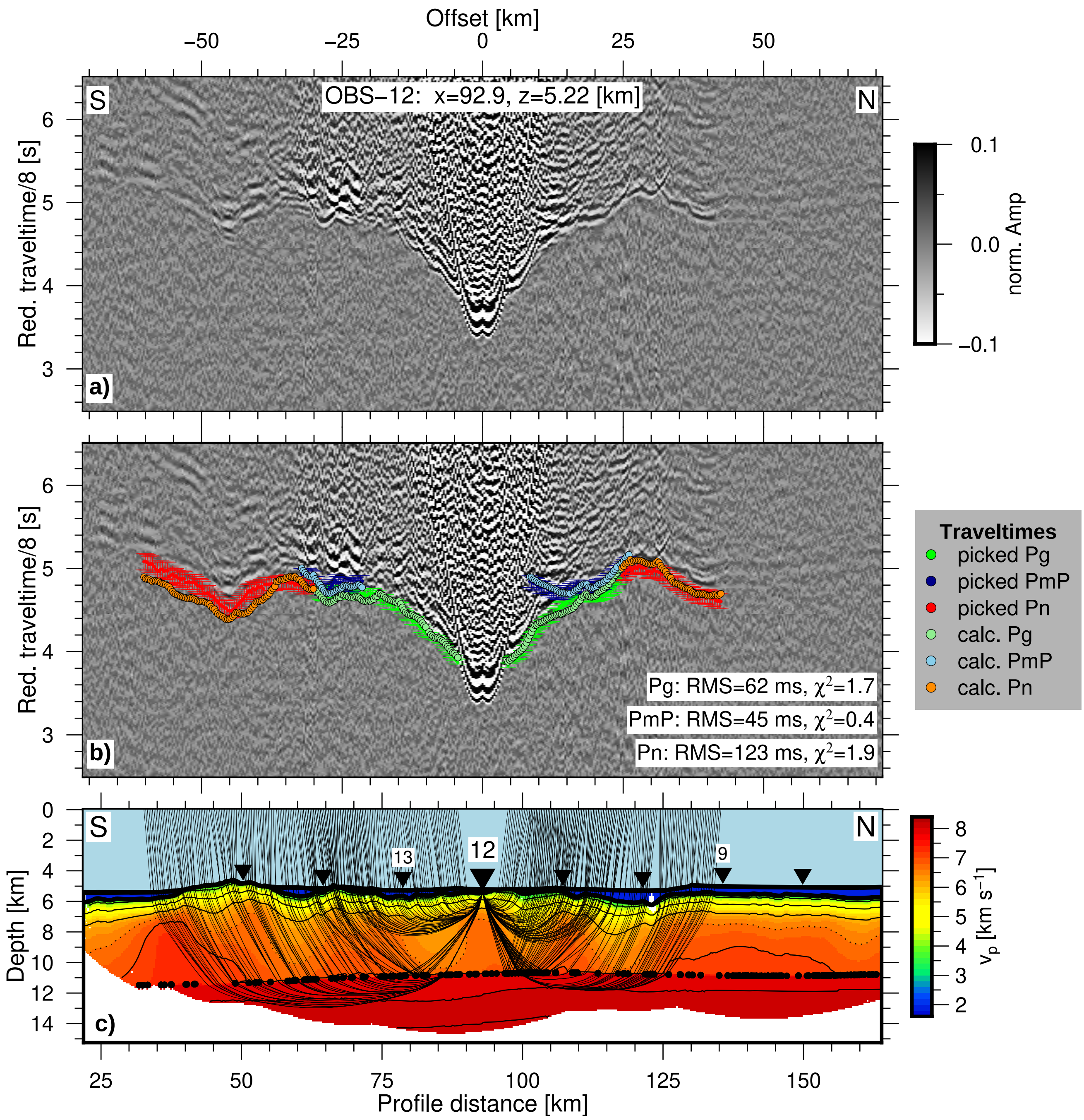

Figure S2l. Record section, traveltime fit and raypaths for OBS 12 (IS-01).

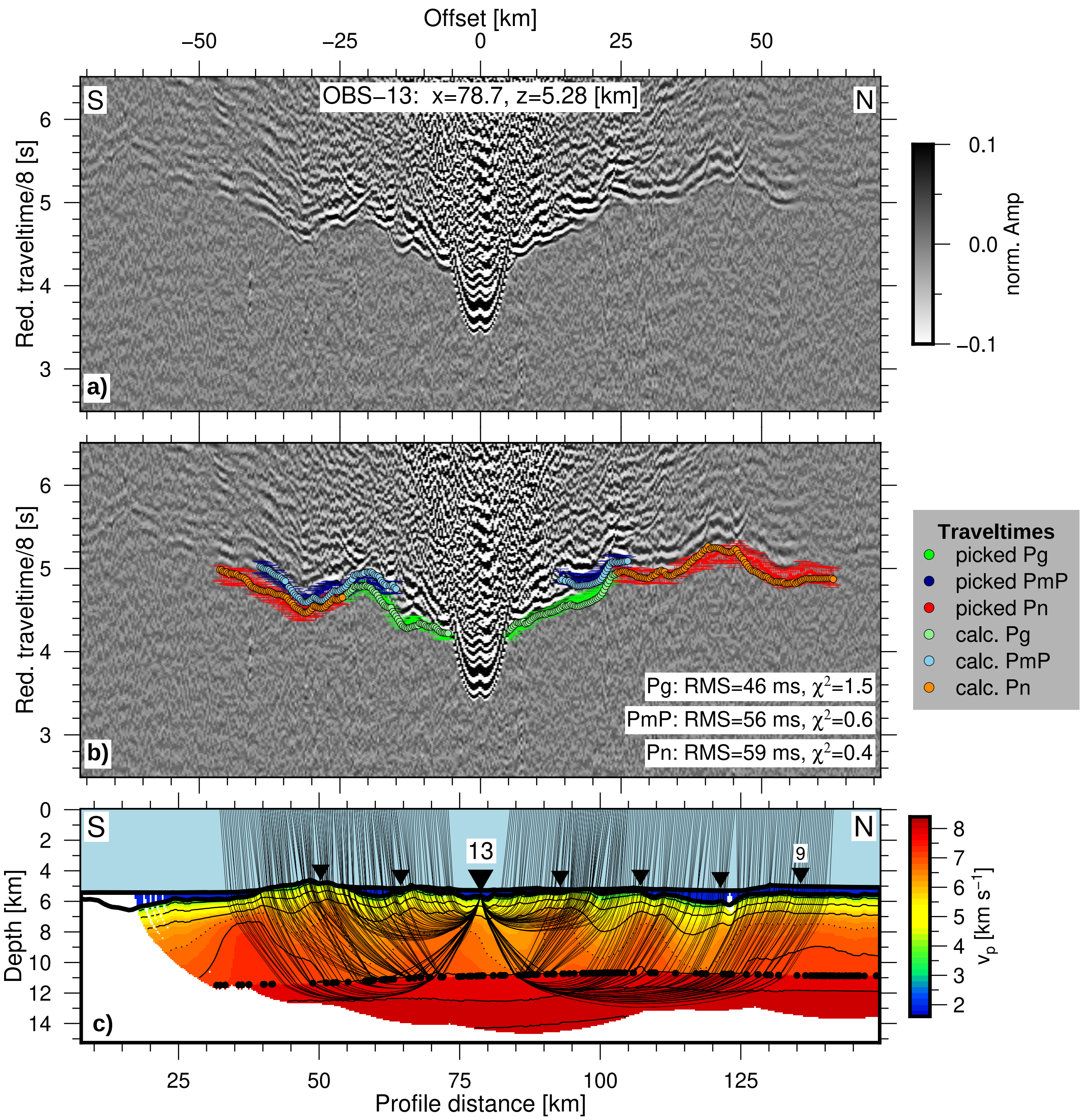

Figure S2m. Record section, traveltime fit and raypaths for OBS 13 (IS-01).

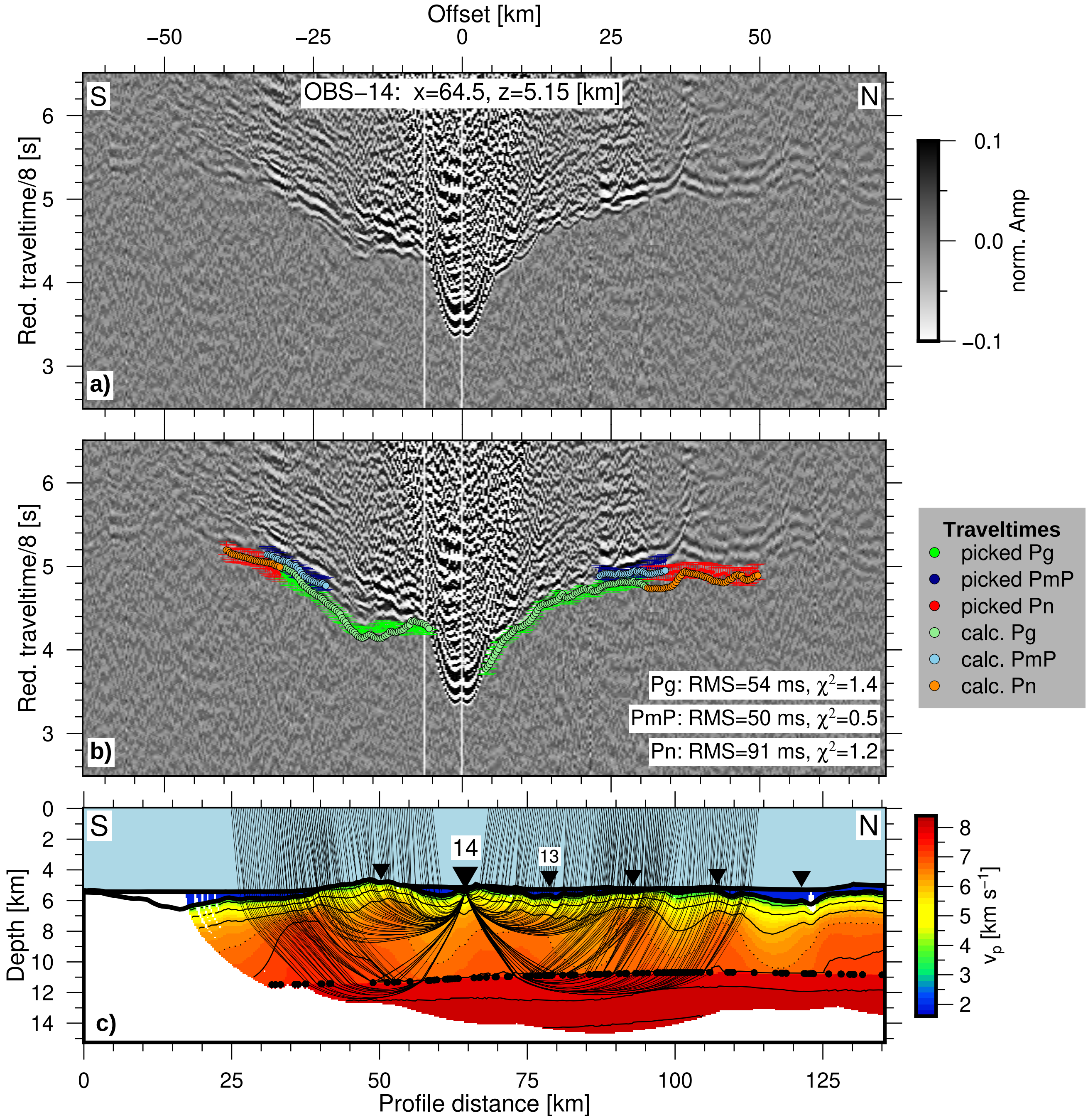

Figure S2n. Record section, traveltime fit and raypaths for OBS 14 (IS-01).

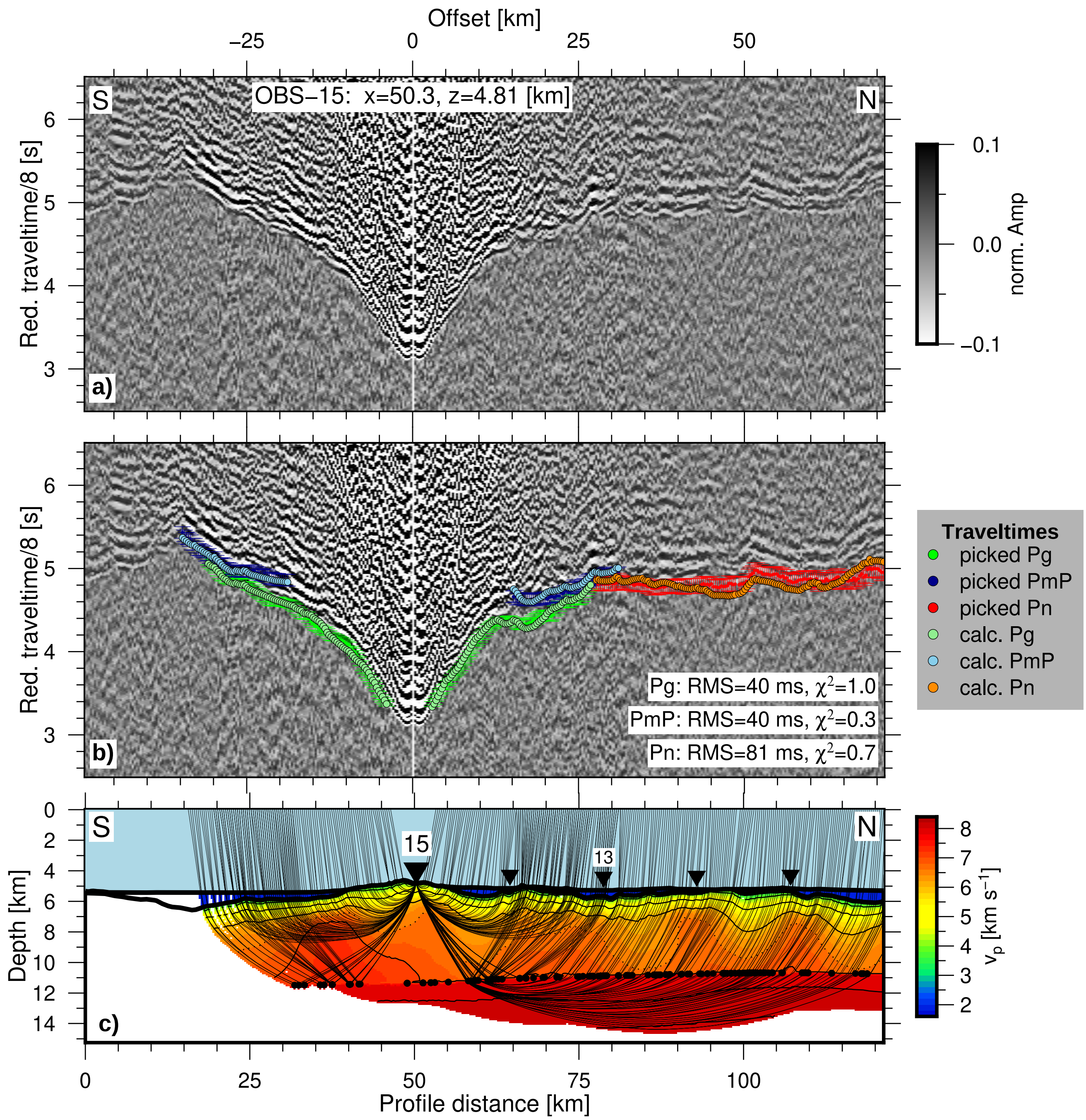

Figure S2o. Record section, traveltime fit and raypaths for OBS 15 (IS-01).

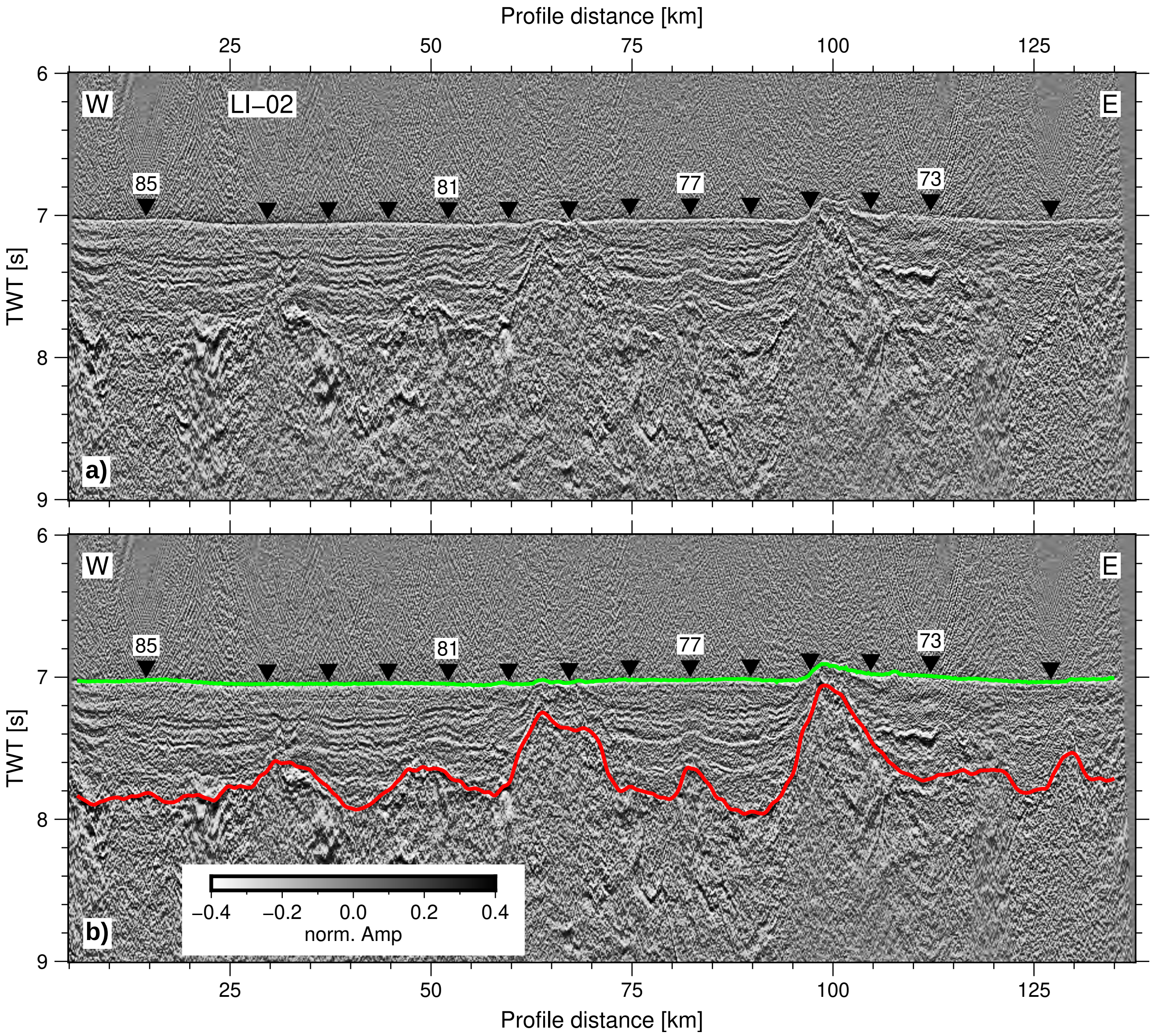

Figure S3. LI-02: **(a)** Mirror image obtained by migration of the multiples (e.g Grion et al., 2007) with **(b)** superimposed seafloor (green) and basement (red) picks. The amplitude is normalized by its maximum and clipped to 40 %.

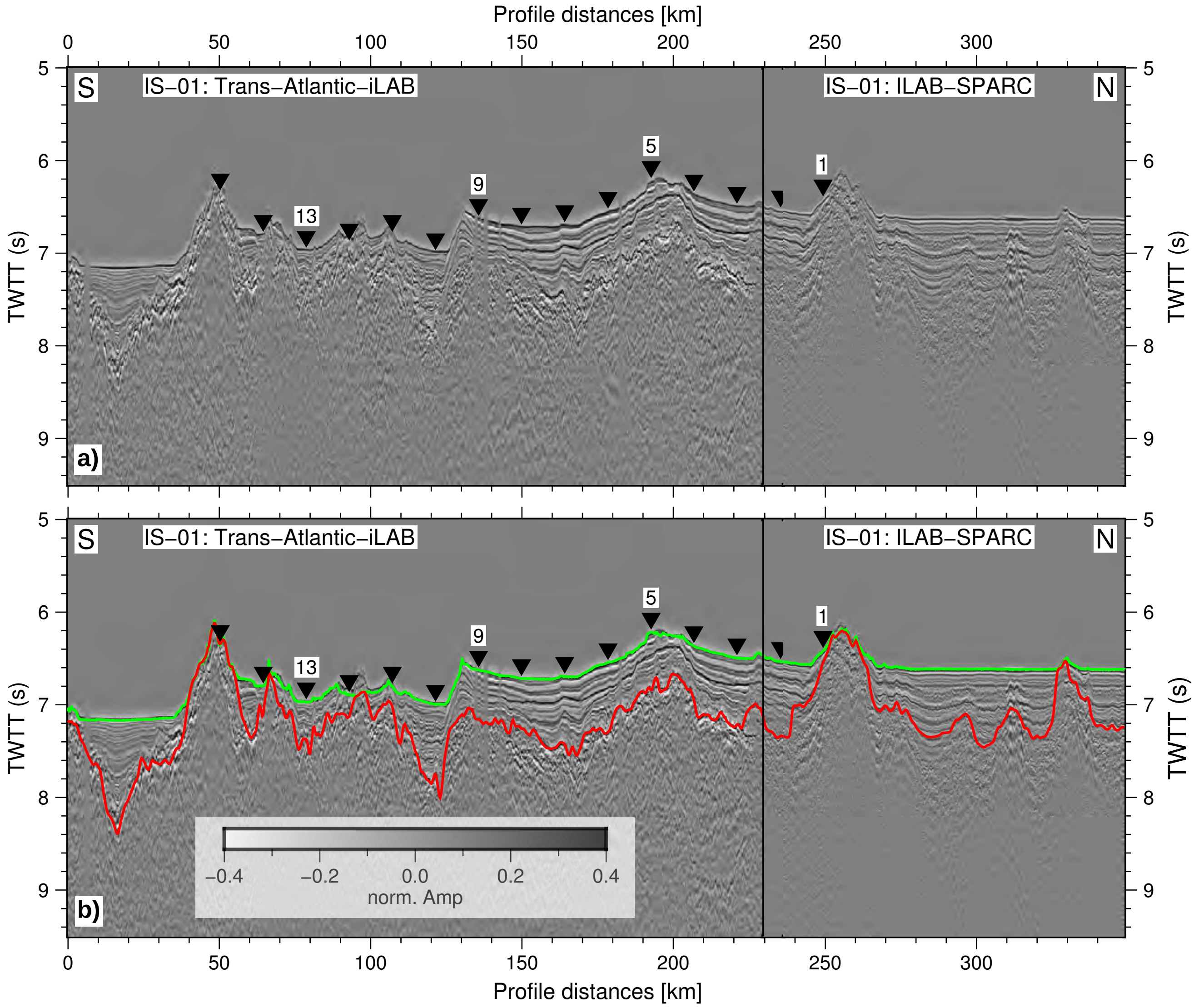

Figure S4. IS-01: **(a)** A composite post-stack time-migrated MCS section along the N-S line acquired during the two cruises, Trans-Atlantic-iLAB (2015) and ILAB-SPARC (2018). The solid vertical line indicates the joint location for the two datasets. The information on the MCS data processing steps is provided in the main text. The amplitude is normalized by its maximum and clipped to 40 %. **(b)** Seafloor (green) and basement (red) picks are superimposed on the seismic section.

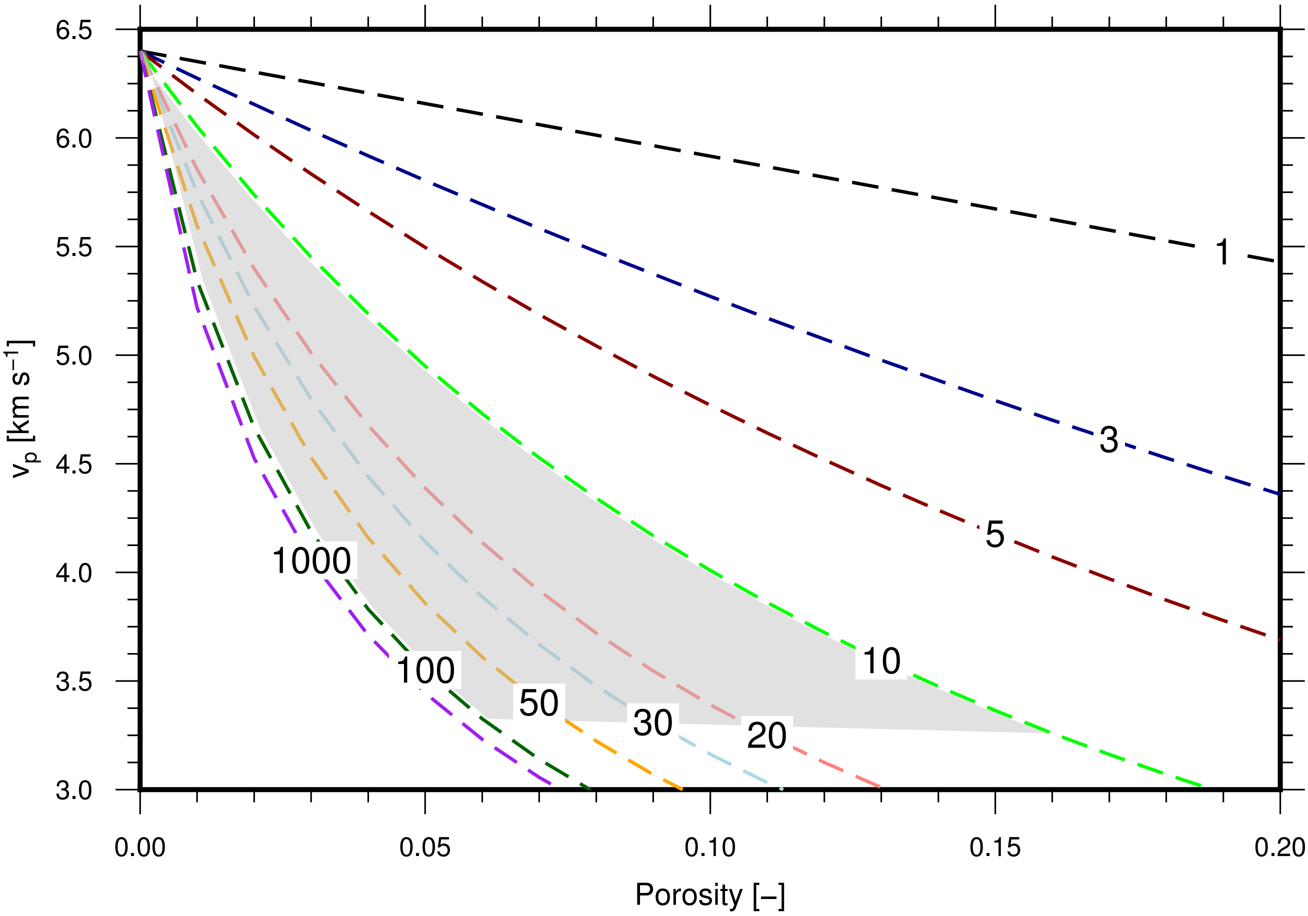

Figure S5. Velocity-porosity relationship for different aspect ratios of fractures (numbered labels). Calculated using a differential effective medium analysis after Taylor and Singh (2002) for a basaltic host rock. Grey area highlights the range of observed crustal velocities and hence the range of possible porosities with respect to the chosen range of aspect ratios of 10-100.

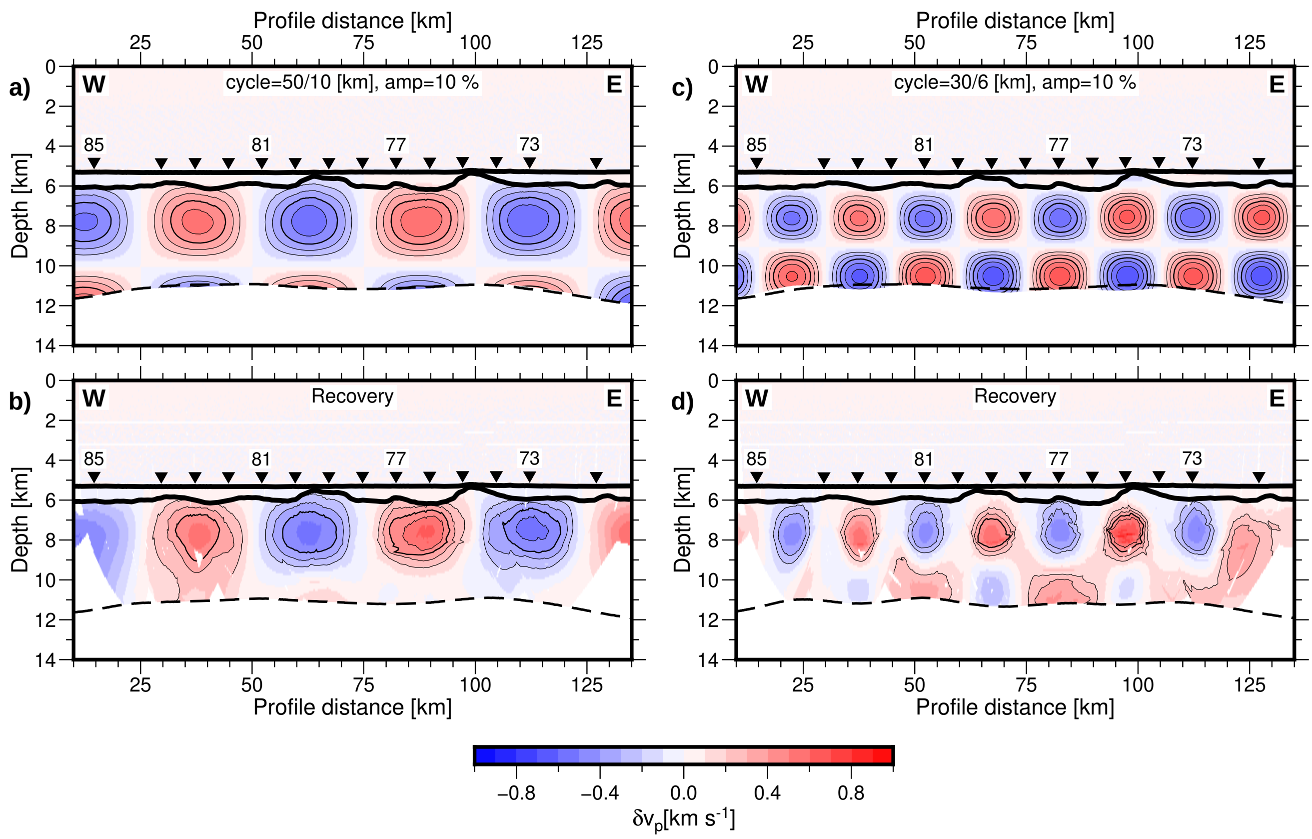

Figure S6. Checkerboard test for LI-02: crustal checkerboard resolution test for different cycle lengths and a perturbation amplitude of 10 %. The contour interval is 0.1 km/s starting at ±0.2 km/s. The dashed line denotes the constrained Moho reflector. The remaining figure elements are the same as in Figure 5 in the main text.

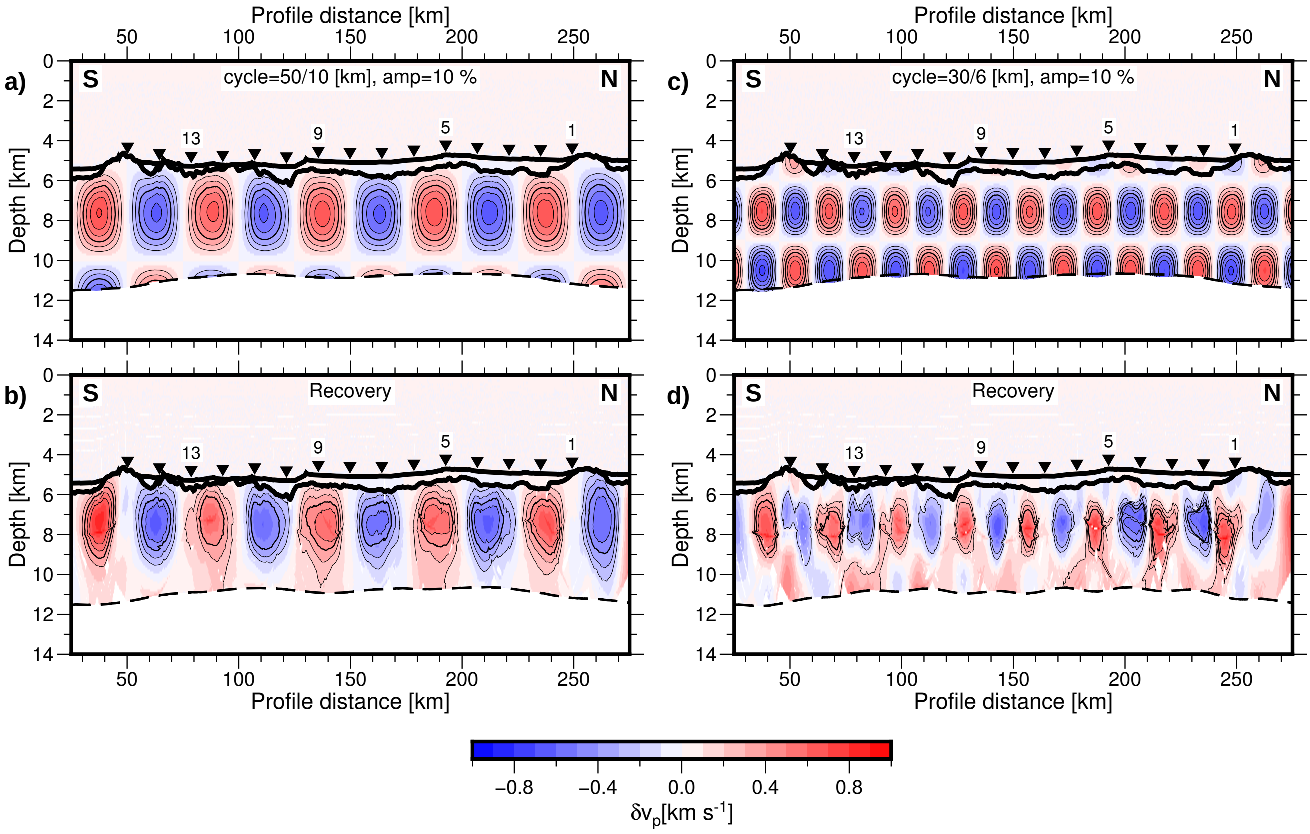

Figure S7. Checkerboard test for IS-01: checkerboard resolution test as in Fig. S6.

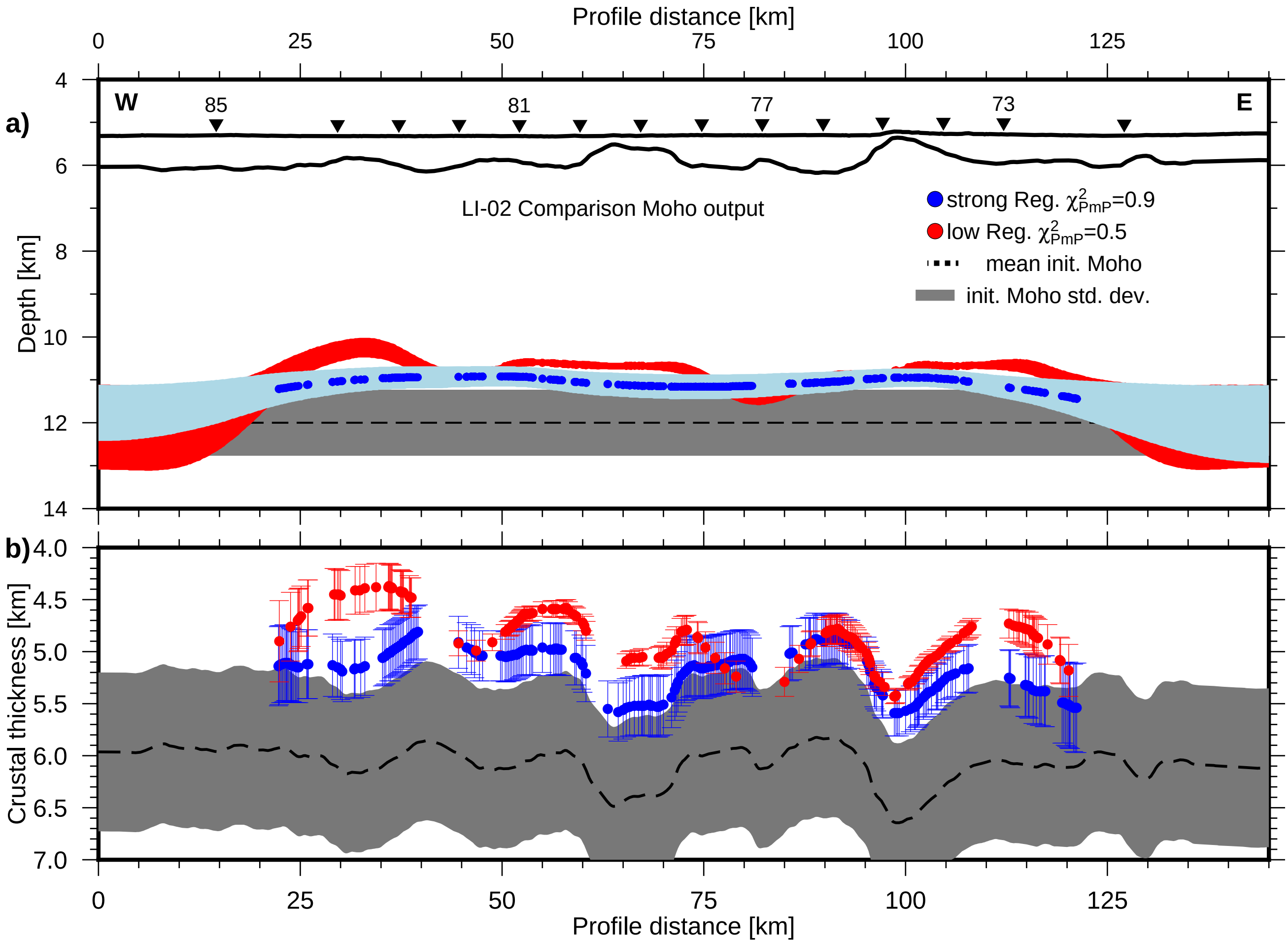

Figure S8. LI-02: **(a)** Comparison of Moho results for line LI-02 from the MCAs using 'strong' (blue) and weak regularization (see Table S3). Dots and shaded areas denote the mean obtained reflection points and the Moho standard deviation from the MCA. Dashed line and gray shading denote the mean initial Moho and the input standard deviation. Solid black lines denote the seafloor and the basement. The inverted black triangles denote the OBS locations. Every fourth OBS is labeled. **(b)** Corresponding crustal thickness along the line. The dots and the error bars represent the modelled PmP reflection points and their standard deviation.

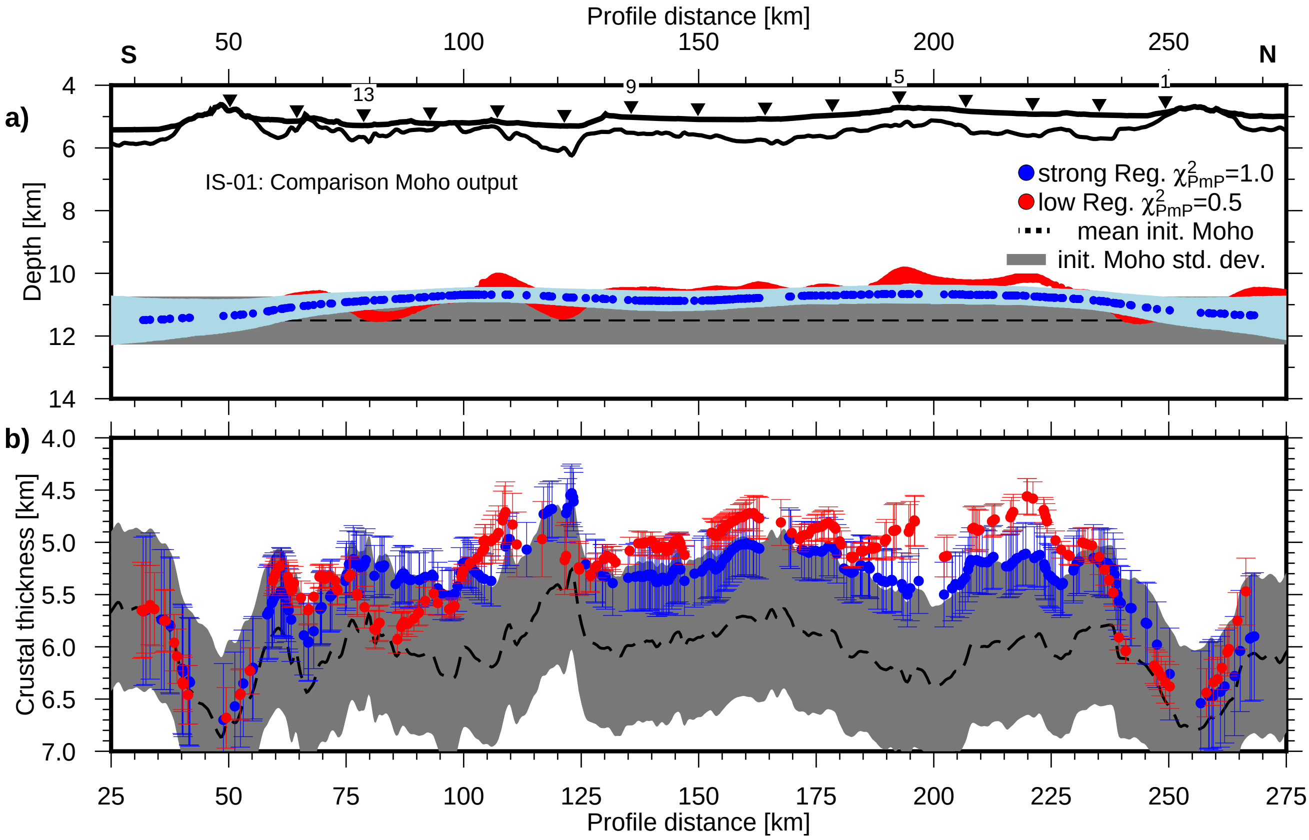

Figure S9. IS-01: the same comparison as in Fig. S8 but for line IS-01.

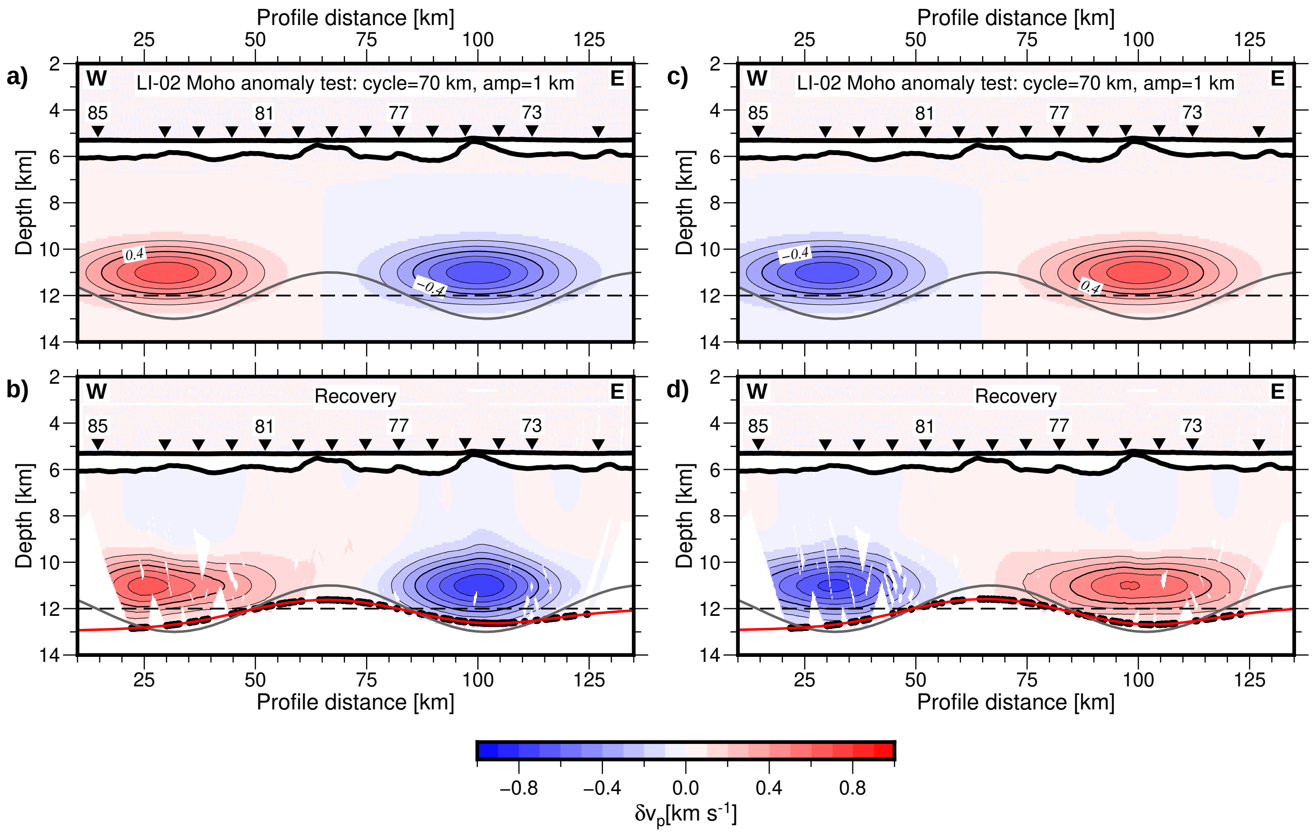

Figure S10. LI-02: Resolution test for sinusoidal Moho anomaly with a cycle of 70 km and a perturbation amplitude of 1 km. Additionally, we introduced gaussian velocity anomalies with horizontal radius of 20 km, a vertical radius of 1.25 km and a perturbation amplitude of 10 % above the Moho reflector. Panels (c,d) show the same test with reversed polarity of (a,b). The contour interval is 0.1 km/s starting at 0.2 km/s. The horizontal dashed, the grey and red lines and the black dots denote the mean input reflector, the perturbed input reflector and the recovered reflector with its obtained reflection points, respectively.

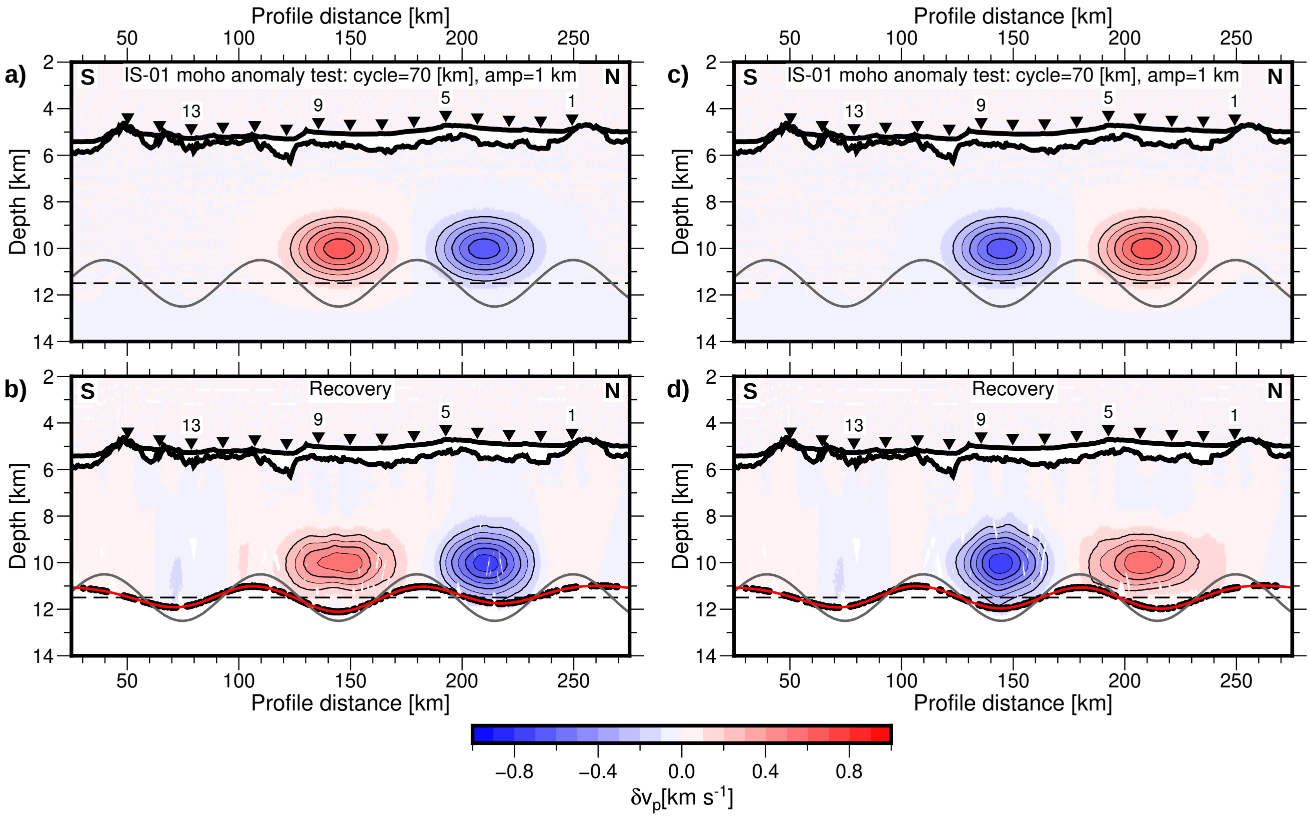

Figure S11. Moho resolution test for IS-01: the same test procedure and figure elements as in Figure S10.

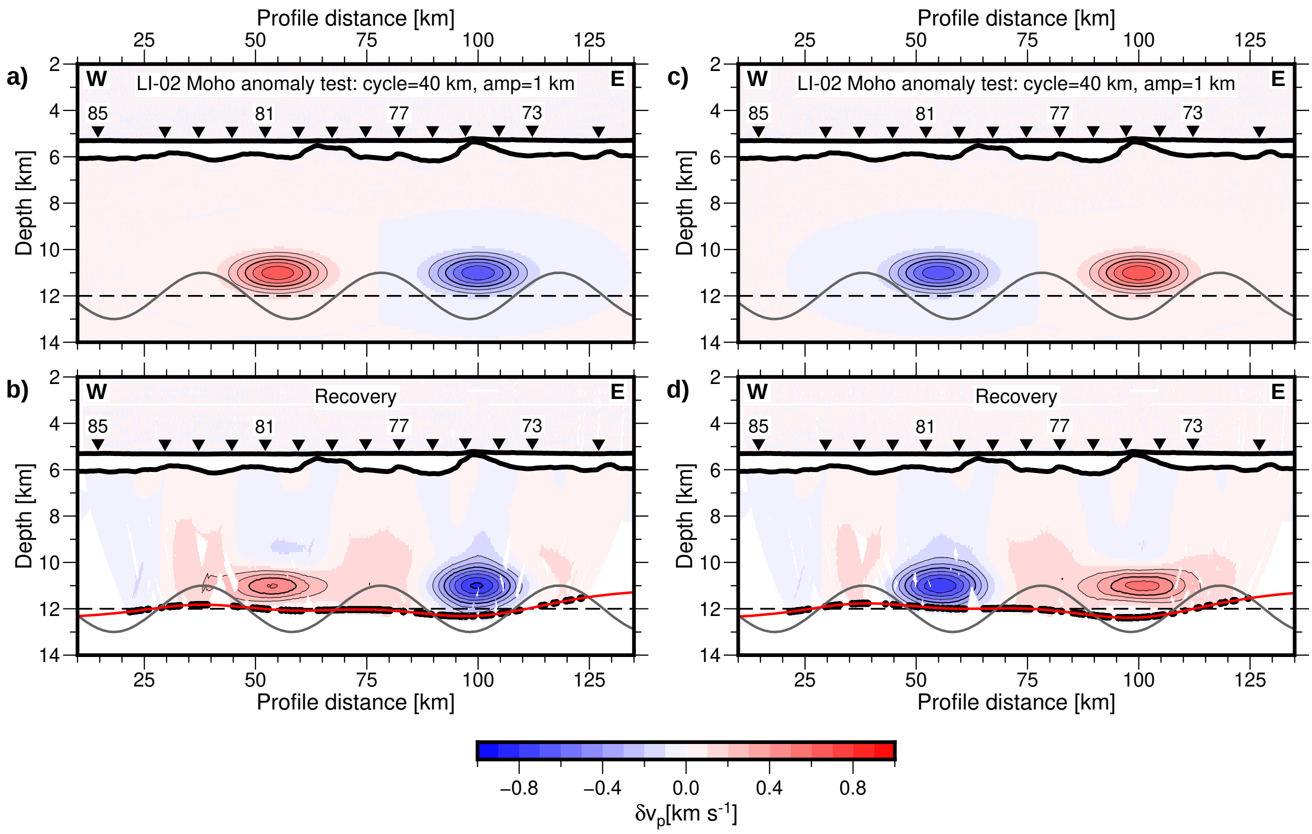

Figure S12. Moho resolution test for LI-02: the same test as in Fig. S10 but with a reduced reflector perturbation cycle length of 40 km.

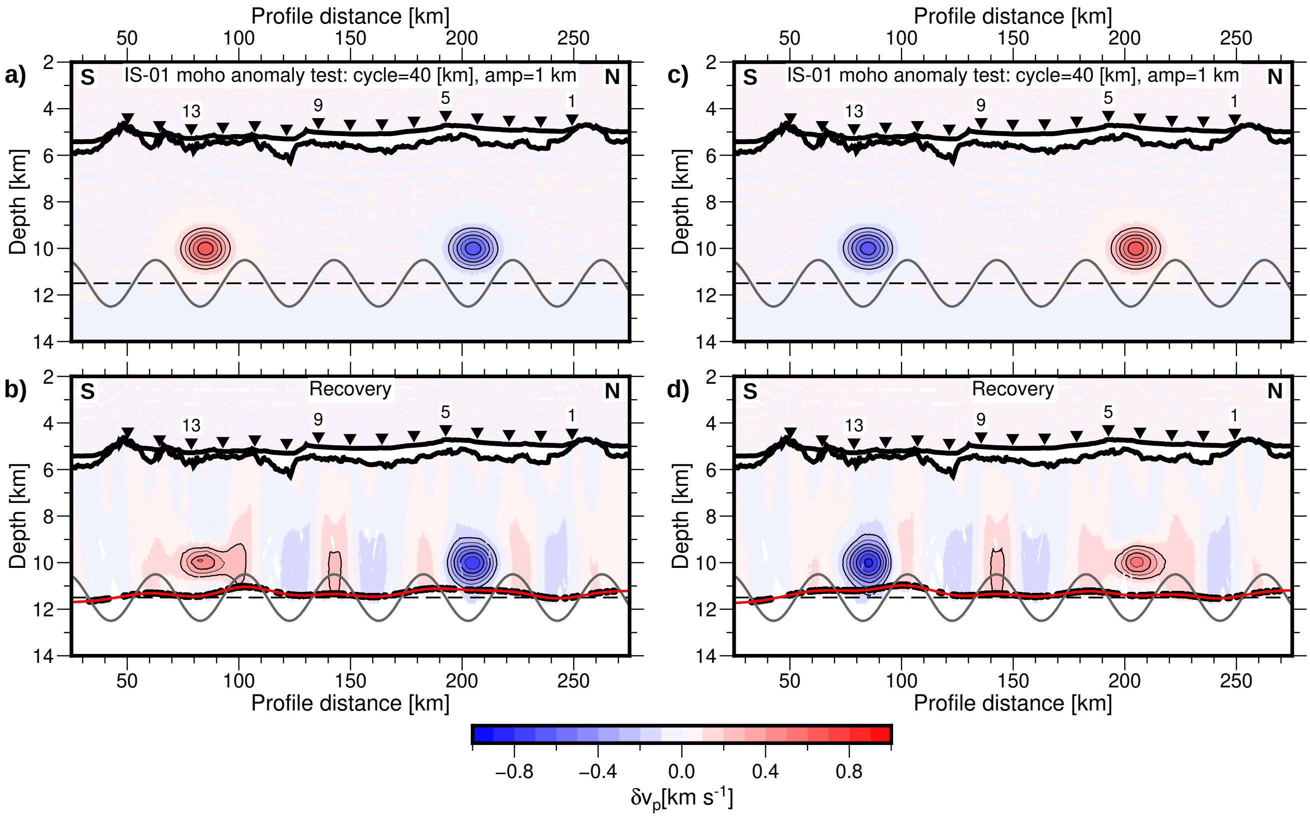

Figure S13. Moho resolution test for IS-01: the same test as in Fig. S11 but with a reduced reflector perturbation cycle length of 40 km.

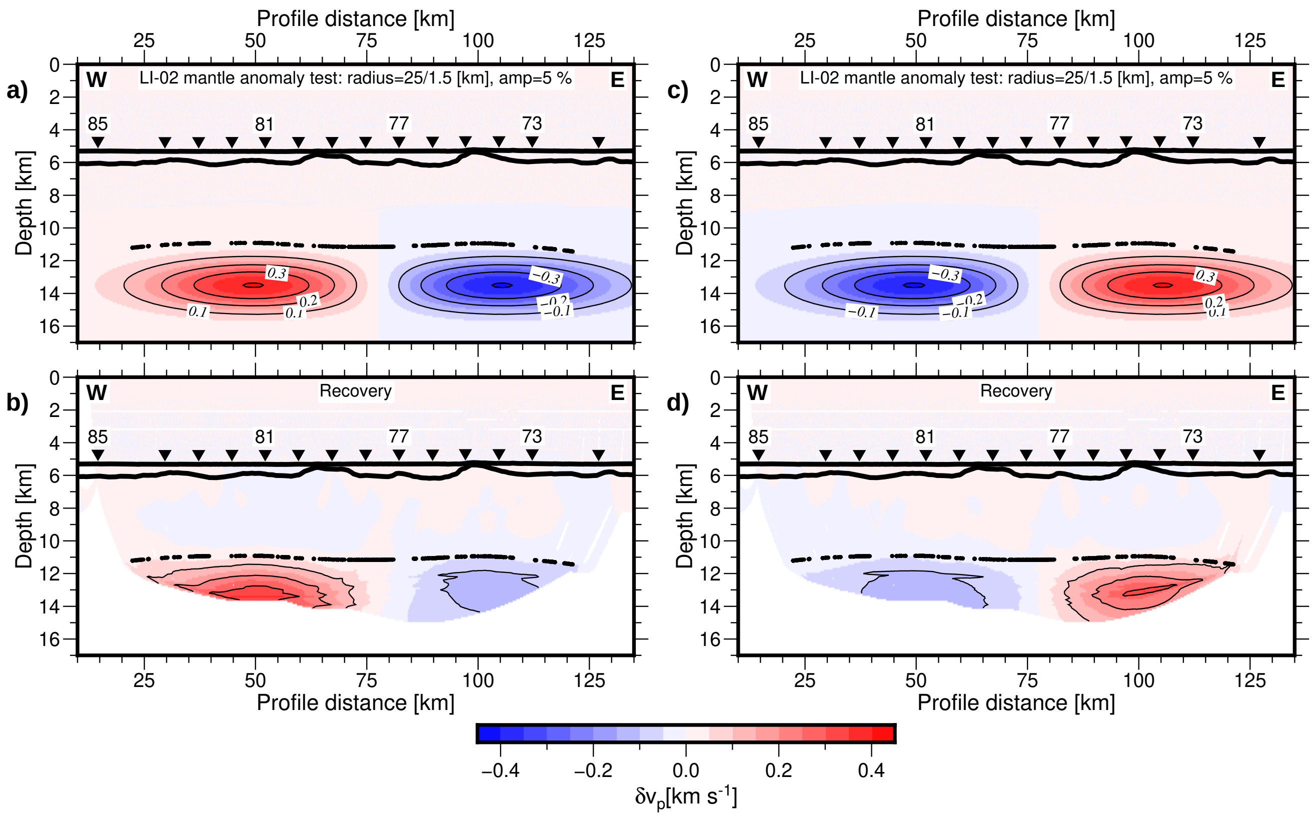

Figure S14. LI-02: mantle anomaly test for gaussian anomaly pattern with horizontal radius of 25 km, a vertical radius of 1.5 km and a perturbation amplitude of 5 %. Panels (c,d) show the same test with reversed polarity of (a,b) The contour interval is 0.1 km/s.

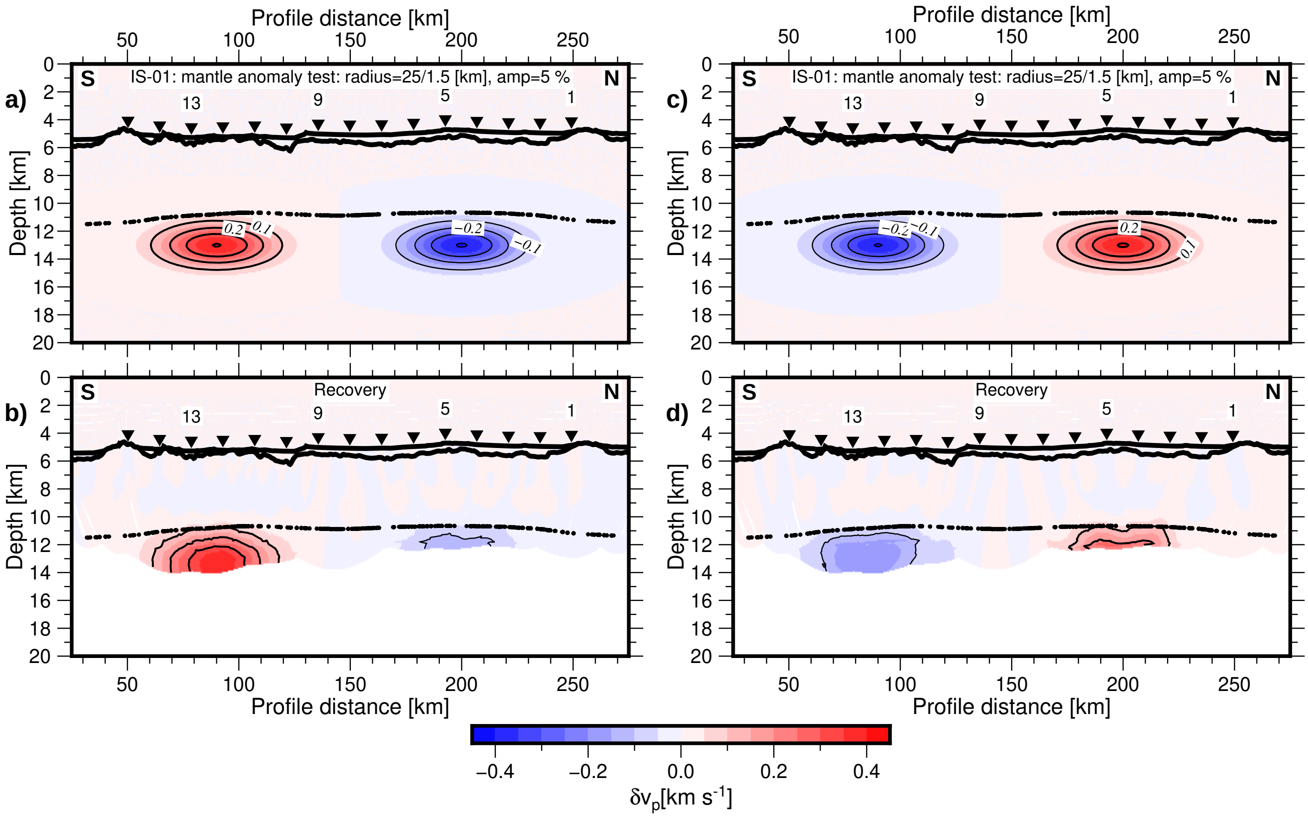

Figure S15. Mantle anomaly test for IS-01: the same testing procedure and figure elements as in Figure S14.

Table S2. Discretization, forward and inversion parameters used for the tomographic inversion with TOMO2D.

Parameter / Line	**LI-02**	**IS-01**
Discretizing		
profile length [km]	145	350
model depth [km]	20	20
horizontal velocity node spacing [km]	0.2	0.3
vertical velocity node spacing [km]	0.05 – 0.25, increasing with depth	
number of velocity nodes	102366	164547
horizontal reflector node spacing [km]	0.2	0.3
number of reflector nodes	726	1167
Forward modelling		
forward star	10x15	
max ray segment length [km]	1	
number of interpolation points per segment	8	
tolerance for conjugate gradient	4.00E-04	
tolerance for Brent minimization	5.00E-05	
Inversion		
horizontal correlation length for velocity [km]	1.25 – 5	1.5 – 5
vertical correlation length for velocity [km]	0.375 – 3	0.5 – 3
horizontal correlation length for reflector [km]	3	
velocity smoothing weight for Pg	30	30
velocity damping weight for Pg	30	30
velocity smoothing weight for Pg+PmP	50	70
velocity damping weight for Pg+PmP	50	50
reflector depth smoothing weight	50	70
reflector depth damping weight	50	50
depth kernel weighting factor	1	
velocity smoothing weight for Pg+PmP+Pn	100	100
velocity damping weight for Pg+PmP+Pn	500	300
max iteration Pg1	8	
max iteration Pg2	8	
max iteration Pg3	8	
max iteration PmP	8	
max iteration Pn	5	
target $\chi 2$	1.2	
tolerance for LSQR sparse matrix solver	3.00E-03	
number of initial models for MCA	100	
mean initial crustal thickness [km]	6	
velocity input standard deviation [km/s]	0.3 – 0.5	
Moho input standard deviation [km]	0.75	

Table S3. PmP reflector inversion parameters for strong and weak regularization. If two values are present, the first one refers to line LI-02 and the second to line IS-01.

Parameter/Line	**strong Reg.**	**weak Reg.**
Reflector correlation length [km]	3	1.25
Reflector smoothing weight	50, 70	15
Reflector damping weight	50	10
χ^2_{pmp}	0.9, 1.0	0.5, 0.5